Repurposing Trifluoperazine in Combination with Kinase Inhibitors for Glioblastoma Therapy: Insights from *In Vitro* and Larval Zebrafish *In Vivo* Models

A THESIS SUBMITTED TO
THE GRADUATE SCHOOL OF ENGINEERING AND SCIENCE
OF BILKENT UNIVERSITY
IN PARTIAL FULFILLMENT OF THE REQUIREMENTS FOR
THE DEGREE OF
MASTER OF SCIENCE
IN
MOLECULAR BIOLOGY AND GENETICS

By
Rana ACAR
August 2025

Repurposing Trifluoperazine in Combination with Kinase Inhibitors for Glioblastoma Therapy: Insights from *In Vitro* and Larval Zebrafish *In Vivo* Models

By Rana Acar

August 2025

We certify that we have read this thesis and that in our opinion it is fully adequate, in scope and in quality, as a thesis for the degree of Master of Science.

Özlen Konu Karakayalı (Advisor)

Onur Çizmecioğlu

Gülçin Çakan Akdoğan

Approved for the Graduate School of Engineering and Science

Orhan Arıkan

Director of the Graduate School of Engineering and Science

ABSTRACT

Repurposing Trifluoperazine in Combination with Kinase Inhibitors for Glioblastoma Therapy: Insights from *In Vitro* and Larval Zebrafish *In Vivo* Models

Rana ACAR

Msc. in Molecular Biology and Genetics

Supervisor: Assoc. Prof. Özlen KONU KARAKAYALI

August 2025

Gliomas are classified into lower-grade gliomas and glioblastomas, with the latter representing the most aggressive and treatment-resistant form, highlighting the urgent need for more effective therapeutic strategies. Recently, the antipsychotic drug trifluoperazine emerged as a potent anticancer drug for multiple cancers, including gliomas. Our previous research identified a potent therapeutic combination of trifluoperazine with sorafenib, a well-established multi-kinase inhibitor with proven efficacy in hepatocellular carcinoma, in Hep3B cell line model. In the present study, the transcriptomic response to trifluoperazine alone or in combination with sorafenib was evaluated in U87-MG glioblastoma cells and revealed that the combinatorial treatment induced a synergistic effect characterized by growth arrest, reduced invasiveness, and transcriptional signatures of metabolic stress and cell fate reprogramming. While trifluoperazine alone promoted a proliferative gene expression profile through the upregulation of essential metabolic and cell cycle-associated genes, its combination with sorafenib counteracted these effects by suppressing oncogenic signaling and amplifying tumor-suppressive pathways. These findings highlight the potential of trifluoperazine as a repurposed agent in kinase-targeted glioblastoma therapy and underscore the benefit of combinatorial strategies to overcome adaptive resistance mechanisms.

Although sorafenib treatment in glioblastoma cells provided mechanistic insights into its synergy with trifluoperazine, *in vivo* exposure to sorafenib caused severe morphological defects in zebrafish larvae over a 72-hour window from 2 to 5 dpf. Moreover, in a previous glial reporter imaging screen using Tg(*gfap*:GFP) line zebrafish larvae, sorafenib was observed to markedly reduce GFP fluorescence, whereas trifluoperazine alone did not produce any detectable adverse effects in either assay. This *in vivo* toxicity prompted the search for alternative targeted kinase inhibitors with more favourable safety profiles to combine with trifluoperazine. Other kinase inhibitors that had a growth inhibitory effect on U87-MG as well

as A172 cells were identified using MTT assays. A screen of 157 kinase inhibitors resulted in 12 kinase inhibitors with IC50 values less than 5 μM for both cell lines. Among the most promising with full cytotoxic effect were volasertib, INK128, CAY10626, tamatinib, Torin1, bisindolylmaleimide IX, AZD7762, NH125, and BMS345541. Trifluoperazine was also combined with selected kinase inhibitors, and volasertib and INK128 were identified to elicit significant synergism. On the other hand, several kinase inhibitors with significant inhibitory effects alone exhibited significantly reversed impact by the addition of trifluoperazine. The PLK1 inhibitor volasertib was top prioritized due to its highest synergy score in combination with trifluoperazine, and RNA-seq was performed on U87-MG cells treated with 2.5 μM volasertib to investigate its translational relevance. The resulting drug-induced gene signature was evaluated over the TCGA-GBM cohort, where high volasertib signature scores correlated with significantly improved overall survival, thereby reinforcing the rationale for its repurposing approach in combination with trifluoperazine for glioblastoma therapy.

Finally, the early larval toxicity profiles of prioritized single or combinatorial drug treatments were assessed *in vivo*, and neither induced developmental abnormalities or phenotypic signs of adverse effects. In this context, *LDexplore*, an R Shiny application was developed to enable multidimensional analysis of zebrafish larval locomotor behaviour under dark:light alternation, incorporating heatmaps and statistical analyses of velocity and acceleration in response to startle stimuli. The app was used to test whether the zebrafish larvae exposed to trifluoperazine alone or in combination with volasertib exhibited different locomotory behaviour and it was found that although trifluoperazine induced a heightened swimming pattern upon stimulus at higher concentrations, the combinatorial treatment was not significantly disruptive to light induced startle response.

These findings indicate that the combination of trifluoperazine and volasertib exhibits strong therapeutic potential, with *in vivo* applicability supported by larval zebrafish assays. Additionally, other kinase inhibitors demonstrating lower toxicity and significant synergistic effects on glioblastoma cell growth were identified, providing insights for further investigation.

Keywords: Glioblastoma, Cancer, Drug Screening, Drug Repurposing, Larval Zebrafish Model, Trifluoperazine, Volasertib.

ÖZET

Glioblastoma Tedavisi İçin Kinaz İnhibitörleriyle Kombine Trifluoperazinin Yeniden Amaçlandırılması: *In Vitro* ve Larval Zebra Balığı *In Vivo* Modellerinden Bulgular

Rana ACAR

Moleküler Biyoloji ve Genetik Yüksek Lisans Programı

Tez Danışmanı: Doç. Dr. Özlen KONU KARAKAYALI

Ağustos 2025

Gliomalar, düşük dereceli glioma ve glioblastoma olarak sınıflandırılır ve özellikle glioblastoma en agresif ve tedaviye en dirençli formu temsil ederek daha etkili terapötik stratejilere duyulan ihtiyacı ortaya koyar. Son zamanlarda, antipsikotik ilaç trifluoperazin, gliomlar da dahil olmak üzere birden fazla kanser türünde güçlü bir antikanser ajan olarak ön plana çıkmıştır. Önceki çalışmalarımız, trifluoperazinin; hepatoselüler karsinomda etkinliği kanıtlanmış çok hedefli bir kinaz inhibitörü olan sorafenib ile Hep3B hepatoma hücrelerinde güçlü bir terapötik kombinasyon oluşturduğunu göstermiştir.

Bu çalışmada, U87-MG glioblastoma hücrelerinde trifluoperazinin tek başına veya sorafenib ile kombine edildiğinde yarattığı transkriptomik etki değerlendirilmiş ve kombinasyon tedavisinin; büyüme duraklaması, invazivitenin azalması ve metabolik stres ile hücresel kader yeniden programlamasına ait transkripsiyonel imzalarla karakterize edilen sinerjistik bir etki oluşturduğu ortaya konmuştur. Trifluoperazin tek başına uygulandığında, temel metabolik ve hücre döngüsü ile ilişkili genlerin artan ekspresyonuyla proliferatif bir profili teşvik ederken, sorafenib ile kombinasyonu bu etkileri baskılayıp onkojenik sinyal yolaklarını susturmuş ve tümör baskılayıcı yolları güçlendirmiştir. Bu bulgular, trifluoperazinin kinaz hedefli glioblastoma terapisi için yeniden amaçkandırma potansiyelini vurgulamakta ve direnç mekanizmalarının üstesinden gelmek için kombinatoryal stratejilerin önemini ortaya koymaktadır.

Glioblastoma hücrelerinde sorafenib uygulaması trifluoperazin ile sinerjisi hakkında mekanistik bilgiler sağlamış olsa da, 2-5 günlük dönemde 72 saat süreyle zebrafish larvalarına yapılan *in vivo* maruziyetin şiddetli morfolojik bozukluklara yol açtığı gözlemlenmiştir. Ayrıca, Tg(*gfap*:GFP) hattı zebrafish larvaları kullanılarak gerçekleştirilen ön çalışmalardaki glial belirteç görüntüleme taramasında sorafenib, GFP floresansını belirgin şekilde azalttığı

halde; trifluoperazinin tek başına her iki deneyde de herhangi bir advers etki göstermediği gözlemlenmiştir. Bu *in vivo* toksisite, trifluoperazinin kombinasyonunda kullanılmak üzere daha düşük toksisiteye sahip alternatif kinaz inhibitörlerinin araştırılmasını öncüllemiştir. U87-MG ve A172 hücrelerinde büyümeyi baskılayıcı etki gösteren diğer kinaz inhibitörleri MTT analizleriyle belirlenmiştir. Toplam 157 kinaz inhibitörünün taranması sonucunda her iki hücre hattında da IC50 değeri 5 µM'nin altında olan 12 inhibitör tespit edilmiştir. Tam sitotoksik etki gösteren en umut verici bileşikler arasında volasertib, INK128, CAY10626, tamatinib, Torin1, bisindolylmaleimide IX, AZD7762, NH125 ve BMS345541 yer almıştır. Trifluoperazin, seçilen bu inhibitörlerle kombinasyon halinde test edilmiş ve volasertib ile INK128'in anlamlı sinerji sergilediği belirlenmiştir. Öte yandan, tek başına güçlü inhibitör etkisi olan bazı bileşiklerin, trifluoperazin eklenmesiyle ters yönde etki ettiği gösterilmiştir. PLK1 inhibitörü volasertib, trifluoperazin ile kombinasyonundaki en yüksek sinerji skoru nedeniyle öncelikli olarak belirlenmiştir. Translasiyonel önemini araştırmak üzere U87-MG hücrelerine 2,5 µM volasertib uygulanarak RNA-seq analizi yapılmıştır. Elde edilen ilaca özgü gen imzası TCGA-GBM kohortunda değerlendirilmiş, yüksek volasertib imza skorlarının anlamlı düzeyde artmış genel sağkalım ile ilişkili olduğu gösterilmiş, bu da gliblastoma tedavisinde trifluoperazin ile kombinasyonunun yeniden kullanım stratejisinin gerekçesini güçlendirmiştir.

Son olarak, öncüllenmiş tekil veya kombinasyon tedavi protokollerinin erken larval toksisite profilleri değerlendirilmiş, hiçbirinin gelişimsel anormalliklere veya fenotipik toksisite belirtilerine yol açmadığı gözlemlenmiştir. Bu kapsamda, zebra balığı larvalarının karanlık:ışık alternasyonuna verdikleri lokomotor davranışı çok boyutlu şekilde analiz edebilen; ısı haritaları ile uyarana bağlı hız ve ivme analizlerini birleştiren bir R Shiny uygulaması olan *LDexplore* geliştirilmiştir. Bu uygulama, trifluoperazin'in tek başına veya volasertib ile kombinasyon halinde uygulanmasının larvaların lokomotor davranışa etkisi test etmek için kullanılmış ve bu kombinasyon tedavisinin ışığa bağlı irkilme tepkisini anlamlı şekilde bozmadığı saptanmıştır.

Bu bulgular, trifluoperazin ve volasertib kombinasyonunun güçlü terapötik potansiyele sahip olduğunu ve zebra balığı larva deneyleriyle de desteklenen *in vivo* uygulanabilirlik sunduğunu göstermektedir. Ayrıca, daha düşük toksisiteye sahip ve glioblastoma hücre büyümesini anlamlı şekilde sinerjik olarak baskılayan diğer kinaz inhibitörleri de tanımlanmış olup, ileri araştırmalar için öncüllenmiştir.

Anahtar Kelimeler: Glioblastoma, Kanser, İlaç Taraması, İlaç Yeniden Amaçlama, Zebra Balığı Larva Modeli, Trifluoperazin, Volasertib.

To my family…

Acknowledgement

First and foremost, I would like to thank my advisor, Dr. Özlen Konu Karakayalı for her guidance throughout my undergraduate and master's studies. I am grateful for her insightful supervision that has profoundly shaped my way of thinking, as well as for her unwavering support and understanding. I have gained invaluable experiences and have grown both professionally and personally thanks to her. I am honoured to be her student.

I extend my profound thanks to my committee members, Dr. Onur Çizmecioğlu and Dr. Gülçin Çakan Akdoğan for dedicating their valuable time to evaluate my thesis.

I further thank Dr. Gülçin Çakan Akdoğan and Çakan Lab members for providing me valuable insights and generously sharing their expertise. I am additionally grateful to the Halt-RONIN consortium and the NIG-JOINT collaboration for the enriching experiences and interdisciplinary perspectives they offered me. While I greatly benefited from these interactions, this thesis work is independent of these collaborations.

I thank each of the current members of Konu Lab, namely Nil Gürgül, Algı Demirbaş, Başak Naz Ulusoy, Beyza Yüceer, Emel Ahmad, Fatma Betül Metin Yılmaz, and Ismat Nanjis, who have made me grateful for being part of a team. I specially and whole heartedly thank Zehra Fırat, for her guidance and thoughtful company that have been among my greatest supports in the lab. I thank former lab members, Güneş Tok and Rüya Tombuloğlu, for their lead and contribution in this project; as well as Abdul Moiz Aftab, Seda Aktürk, Burçin İrem Arıcı, Çağdaş Yanyatan, and Melike Tombaz, who had all been inspiring and supportive lab mates. I especially want to thank Merve Vural-Özdeniz, for her influential mentorship starting from my undergraduate, and her friendship ever since. I also specially thank Siber Güneş Çelik for being by my side throughout my master's. In addition, I thank my friends from Bilkent, Naciye Bozkurt and Melis Karaca for making these years memorable. I also thank Tülay Arayıcı, Seda Birkan, and Burcu Çeyrekli for their support in the department.

I thank Mert Demirdizen, with an appreciation I cannot describe enough with words, who has been my dearest fellow in every aspect.

My greatest thanks are to my family, Akiko Ushioda Acar, Ahmet Nejat Acar and Mine Acar, who have always been supportive of me with unconditional love.

This thesis work was funded by TÜSEB (Project No: 4223, Ethical Protocol No: 2023/12). I acknowledge the financial support I had received as its project scholar.

LDexplore presented in this study was conducted as part of the Halt-RONIN consortium funded by EU HORIZON (HORIZON-HLTH-2022-STAYHLTH-02/101095679).

I acknowledge that I am a recipient of the fellowship of 2210-A National MSc/MA Scholarship Program of Directorate of Science Fellowships and Grant Programmes (BİDEB) of Scientific and Technological Research Institution of Türkiye (TÜBİTAK). Lastly, I thank Bilkent MBG Department for its welcoming academic environment and financial support.

Table of Contents

List of Figures

List of Tables

Abbreviations

AB:	Wild-type zebrafish strain
AChE:	Acetylcholinesterase
AKT:	Protein kinase B
ANCOVA:	Analysis of covariance
AUC:	Area under the (dose–response) curve
BBB:	Blood–brain barrier
CaM:	Calmodulin
CaMK:	Calmodulin-dependent protein kinase
CDKN1A:	Cyclin-dependent kinase inhibitor 1A (p21)
CNS:	Central nervous system
DMSO:	Dimethyl sulfoxide
dpf:	Days post-fertilization
ECM:	Extracellular matrix
EGFR:	Epidermal growth factor receptor
ER:	Endoplasmic reticulum
ERK:	Extracellular signal-regulated kinase
FADS2:	Fatty acid desaturase 2
FDA:	Food and Drug Administration
GBM:	Glioblastoma multiforme
GFP:	Green fluorescent protein
GFAP:	Glial fibrillary acidic protein
GO:	Gene Ontology Resource
GSC:	Glioblastoma stem cell
GSEA:	Gene set enrichment analysis
GSVA:	Gene set variation analysis
HRAS:	Harvey rat sarcoma viral oncogene homolog
IC50:	Half-maximal inhibitory concentration

INK128: Sapanisertib (dual mTORC1/2 inhibitor)

KEGG: Kyoto Encyclopedia of Genes and Genomes

KRAS: Kirsten rat sarcoma viral oncogene homolog

LDH: Lactate dehydrogenase

MAPK: Mitogen-activated protein kinase

MGMT: O-6-methylguanine-DNA methyltransferase

mTOR: Mechanistic target of rapamycin

MTT: 3-(4,5-Dimethylthiazol-2-yl)-2,5-diphenyltetrazolium bromide assay

MWP: Multi-well plate

Myc: c-Myc oncogene

NF-κB: Nuclear factor kappa-light-chain-enhancer of activated B cells

PDGFR: Platelet-derived growth factor receptor

PI3K: Phosphoinositide 3-kinase

PKC: Protein kinase C

PLC: Phospholipase C

PLK1: Polo-like kinase 1

PTEN: Phosphatase and tensin homolog

ROS: Reactive oxygen species

RTK: Receptor tyrosine kinase

SFB: Sorafenib (multi-kinase inhibitor)

STAT3: Signal transducer and activator of transcription 3

SU6656: Src inhibitor

TFP: Trifluoperazine

TME: Tumour microenvironment

TMZ: Temozolomide

TNFα: Tumour necrosis factor alpha

TP53: Tumour protein p53

VEGFR: Vascular endothelial growth factor receptor

VOL: Volasertib (PLK1 inhibitor)

1. INTRODUCTION

1.1 Glioblastoma

Glioblastoma, also known as glioblastoma multiforme (GBM), is the most aggressive and lethal type of brain cancer, and is classified as WHO grade IV IDH-wildtype diffuse astrocytoma (Dewdney et al., 2023). It is also the most common form of malignant brain tumours, taking up around 60% of all cases (Wen & Kesari, 2008). Although there is slight variation across different populations, GBM incidence is reported to be around up to 5 cases per 100,000 people annually, with a higher frequency in individuals between 45 to 70 years old and a slight male predominance (Thakkar et al., 2014).

GBM tumours derive from cells of glial lineage, which support neuronal cells in the central nervous system (CNS) (Stupp et al., 2005). It can develop either as a primary GBM tumour, or as a secondary tumour that has evolved from a low-grade astrocytoma. GBMs that originate from differentiated glial cell types typically arise from astrocytes that have undergone malignant transformation (Kleihues et al., 2002). However, some research also suggest that another potential GBM origin may be stem-like oligodendrocyte precursor cells (OPCs) that differentiate into oligodendrocytes, another glial cell subtype responsible for maintaining the myelin sheath of neurons, yet tumours arising from mature oligodendrocytes are often classified differently as oligodendrogliomas due to their distinct molecular features (Persson et al., 2010). Similarly, tumours arising from the glial cell subtype of ependymal cells are classified differently as ependymomas, which develop also in the CNS, yet at a slow growth rate (Louis et al., 2016). Neither GBM nor the other types of glioma originate from microglia cells, yet these resident macrophages are known to be enhancing tumour progression and invasiveness through their significant involvement in the tumour microenvironment (TME)

(Hambardzumyan et al., 2016). The initial cause of GBM most commonly traces back to neural stem cells (NSCs) and neural progenitor cells (NPCs), which act as the main precursors to glial progenitor cells and possess the self-renewal and differentiation potential that, when coupled with oncogenic mutations, give rise to glioblastoma stem cells (GSCs) to initiate tumour formation (Alcantara Llaguno & Parada, 2016; Singh et al., 2003).

1.1.1 Progression and Prognosis of Glioblastoma

GBM carries one of the worst prognoses in oncology despite advancements in research and therapeutic options (Tan et al., 2020). Even with optimal therapy, median overall survival is only about 12-15 months, and less than 5% of patients survive beyond 5 years (Dewdney et al., 2023). Histologically, GBM tumours diffusely invade surrounding brain tissue and characteristically exhibit regions of necrosis and microvascular proliferation (Pouyan et al., 2025). This diffuse infiltration of GBM cells into normal brain and their propensity for microscopic level spread often make complete surgical resection impossible, rendering the tumour inevitably recurrent and highly lethal (Manoharan et al., 2024). Indeed, 75-90% of GBM patients experience relapse at or near the original site, typically within the first year (Waqar et al., 2022). Younger patients who undergo successful total resection and have good functional status tend to survive longer than older patients with incomplete resection or poor status (Weller et al., 2021).

Importantly, one of the strongest predictive and prognostic molecular biomarkers is the methylguanine DNA methyltransferase (MGMT) promoter methylation status (Pouyan et al., 2025). MGMT is a DNA-repair enzyme that counteracts alkylating chemotherapy. Although temozolomide, an oral alkylating drug that methylates DNA at a guanine position to induce lethal lesions and trigger cancer cell apoptosis, is the pioneering chemotherapeutic agent for

GBM, tumours with an unmethylated MGMT promoter express high MGMT levels and can readily repair temozolomide-induced DNA damage, leading to treatment resistance (Hegi et al., 2005). By contrast, tumours with MGMT promoter methylation, seen in around 40% of GBMs, have silenced MGMT expression and thus accumulate more DNA damage from temozolomide, exhibiting significantly better responsiveness to chemotherapy and improved survival outcomes. Other genetic factors can modulate prognosis as well (Pouyan et al., 2025). For instance, GBMs that arise from lower-grade, IDH-mutant astrocytomas referred as secondary GBMs, generally progress slower than IDH-wildtype primary GBMs, though by definition IDH-mutant tumours are classified separately as of 2021, often harbouring TERT promoter mutations, EGFR amplification, or changes in +7/−10 chromosome copies (Torp et al., 2022). Mechanistically, GBM progression is driven not only by autonomous tumour growth but also by interactions with the brain microenvironment. Recently, it was shown that glioblastoma cells can functionally integrate into neural circuits by forming synapse-like connections with neurons and become electrically coupled to neuronal activity (Krishna et al., 2023). This pathologic neuroplasticity was described to fuel tumour progression, highlighting greater functional connectivity between the tumour and brain, as well as to correlate with worse patient survival and cognitive impairment. The recurrence capacity and the tendency of GBM to actively remodel its microenvironment to its advantage by growth-promoting factors in the brain milieu that encompass cerebrospinal fluid dynamics, intracranial pressure regulation, cerebral perfusion, blood-brain barrier integrity, central respiratory control, and the supportive functions of glial cells collectively lead to its extremely poor prognosis.

1.1.2 Molecular Mechanisms Driving Glioblastoma

GBM is characterized by a complex array of genetic alterations and dysregulated signaling pathways leading to its aggressive nature and therapeutic resistance (Brennan et al., 2013). Large-scale profiling, such as that in The Cancer Genome Atlas (TCGA) and in recent single-cell studies, have revealed extreme intratumoural heterogeneity with multiple coexisting cell subpopulations having different molecular profiles and lineage states (Dewdney et al., 2023; Torp et al., 2022). Key driver pathways frequently altered in GBM include those controlling cell proliferation, survival, and invasion. Aberrant activation of receptor tyrosine kinase (RTK), especially epidermal growth factor receptor (EGFR), signaling is very common. EGFR is mutated or amplified in around 40-60% of primary GBMs, where a common variant is the deletion mutant EGFRvIII that leads to constitutive signaling and is found in a substantial subset of EGFR-amplified tumours. Other RTKs including PDGFRA, MET, FGFR, and VEGF receptor are also frequently overexpressed or mutated, driving multiple oncogenic downstream pathways (Brennan et al., 2013). The growth and angiogenesis process of GBM cells is devastatingly quick due to the disruption of its critical cell cycle regulatory pathways and its fast response to hypoxia for the supply of excess oxygen and nutrients (Furnari et al., 2007). Alterations in the PI3K/Akt/mTOR pathway are observed in a majority of GBMs, often via loss-of-function of the PTEN tumour suppressor or PIK3CA mutations, promoting unchecked cell growth and survival signals (Pouyan et al., 2025). Disruption of cell cycle regulators such as CDKN2A/B (p16/ARF) deletion that occurs in around 50-60% of GBMs and disables the Rb tumour suppressor pathway, and TP53 mutations or pathway inactivation, lead GBM cells to evade apoptosis and DNA damage checkpoints. The hypoxic, necrotic regions in GBM further drive aggressive behaviour by stabilizing HIF-1α and promoting invasiveness. Moreover, GBM cells can adopt stem-like or progenitor-like states as well as more differentiated astrocytic or mesenchymal states in response to therapy (Dewdney et al., 2023).

The phenotypic switch is often associated with NF-κB and inflammatory signaling, where cells with mesenchymal programs become more resistant to treatment with radiation or chemotherapy. This plasticity enables GBM to adapt and survive aggressive treatments as resistant populations, further increasing relapse risk. Equally important are the interactions of GBM with its tumour microenvironment. GBMs are often densely infiltrated by immunosuppressive microglia and macrophages as well as regulatory T-cells that help the tumour evade immune response (Liu et al., 2024). In addition, the presence of the blood–brain barrier (BBB) limits the delivery of many systemic therapies to the tumour site. The BBB in GBM is heterogeneously disrupted, often preventing drugs from reaching residual cancer cells. Besides, the genetic evolution of tumour cells continues during treatment. Recurrent tumours often accumulate new mutations such as those acquired by temozolomide induced DNA damage or by upregulation of mismatch repair pathways, which can further reduce drug efficacy (Varn et al., 2022). Finally, the infiltrative tumour border contains invading cells that are often in a slow-cycling state, rendering them less susceptible to radiation, which mainly kills dividing cells (Antonica et al., 2022). Overall, GBM's molecular pathogenesis involves a web of aberrant RTK/Ras/PI3K, TGF-β, Wnt signaling that drives proliferation and invasion with disrupted p53 and Rb tumour suppressor pathways, a dynamically shifting cellular composition, and a supportive microenvironment, all of which contribute to its malignancy and resistance to therapy.

1.1.3 PI3K/Akt/mTOR Pathway in Glioblastoma

The PI3K/Akt/mTOR pathway is one of the most frequently dysregulated cascades in GBM, where around 88% of GBMs harbour alterations activating this pathway (Langhans et al., 2017). Common lesions include EGFR amplification, activating PIK3CA mutations, or loss

of the PTEN tumour suppressor, all converging on hyperactivation of PI3K/Akt and its downstream effector mTOR (Colardo et al., 2021). Notably, unlike some oncogene addicted cancers, GBM cells are not uniformly dependent on PI3K for survival, hence its inhibition alone is often insufficient to induce apoptosis, indicating redundant survival routes. Recently, PI3K signaling has been shown to exert cell type-specific roles in GBMs. For instance, it primarily confers chemoresistance in stem-like GBM cells, whereas it mainly promotes motility and invasiveness in more differentiated tumour cells. Such findings suggest the pathway's effects can vary across the heterogeneous cell populations in a tumour, which should be considered in therapeutic targeting. The ubiquitous activation of PI3K/Akt/mTOR makes it an attractive therapeutic target, and numerous inhibitors have shown promise in preclinical models. These include pan-PI3K inhibitors, isoform-specific PI3K inhibitors, and dual PI3K/mTOR inhibitors, which can suppress GBM cell growth, especially in combination with other treatments (Zhao et al., 2017). However, none of the drugs targeting this pathway that have entered phase I/II clinical trials have demonstrated significant survival benefits, largely due to poor blood-brain barrier penetration and the emergence of resistance mechanisms (Colardo et al., 2021). Still, this axis remains a compelling target regarding the central role in cancer cell growth and survival, thus modern approaches focus on combination strategies and patient subgroup selection to improve treatment efficacy (Li et al., 2016). For instance, co-inhibition of parallel pathways as RTKs or MEK/ERK is being explored to overcome compensatory signaling. Widely used agents targeting this axis include the PI3K inhibitors GDC-0941, BKM-120, PX-866, the Akt inhibitor perifosine, and mTOR inhibitor rapamycin.

1.1.4 Cholesterol Metabolism in Glioblastoma

Altered lipid metabolism, particularly cholesterol homeostasis, is increasingly recognized as a driver of GBM malignancy. Cholesterol is an essential component of cell membranes and a precursor for steroid hormones and signaling molecules. Reprogramming of cholesterol metabolism has been considered as a metabolic hallmark in many cancers, including GBM (Guo et al., 2022). The brain maintains an isolated cholesterol pool since the blood-brain barrier largely prevents peripheral cholesterol entry. Therefore, GBM cells must fulfil their cholesterol needs locally. Studies have shown that they reduce their *de novo* cholesterol synthesis and become highly dependent on exogenous sources. For instance, GBM cells tend to downregulate cholesterol biosynthesis pathways while upregulating LDL receptors (LDLR) to scavenge cholesterol from the microenvironment (Han et al., 2020). They also accumulate cholesterol in esterified form within lipid droplets to support rapid growth. At the same time, GBMs often have diminished cholesterol efflux mechanisms and reduced production of oxysterols that activate liver X receptors (LXRs) to promote efflux. This metabolic rewiring indicates that GBM cells store cholesterol, and in turn sustains membrane synthesis, signaling, and energy storage, aiding tumour proliferation and survival (Pouyan et al., 2025). Elevated cholesterol levels in tumour cells have been correlated with greater malignancy and invasive capacity, suggesting cholesterol as a critical fuel for GBM progression. It has been demonstrated that activating LXRs by a brain-penetrant compound triggers massive apoptosis in GBM cells, but not in normal astrocytes, and causes tumour regression with prolonged survival in mouse models (Villa et al., 2016). The LXR-cholesterol axis can therefore be evaluated as metabolic vulnerability, where GBMs rely on high intracellular cholesterol and are fatally stressed when cholesterol efflux is enforced. Other approaches target different nodes of cholesterol homeostasis. For instance, inhibiting cholesterol uptake, blocking ACAT-mediated cholesterol esterification to prevent lipid droplet

formation, or stimulating cholesterol export are all being explored as potential GBM therapeutic strategies. Statins, which are HMG-CoA reductase inhibitors, have also been investigated to cut off *de novo* cholesterol synthesis. However, they have been shown to exhibit limited efficacy unless combined with other agents. In addition, restoration of CYP46A1 enzymatic activity has been shown to activate LXR-dependent cholesterol clearance, resulting in tumour suppression (Han et al., 2020). These suggest that drugs boosting cholesterol catabolism in the brain could be repurposed for GBM therapy. It has also been found that hypoxia in GBM further alters lipid metabolism, where HIF-1 was shown to induce fatty acid uptake and lipid storage. Moreover, high-throughput analyses have identified cholesterol metabolism gene signatures associated with poor prognosis in gliomas, reinforcing the clinical relevance of this pathway. Overall, targeting cholesterol metabolism through multiple angles holds significant promise as an adjunct to GBM therapy, given the tumour's heavy reliance on lipid metabolic reprogramming (Guo et al., 2022).

1.1.5 Calcium Signaling in Glioblastoma

Calcium (Ca^{2+}) is a universal second messenger that regulates numerous cellular processes, and GBM cells harness calcium signaling to support their malignant behaviour (Clapham, 1995; Venkataramani et al., 2022). Dysregulated calcium homeostasis is now recognized as a hallmark of cancer cell progression, including in GBM, where it contributes to uncontrolled proliferation, invasion, and therapy resistance (Pillai et al., 2025). GBM cells often exhibit aberrant expression or activity of various calcium channels, pumps, and binding proteins, leading to heightened intracellular levels that can drive tumour-promoting pathways linked to GBM cell motility and invasiveness. Calcium dependent enzymes and cytoskeletal proteins coordinate the cell contraction and expansion needed for migrating glioma cells to

navigate the brain. Activation of multiple calcium permeable channels, including IP3 receptors on the endoplasmic reticulum (ER), store-operated channels (Orai/STIM), transient receptor potential (TRP) channels, voltage-gated calcium channels (VGCCs), purinergic P2X receptors, and glutamate receptors, were shown to trigger pathways that promote cytoskeletal remodelling, cell migration, and matrix invasion in GBM (So et al., 2021). Similarly, calcium activated potassium (K^+) channels were shown to help maintain the ionic balance during calcium oscillations, facilitating repeated spikes that drive migration, and blocking these channels was shown to impair GBM cell movement (Catacuzzeno & Franciolini, 2018). Certain anti-epileptic drugs given to GBM patients for seizure control were shown to block voltage-gated calcium channels or glutamate receptors, potentially providing a secondary anti-tumour benefit. Moreover, it was found that cells in the tumour core, which are static or less migratory, had unsynchronized calcium spikes, whereas cells at the invasive periphery, which are highly mobile and invasive, displayed more intense and synchronized calcium bursts (Pillai et al., 2025). Such findings suggest that targeting calcium regulators might preferentially impact the invasive cell population in GBM. One promising target is the family of T-type voltage-gated calcium channels, which control calcium influx at relatively low membrane potentials, and are often overexpressed in high-grade gliomas (Visa et al., 2019). They promote cell cycle progression by providing calcium signals needed for G1/S transition and protect tumour cells from stress-induced death. A T-type calcium channel, Cav3.1, was shown to disrupt autophagy, induce TMZ resistance, and prevent GBM recurrence upon its inhibition or knock down. Other selective T-type inhibitors are also under development to exploit this vulnerability. Importantly, any calcium targeted strategy must be balanced, as calcium is vital in normal neurons and glia. However, the accumulating evidence that inhibiting calcium influx can slow cell proliferation and even trigger p53-dependent apoptosis in cancer cells makes a

compelling case that combining agents modulating calcium signaling along with standard therapy might yield improved outcomes in GBM pathophysiology (So et al., 2021).

1.1.6 Current Glioblastoma Therapies

The current standard-of-care for glioblastoma was established in the mid-2000s and has remained largely unchanged for over 15 years (Dewdney et al., 2023). It involves a multimodal approach, where the first step is maximal safe surgical resection of the tumour, which provides tissue for diagnosis and relieves pressure. Surgery is followed by radiation therapy to the tumour, concurrent with daily TMZ chemotherapy, and then adjuvant TMZ for monthly cycles (Pouyan et al., 2025). This regimen modestly improved survival compared to radiation alone, raising median survival for around 3 months. This standard chemoradiation is generally well-tolerated, though TMZ can cause systemic side effects as myelosuppression that may impact quality of life, and is pronouncedly benefited by patients with MGMT-methylated tumours. In recent years, an additional modality of Tumour Treating Fields (TTFields) has been incorporated for some patients, which are low intensity alternating electric fields delivered to the scalp with the aim of disrupting tumour cell mitosis. TTFields are FDA-approved due to their modest survival benefit and have been included in National Comprehensive Cancer Network (NCCN) guidelines as a recommended adjunct to standard chemoradiation in patients up to age 70.

Despite aggressive treatment, almost all GBMs recur, and there is no universally effective therapy. Options for recurrent GBM include repeat surgery, if feasible, and second-line chemotherapy. One commonly used drug for recurrence is bevacizumab, a monoclonal antibody against VEGF, which is administered to control edema and symptoms rather than as a curative therapy. Other cytotoxic agents like nitrosoureas including lomustine and carmustine

are also used, either alone or in combination. Procarbazine, vincristine, and regimens like TMZ re-challenge or carboplatin are also tried on recurrent GBM, but there is limited evidence on their efficacy. Numerous clinical trials have explored targeted drugs, immunotherapies, gene therapies, and combination approaches. Among promising leads of novel GBM therapies, targeted molecular therapies by smart combinations or patient-specific precision medicine stand out. Yet although small-molecule kinase inhibitors against EGFR, PDGFR, FGFR, and MET show potent tumour cell killing *in vitro*, they largely fail in clinical trials due to issues like poor BBB penetration and pathway redundancies. Newer strategies include antibody-drug conjugates (ADCs) that deliver toxins to tumour cells expressing a specific antigen (Dewdney et al., 2023). Immunotherapy approaches have been tested in many trials for GBM, but the immunosuppressive environment of GBM has proven to be a major obstacle. Trials of immune checkpoint inhibitors have been largely disappointing in GBM. Other immunotherapeutic approaches include personalized peptide or tumour-lysate vaccines and cell therapies (Liau et al., 2023). Similarly, viral therapies are being explored to stimulate immunity and directly lyse tumour cells (Desjardins et al., 2018). Another promising approach is CAR T-cell therapy, where patients' T lymphocytes are genetically modified to target GBM specific antigens. Early CAR T trials have targeted antigens like IL13Rα2, EGFRvIII, and HER2 which are enriched on glioma cell surface (Dewdney et al., 2023). Researchers are increasingly recognizing that multi-modality treatments may be needed for GBM. Nanotechnology-based delivery of drugs or RNA interference is another emerging area, aiming to improve drug penetration to the tumour. Metabolic therapies are also of interest since GBM cells exhibit altered metabolism characterized by the Warburg effect. Trials of ketogenic diets or drugs targeting metabolic enzymes such as inhibitors of glutamine metabolism are under investigation. Radiotherapy enhancements are also being tested to improve local control. Given the urgency, these emerging therapies and trial innovations are crucial.

1.2 Kinases as Targets in Cancers

Kinases are critical regulators of cell signaling, and their dysregulation is a hallmark of cancer. Alterations such as mutations or overexpression in both receptor tyrosine kinases (RTKs) and serine/threonine kinases can drive oncogenic transformation, promoting uncontrolled proliferation, survival, and metastasis (Li et al., 2024; Tomuleasa et al., 2024). In response to these insights, kinases have emerged as prime therapeutic targets in oncology. Over the past two decades, intensive research has led to the development and clinical validation of numerous kinase inhibitors, transforming cancer treatment, and today kinase inhibitors represent one of the largest classes of cancer drugs. A remarkable number of kinase-directed therapies have reached clinical trials, and over 70 small-molecule kinase inhibitors have been approved by the FDA for cancer, with many more in development (Attwood et al., 2021). These agents target a spectrum of kinases that are frequently dysregulated in tumours. For example, receptor tyrosine kinases like EGFR, HER2/ERBB2, and ALK are key oncogenic drivers in certain lung and breast cancers, and their inhibition with TKIs or antibodies yields significant clinical responses. Similarly, serine/threonine kinases critical to cell-cycle and survival pathways are targeted. For instance, BRAF mutations in melanoma are treated with RAF/MEK inhibitors, achieving markedly improved patient outcomes when used in combination (Cohen et al., 2021). Altogether, kinase-targeted therapies have become integral in managing cancers ranging from leukaemia to solid tumours, often achieving prolonged positive outcome.

Therapeutic strategies to inhibit kinases are diverse. Most widely used ones include the use of small-molecule ATP-competitive inhibitors, which are able to selectively bind the conserved kinase ATP pocket and block signaling (Li et al., 2024). Dozens of such inhibitors including largely EGFR, VEGFR, and CDK4/6 inhibitors are in clinical use, along with second and third generation compounds designed to overcome specific mutations that induce

resistance. In addition, monoclonal antibodies against RTKs, such as anti-HER2 trastuzumab, have shown success by preventing ligand-receptor interactions or downregulating the receptor of interest. Moreover, new modalities as kinase-targeted proteolysis via PROTACs and other degraders, and inhibitors of kinase-substrate interactions are in development for kinases that cannot be targeted by traditional ATP-site inhibitors. These innovative approaches apart from allosteric inhibitors aim to improve specificity and combat acquired resistance. Although kinase inhibitors are promising for both common and rare cancers, there is still a large number of members of the human kinome that has not been therapeutically targeted, with only around 30% of kinases being currently targeted by existing drugs, indicating the potential of new therapeutic discoveries (Attwood et al., 2021).

1.2.1 Volasertib in Cancer Research

Volasertib, also known as BI-6727, is a potent and selective small molecule inhibitor of Polo-like kinase 1 (PLK1), a serine/threonine kinase crucial for cell cycle progression. By binding the ATP site of PLK1, volasertib has been shown to induce mitotic arrest at the G2/M phase, and less often at S phase, leading to apoptotic cell death in cancer cells (Cholewa et al., 2017; de Braud et al., 2015). PLK1 is frequently overexpressed in a variety of solid tumours as well as acute leukaemias, and its high expression has been shown to correlate with tumour aggressiveness and poor patient prognosis, making it a compelling target for chemotherapy (Gjertsen & Schöffski, 2015). In addition, the mitotic failure induced by volasertib has been shown to be accompanied by induction of p53 and p21 signaling pathways and caspase-3 activation, indicating the induction of DNA damage response and apoptotic pathways. Volasertib was developed as a second generation PLK1 inhibitor to improve shortcomings of the first generation, BI-2536, providing higher clinical efficacy and longer half-life. It has been

shown to exhibit broad anti-tumour activity in numerous preclinical models across cancer types including colon, lung, melanoma, prostate, urothelial, and hematologic malignancies at nanomolar concentrations *in vitro*, while relatively sparing healthy cells. It has also been shown to have tumour regressive impact in melanoma mouse xenograft models (Cholewa et al., 2017). Given its promising effects as an anti-mitotic agent, it has also been explored in combination with other therapies for obtaining synergistic or additive effects (Su et al., 2022). For instance, it was combined with cisplatin in cervical cancer models, resulting in reduced cancer cell growth and superior tumour shrinkage *in vivo* compared to both single treatments (Xie et al., 2015). It has also been shown to exhibit synergistic cytotoxicity with vincristine in paediatric cancer models, enhancing apoptosis and reducing cell survival rates (Abbou et al., 2016). Other synergistic combinations include its combination with sorafenib in thyroid cancer models, with paclitaxel in ovarian cancer models, and with azacitidine in leukaemia models (Lin et al., 2019; Noack et al., 2018; Platzbecker et al., 2022). Combination approaches have thus been a major theme in using volasertib as an anti-cancer agent, aiming to integrate this PLK1 inhibitor into broader therapeutic strategies.

In the clinical context, volasertib has been tested for various solid tumours including melanoma, ureteral, breast, and non-small cell lung cancers in phase I trials either as monotherapy or in combination with standard chemotherapies of corresponding cancers, all demonstrating its manageable safety profile with mild to moderate adverse effects (de Braud et al., 2015; Lin et al., 2014; Schöffski et al., 2012). In these studies, volasertib was administered intravenously either as a single infusion of 300 mg on day 1 every three weeks or as 150 mg on days 1 and 8 every three weeks, achieving peak concentrations of approximately 2-3 μg/mL, i.e. 3-4.5 μM. However, it has not yet achieved sufficient impact on any of the solid tumours, and several overlapping hematologic toxicities observed upon combination therapies had limited its advancement in respective trials. Instead, attention has turned to hematologic

malignancies where volasertib has shown more promising results (Döhner et al., 2014; Platzbecker et al., 2022). Indeed, it has progressed into phase III trials for acute myeloid leukaemia (AML), although they were as well terminated due to unmet expectations (DeAngelo et al., 2015). Trends in recent research include a shift from using volasertib as monotherapy to combinatorial therapy, and efforts to identify genetic and molecular backgrounds as PLK1 levels and p-AKT status that predict which tumours are most susceptible (Gjertsen & Schöffski, 2015; Su et al., 2022). While volasertib has not yet reached clinical approval, its development has significantly advanced the understanding of PLK1 as a promising target against multiple cancers.

1.2.2 Small Molecule Kinase Inhibitors in Glioblastoma Research

Small-molecule kinase inhibitors have been intensively investigated as targeted therapies in GBM models and clinical trials. Table 1.1 summarizes 39 inhibitors, spanning agents that target cell-cycle regulators, RTKs, and angiogenesis kinases, as well as intracellular signaling nodes. Early-phase clinical trials of EGFR inhibitors yielded limited efficacy, largely due to blood-brain barrier penetration issues and intratumoural heterogeneity. Erlotinib and gefitinib demonstrated minimal impact on overall survival in phase II studies of newly diagnosed GBM, despite frequent EGFR amplification in patient tumours. Similarly, pan-PI3K and mTOR inhibitors achieved biochemical target engagement but failed to translate into meaningful clinical benefit, often due to their dose-limiting toxicities as setbacks. Multi-kinase angiogenesis inhibitors have shown more promise in modulating the highly vascularized GBM microenvironment. Regorafenib, a broad-spectrum VEGFR/PDGFR/RAF inhibitor, achieved a statistically significant survival benefit in recurrent GBM, becoming the first kinase inhibitor with regulatory approval for this indication. However, most multi-kinase agents such as

sorafenib did not improve outcomes in phase III trials when combined with standard chemoradiotherapy, highlighting challenges in balancing anti-angiogenic potency with toxicity. More recently, inhibitors of cell-cycle kinases and MAPK pathway modulators have also entered early clinical evaluation. The trial outcomes emphasize the need for enhanced blood-brain barrier delivery, precise biomarker selection, and combination strategies to overcome adaptive resistance.

Table 1.1. Small molecule kinase inhibitors under clinical trials for GBM chemotherapy.

Inhibitory Drug	Target Kinase(s)	Clinical Information
Abemaciclib	CDK4/6	Phase II (Rahman et al., 2023)
Adavosertib	WEE1	Phase I (Alexander et al., 2018; Song et al., 2019)
Afatinib	EGFR/ErbB family	Phase II (Huang et al., 2022)
Alisertib	Aurora kinase A	Phase I (Song et al., 2019)
Anlotinib	VEGFR1–3, FGFR1–4, PDGFRα/β, c-Kit	Phase II (Huang et al., 2022; Yang et al., 2023)
Axitinib	VEGFR1–3	Phase II (Salbini et al., 2025)
Buparlisib	Pan-PI3K	Phase II (Huang et al., 2022)
Cabozantinib	MET, VEGFR2, AXL	Phase II (Huang et al., 2022)
Cediranib	VEGFR, c-Kit	Phase III (Huang et al., 2022)
CC-115	DNA-PK and mTOR	Phase II (Rahman et al., 2023)
Copanlisib	PI3K-α/δ	Phase II (Huang et al., 2022)
Dabrafenib	BRAF V600E	Phase II (Cabezas-Camarero et al., 2024)
Dasatinib	Src family, ABL, c-Kit, PDGFR	Phase II *low efficacy* (Salbini et al., 2025)
Dovitinib	VEGFR, FGFR, PDGFR	Phase I/II (Huang et al., 2022)
Enzastaurin	PKC-β	Phase III *no survival benefit* (De Witt Hamer, 2010)
Erlotinib	EGFR	Phase II *no significant efficacy* (Raizer et al., 2004)
Everolimus	mTORC1	Phase II *no survival benefit* (Huang et al., 2022)
Gefitinib	EGFR	Phase II *disappointing results* (Huang et al., 2022)
Imatinib	PDGFRα/β, c-Kit, BCR-ABL	Phase III *no significant benefit* (Huang et al., 2022)
Lapatinib	EGFR/HER2	Phase I/II *no improved outcome* (Salbini et al., 2025)
Lenvatinib	VEGFR1–3, FGFR1–4, PDGFRα, RET, c-Kit	Phase II (Huang et al., 2022)
Motesanib	VEGFR1–3, PDGFR, c-Kit	Phase II (Huang et al., 2022)
Neratinib	EGFR/HER2	Phase II (Rahman et al., 2023)
Nilotinib	BCR-ABL, PDGFR, c-Kit	Phase II *low efficacy* (Salbini et al., 2025)
Nintedanib	VEGFR1–3, FGFR1–3, PDGFRα/β	Phase II (Huang et al., 2022)
Osimertinib	EGFR	Phase II (Cardona et al., 2021; Huang et al., 2022)
Palbociclib	CDK4/6	Phase II *no efficacy* (Taylor et al., 2018)
Pazopanib	VEGFR1–3, PDGFRα/β, c-Kit, FGFR	Phase II *no improvement* (Huang et al., 2022)
Perifosine	AKT pathway inhibitor	Phase I (Huang et al., 2022)
Pilaralisib	Pan-PI3K inhibitor	Phase I (Huang et al., 2022)
Regorafenib	VEGFR1, FGFR1, PDGFRα/β, KIT, RET, RAF1/BRAF, TIE2	Approved *Italy* (Salbini et al., 2025)
Sorafenib	VEGFR2/3, PDGFR, FGFR, c-Kit, FLT3, RAF	Phase II *no significant benefit* (Huang et al., 2022)
Sunitinib	VEGFR1–3, PDGFRα/β, c-Kit, RET	Phase II *high toxicity, no significant efficacy* (Huang et al., 2022)
Taselisib	Pan-PI3K inhibitor	Phase II (Huang et al., 2022)
Tandutinib	PDGFRβ, FLT3	Phase I (Huang et al., 2022)
Temsirolimus	mTORC1	Phase II *no overall survival benefit* (Huang et al., 2022)
Trametinib	MEK1/2	Phase II (Cabezas-Camarero et al., 2024)
Vandetanib	VEGFR2, EGFR, RET	Phase II (Huang et al., 2022)
Vatalanib	VEGFR1–3, PDGFR-β, c-Kit	Phase I/II (Huang et al., 2022)

Apart from clinically investigated small kinase inhibitor trials, multiple high-throughput screening approaches have been conducted, from genetic loss-of-function screens to small-molecule libraries and proteomic analyses, to uncover kinases that GBM cells rely on for growth or therapy resistance. Testing panels of small-molecule inhibitors can expose which kinase pathways are most actionable in glioma cells. These small-molecule screens complement genetic approaches by directly evaluating drug sensitivity, thereby identifying kinase inhibitors that could be rapidly repurposed or advanced to clinical testing in GBM. Kinome-wide RNAi by shRNA/siRNA screens have revealed several kinase dependencies in GBM such as the receptor tyrosine kinase AXL (P. Cheng et al., 2015; Varghese et al., 2016). Genome-wide and kinome-focused CRISPR knockout screens have also been applied to GBM models to unbiasedly discover essential genes such as MAP4K4 (Prolo et al., 2019). These approaches not only reveal potential target kinases but also emphasize that the spectrum of kinase targets in GBM may need to be tailored to tumour subtypes, with different kinases driving cell growth in different contexts (MacLeod et al., 2024). Additionally, proteomics-based profiling of GBM tumours has helped map active kinases and signaling networks for target discovery. Phosphoproteomic analyses have shown that GBM tumours maintain complex kinase signaling even when treated with kinase inhibitors, suggesting why single-agent inhibitions have had limited success in GBM, and supporting the use of proteomics to identify combination targets (Van Linde et al., 2022). Such kinase profiling approaches including mass spectrometry-based kinome assays and inhibitor affinity capture techniques are used to define the active kinome of GBMs, revealing which kinases are functionally driving tumour growth or resistance at a given time. Collectively, these clinical studies and preclinical screens highlight that glioblastoma harbours multiple kinase-driven dependencies that could be therapeutically exploited.

1.3 Phenothiazines in Cancer Research

Phenothiazines are a class of heterocyclic compounds long used as antipsychotic, antiemetic, and antihistamine drugs (Mehrabi et al., 2023; Shen, 1999). These compounds are cationic amphiphiles that integrate into cell membranes, altering lipid composition and calcium signaling. Their therapeutic mechanism of action is fundamentally linked with the targeting of dopaminergic receptors, in particular dopamine D2 receptor (D2R), yet they exhibit a broad range of biological impact in addition to it, including the inhibition of calmodulin (CaM) signaling, protein kinase C (PKC) activity, and P-glycoprotein transport (Jaszczyszyn et al., 2012). Epidemiological data from 1957-1980, showing that psychiatric patients on chlorpromazine had lower incidence of cancer than the general population, had led to the investigation of phenothiazines including chlorpromazine, promethazine, thioridazine, trifluoperazine, and fluphenazine as anticancer agents with known safety profiles (Kamgar-Dayhoff & Brelidze, 2021; Mehrabi et al., 2023). Repurposing established drugs can pave the way of new therapeutic approaches, leveraging their known pharmacokinetics and safety, and phenothiazines are especially attractive as they are inexpensive, cross the BBB, and have decades of clinical use (H. Cheng et al., 2015). More recently, several studies have explored how phenothiazines affect cancer cell survival, induce cell death, and interfere with oncogenic pathways across diverse cancer types. In addition, their ability to sensitize cancer cells to damage and overcome multidrug resistance by compromising plasma membrane integrity and repair in tumours has been proposed. Importantly, their antitumor potency is independent of their antipsychotic activity, indicating distinct anticancer mechanisms.

A central anticancer action of phenothiazines is the induction of apoptosis in malignant cells. Multiple studies have demonstrated that phenothiazines trigger apoptosis via diverse pathways including caspase activation, mitochondrial dysfunction, and disruption of survival

signals. For instance, thioridazine was shown to produce a sharp rise in cytosolic calcium level in leukaemia cells, followed by mitochondrial membrane permeabilization, caspase-3 activation, ER stress, and eventually apoptosis (Moraes et al., 2022). Notably, calcium chelators or ER stress inhibitors could rescue cells, confirming that thioridazine drives a calcium mediated apoptotic pathway. Likewise, thioridazine was shown to provoke apoptosis in lung cancer stem-like cells characterized by nuclear fragmentation, Annexin V positivity, caspase upregulation, and G0/G1 cell-cycle arrest accompanied by cell-cycle blockade (Shen et al., 2017). Chlorpromazine was also shown to inhibit tumour growth and induce apoptosis in colorectal cancer models, apparently by downregulating SIRT1 and thus restoring p53 pro-apoptotic function (Kamgar-Dayhoff & Brelidze, 2021). Chlorpromazine was found to induce G2/M cell cycle arrest and apoptosis via modulation of the PI3K/AKT/mTOR signaling axis and autophagy pathways (Jhou et al., 2021). Trifluoperazine (TFP), a calmodulin-inhibiting phenothiazine, can likewise trigger apoptosis in various malignancies (Yeh et al., 2012). In multiple myeloma, TFP was shown to inhibit cytoprotective autophagy by targeting the stress regulatory protein NUPR1, leading to apoptotic cell death (A. Li et al., 2020). It was also shown to induce apoptosis in osteosarcoma and glioma cells, together with G0/G1 cell-cycle arrest and reduced migratory and invasive capacity (Park et al., 2022; Zeng et al., 2024). These findings collectively highlight that apoptosis induction is a recurring mechanism by which phenothiazines exert their anticancer effects. By activating caspases, promoting DNA fragmentation, and disrupting survival pathways, phenothiazines effectively push cancer cells into programmed death while often sparing healthy cells.

Beyond apoptosis, phenothiazines influence a broad spectrum of cellular pathways that suppress tumour growth, metastasis, and therapy resistance. Firstly, the amphiphilic cationic nature of phenothiazines allows them to localize in lipid bilayers, altering membrane fluidity and impairing membrane integrity (Mehrabi et al., 2023). Cancer cells, which rely on efficient

plasma membrane repair due to high metabolic and mechanical stress, become vulnerable when this repair is compromised. By accumulating in membranes, they can also disturb calcium channel function, ultimately sensitizing cells to chemotherapy induced stress. For instance, thioridazine's induction of a cytosolic calcium spike not only triggers apoptosis but also reflects its interference in calcium signaling and ER homeostasis (Moraes et al., 2022). Moreover, thioridazine has been shown to affect the PI3K/Akt/mTOR cascade, contributing to anti-angiogenic effects and apoptosis in breast and ovarian cancer models (Shen et al., 2017). In glioblastoma cells, phenothiazines including TFP and chlorpromazine were identified as agents that can reverse cancer stemness signatures, activate autophagy and later apoptosis while altering MAPK signaling outputs (H. Cheng et al., 2015). Moreover, certain phenothiazines were shown to mislocalize oncogenic KRAS from the plasma membrane due to CaM inhibition, thereby blunting Ras/MAPK pathway signaling (Manoharan et al., 2022). For instance, a known calmodulin antagonist fluphenazine was shown to reduce Ras/MAPK signaling, lower c-Myc levels, and increase cancer cell apoptosis. By simultaneously hitting calcium-CaM signaling and the MAPK signaling, phenothiazines can attenuate proliferation signals and induce cell death. Phenothiazines were also shown to halt cancer cell proliferation by inhibiting DNA synthesis. Chlorpromazine was found to directly inhibit DNA synthesis by reducing thymidine incorporation into DNA in tumour cells, correlating with cell cycle arrest at G1 or G2/M phases in various cancers (Kamgar-Dayhoff & Brelidze, 2021). Another noteworthy aspect of phenothiazines is their activity against cancer stem cells and drug-resistant cell populations. Thioridazine has been shown to selectively target leukaemia stem cells, while sparing normal stem cells. It was also shown to inhibit sphere formation in lung cancer and glioblastoma models, indicating impairment of self-renewal capacity. Furthermore, phenothiazines can reverse chemoresistance mechanisms by modulating drug transporters, heat shock proteins, and repair enzymes. For instance, thioridazine and chlorpromazine were

reported to inhibit the P-glycoprotein drug efflux pump ABCB1, thereby resensitizing multidrug-resistant cancer cells to chemotherapy. Moreover, emerging studies suggest that phenothiazines might also affect the tumour microenvironment and metastatic capacity, likely by inhibiting cytoskeletal regulators and matrix metalloproteinases that might as well be associated with calmodulin inhibition and altered calcium signaling (Yeh et al., 2012). Notably, phenothiazines have demonstrated efficacy in brain cancers, leukaemias, lymphomas, , and numerous solid tumours including lung, breast, colorectal, ovarian, cervical, endometrial, prostate, and pancreatic cancers (H. Cheng et al., 2015; Cui et al., 2021; Kamgar-Dayhoff & Brelidze, 2021; Matarrese et al., 2024; Moraes et al., 2022; Shen et al., 2017). The accumulated evidence for cross-cancer efficacy suggests that phenothiazines exploit vulnerabilities common to many cancers and are worthy of further clinical investigation as multi-purpose anticancer agents.

1.3.1 Trifluoperazine in Glioblastoma Research

TFP is now recognized as a novel autophagy inhibitor in cancer cells (Zhang et al., 2017). It has been shown to upregulate autophagosome markers LC3-II, p62 and impair lysosomal acidification, indicating blockade of autophagic flux. It has also been shown to downregulate cathepsin L and homologous recombination proteins, indicating impaired DNA damage repair. Several preclinical studies have demonstrated TFP's potent therapeutic effects in GBM models. Firstly, it has been shown to activate GSK3β, thus lowering p-Akt and β-catenin levels, and prevent radiation-induced Nanog and Sox2 expression for malignant reprogramming in glioma initiating cells that have undergone standard radiation therapy (Bhat et al., 2020). This study has shown that TFP enhances the efficacy of radiotherapy in GBM by interrupting the induction of a stem-like, therapy-resistant phenotype and thus preventing the

emergence of treatment-resistant stem cell populations. In addition, TFP has been shown to synergize with the standard chemotherapy temozolomide and radiation (Stringer et al., 2023). It has been shown to effectively counteract resistance to chemoradiotherapy in GBM cells grown in human cerebrospinal fluid (CSF), which more closely mimics the brain tumour microenvironment, by inhibiting the key CSF-induced stress protein NUPR1. Importantly, the doses of TFP that eradicated tumour cells in these assays had minimal toxicity on normal human neurons and astrocytes, highlighting its therapeutic window in the brain. Other studies also validate the ability of TFP to sensitize GBM to radiation. In orthotopic GBM mouse xenograft models, the combination of TFP with radiation yielded significantly greater tumour control than radiation alone, leading to improved survival (Zhang et al., 2017).

Recent studies suggested that TFP can inhibit treatment induced malignant reprogramming of GBM cells, preventing stress induced adoption of stem-like, resistant phenotypes upon chemotherapy (Bhat et al., 2020). Although kinase inhibitors have had limited success in GBM, the ability of TFP to penetrate the BBB and target non-redundant survival mechanisms provides a strong rationale for combining TFP with emerging targeted agents to improve GBM outcomes (De Silva et al., 2025). In EGFR-driven tumours, tyrosine kinase inhibitors (TKIs) like gefitinib or erlotinib initially arrest tumour growth but resistance frequently arises, often through drug tolerant cancer stem cell populations and alternative signaling pathways as Wnt/β-catenin. So far, a combined treatment approach for TFP with small molecule kinase inhibitors has been utilized in a study that has shown the synergistic effect of TFP with the EGFR TKI gefitinib in non-small cell lung cancer (NSCLC) cells (Yeh et al., 2012). Strikingly, the study has also shown that combining TFP with gefitinib overcame TKI resistance *in vitro* and led to greater tumour growth inhibition in lung cancer mouse xenograft models. The synergy of TFP with sorafenib in Hep3B hepatoma cells was also described by our lab (Murat Yaman, PhD Thesis; Büşra Korkmaz, MSc Thesis). By targeting

quiescent stem-like cells, blocking autophagy, altering calcium/calmodulin signaling, and modulating transcriptional stress responses, TFP fills the gaps formed by kinase inhibitors that typically target a single oncogenic node.

1.4 Zebrafish Disease Models

Zebrafish (*Danio rerio*) have become a powerful vertebrate model in biomedical research, offering high genetic and physiological homology to humans and rapid, transparent development (Zhao et al., 2015). Over 70% of human disease-related genes have functional counterparts in zebrafish, and all major organ systems such as the brain, heart, and liver form within days post fertilization. These attributes, along with their high fecundity and optical transparency of embryos, enable direct *in vivo* observation of disease processes and high-throughput experimentation at low cost. Zebrafish are employed to model a broad spectrum of human diseases, from cancers to cardiovascular, metabolic, infectious, and neurological disorders. This model organism is also highly compatible for leveraging genetic tools such as CRISPR/Cas9 mutagenesis, transgenic expression and experimental manipulations to induce disease-relevant phenotypes that recapitulate aspects of human pathology (Choi et al., 2021; Sakai et al., 2018). Key advantages include the ability to visualize disease progression in vivo using fluorescent markers and to rapidly test interventions in large sample sizes.

1.4.1 Zebrafish Larvae in Toxicological Research

Zebrafish larvae have become a valuable model in toxicology and safety pharmacology due to their advantageous features of small size, rapid development and active absorption of small chemicals easily through water, which allow for high-throughput *in vivo* screens assessing the

efficacy and toxicity of numerous potential therapeutic compounds or environmental chemicals in parallel (Modarresi Chahardehi et al., 2020; Patton et al., 2021). They serve as a bridge between *in vitro* assays and experimentation on higher order mammalian models, thus can accelerate the process of drug discovery or the sequential approaches for identifying a biological mechanism while aligning with 3Rs principles. Importantly, since zebrafish are vertebrates with complex organ systems, they can reveal organ-specific toxicities that might be missed *in vitro*, yet they are much higher throughput and lower cost than traditional animal models. A range of toxicity assays have been standardized in zebrafish. The fish embryo acute toxicity (FET) test is an OECD-approved assay that uses zebrafish embryos, usually conducted before 96 hours post-fertilization, to determine acute lethality by LC50 values and teratogenic effects of chemicals. Endpoints assessed in the FET and similar assays include embryo survival, hatching success, and morphological abnormalities as edema, spinal curvature, or swim bladder inflation. Beyond acute lethality, zebrafish tests can cover neurotoxicity, cardiotoxicity, hepatotoxicity, reproductive toxicity, and endocrine disruption within early developmental stages. The ability to observe the intact developing organism over time gives a comprehensive view of toxic impacts. Larval zebrafish assays have been extensively used to evaluate the toxicity of cancer therapeutics, helping to balance efficacy with safety in preclinical development. Many chemotherapeutic drugs have well-known side effects as cardiotoxicity or neurotoxicity, and zebrafish have proven compatibility at modelling these. For instance, tyrosine kinase inhibitors and other targeted therapies have been tested on zebrafish larvae to screen for cardiac or vascular toxicities by observing changes in heart function or blood vessel development (Zakaria et al., 2018). *In vivo* zebrafish findings have correlated with mammalian cardiotoxic profiles in many cases. Zebrafish larvae have also been used to study chemotherapy induced neurotoxicity, such as peripheral neuropathy caused by platinum drugs or vinca alkaloids, by analysing behavioural endpoints and neuronal morphology after drug exposure.

Overall, zebrafish larvae have emerged as a versatile and predictive toxicology model. They allow researchers to observe comprehensive toxicity endpoints as lethality, teratogenicity and organ damage within days of exposure (Modarresi Chahardehi et al., 2020).

1.4.2 Larval Zebrafish Xenograft Models

Zebrafish larvae have been used extensively to study cancer initiation, progression, and therapy. Widely used methodologies include chemical carcinogenesis, transgenic oncogene expression, and xenograft transplantation to induce tumours (Zhao et al., 2015). These models allow for the investigation of tumour biology *in vivo* under relevant microenvironmental conditions. In fact, one of the most striking applications of zebrafish in biomedical science is the xenograft of human cells into larval fish, creating chimeric models of human disease (Hu et al., 2024). This approach involves transplanting cultured human cancer cells or patient-derived tumour cells into early-stage zebrafish larvae and observing their growth, invasion, and response to treatments within the living, transparent organism. The most common stage for xenograft injection is the zebrafish larva at 2 days post-fertilization (dpf), when larvae are developed enough to have circulation and tissue structure, but their adaptive immune system is still immature, and thus will not reject human cells (Gamble et al., 2021). Early pioneering work established the yolk sac as a convenient injection site, providing a nutrient-rich niche for implanted cells, yet multiple injection sites have been adapted depending on the experimental goal since then. They include the duct of Cuvier for injection into the bloodstream for modelling metastatic spread, the cavity between the yolk and body for localized tumour growth near abdominal organs, the caudal vein for intravenous injections, and the brain ventricle for modelling brain tumours and CNS metastases. These injections require precise micromanipulation, and slight variations in cell number delivered can affect engraftment

success. To improve consistency and throughput, recent advances have introduced automated microinjection systems that can inject hundreds of embryos with cancer cells in a reproducible manner, greatly speeding up the process. Once engrafted, human tumour cells proliferate and migrate within the zebrafish larval environment, typically over a period of 3-7 days before the larva outgrows the model due to immune development or size constraints. Researchers take advantage of the zebrafish's optical clarity to monitor these events in vivo (Hu et al., 2024). Tumour cells are usually labelled with a fluorescent dye as DiI/DiO or expressing fluorescent proteins as GFP/RFP so that the cell mass can be quantified and tracked under microscope. Powerful imaging modalities, enable visualization of cancer cell migration in real time within the intact larva. Invasion into neighbouring tissues and entry of cells into circulation to metastasize at distant sites can also be tracked dynamically. Another advantage is that the timeline of metastasis is highly accelerated in zebrafish larvae, where tumour cells can often be detected within 1-3 days after injection, providing a fast model (Gamble et al., 2021). The power of zebrafish xenografts for phenotypic drug screening has been demonstrated by several studies evaluating large panels of compounds for those that reduce tumour burden within the organism. Beyond general drug screens, zebrafish xenografts are being used in personalized medicine pipelines. Zebrafish patient-derived xenografts (PDX) involve transplanting dissociated tumour cells from a cancer patient biopsy directly into zebrafish larvae (Zhai et al., 2021). It has been reported that drug responses in larval PDX models correlated strongly with patients' clinical responses to chemotherapy. Additionally, to systematically address the growing number of zebrafish xenograft studies, a comprehensive, manually curated database ZenoFishDb v1.1 that enables researchers to search, visualize, and compare technical and biological attributes of zebrafish xenotransplantation studies, including molecular modifications, injection sites, and PDX details has been presented (Targen et al., 2020). Larval zebrafish xenograft models are highly efficient and cost-effective, and the throughput for drug

testing is far greater than in mouse xenografts with shorter experimental time course of 1-2 weeks. On the other hand, although the larval zebrafish immune system is convenient for engraftment, is not fully representative of the human tumour-immune interactions, and for studies beyond 7 days, the developing immunity limits the model. In addition, zebrafish are maintained at 28 °C, which is lower than human body temperature, necessitating the maintenance of xenograft models at suboptimal temperatures at which both the host larvae and the human cells can survive. Still, larval zebrafish xenografts have proven to be powerful translational model, accelerating the evaluation of cancer therapeutics and enabling experiments that would be impractical in mammals.

1.4.3 Behavioural Research on Zebrafish Larvae

Larval zebrafish has emerged as a powerful vertebrate model for neuroscience, toxicology, and pharmacology studies, offering practical advantages like small size, high synchronously developing sibling batch size, and low cost (Basnet et al., 2019). Despite differences in neuroanatomy, zebrafish share a high morphological and functional homology with mammals, with many of their brain structures as the retina, olfactory bulb, and cerebellum, and major neurotransmitter systems as GABA, glutamate, dopamine, and serotonin, being conserved. In addition, zebrafish larvae display complex behaviours as anxiety-like responses, memory, and defensive responses that can be quantified, and are sensitive to neuroactive or toxic substances (Modarresi Chahardehi et al., 2020). Another advantage of zebrafish larvae is that they can be tested at very early stages, even around 24 hours post-fertilization (hpf) for simple reflexes, as they already freely swim by 5 dpf, which is also when many of their neurochemical pathways are functional.

Automated systems, such as *Zantiks MWP*, *DanioVision*, and *ZebraBox*, exist to track zebrafish behaviour in terms of movement and tail reflexes across multi-well plates, enabling rapid and replicable screening of chemical libraries. Such tracking systems allow for measuring diverse neurological phenotypes mainly described by paradigms including locomotion, startle responses, thigmotaxis or edge exploration, optomotor reflexes, habituation, prey capture, and sleep-wake cycles. The rise of these paradigms has suggested that subtle behavioural changes, which might otherwise go unnoticed, can be detected and analysed with high statistical power (Basnet et al., 2019). The most widely used type of behavioural assays for neuropharmacology are light-dark assays. However, there are several different approaches and experimental protocols that do not fall under a well-defined standard. Light-dark locomotion tests, also referred as photomotor response assays, measure changes in spontaneous movement of larvae upon light-dark transitions, where their locomotor activity can be tracked over time or in response to stimuli. Neurotoxins often produce hyperactivity or paralysis phenotypes that serve as early indicators. Altered behavioural endpoints as reduced response to stimuli, seizure-like convulsions, or hypoactivity, can indicate neurodevelopmental toxicity even if the larvae do not exhibit morphological defects. Studies have shown that zebrafish larvae exhibit clear dose-dependent responses that make them reliable indicators of sublethal toxic stress. After swim bladder inflation at 4 to 5 dpf, zebrafish larvae display a distinct pattern of increased movement under dark and relative immobility under light. In practice, larvae are placed individually in wells and exposed to alternating light and dark phases, while an automated video tracker measures distance moved. Typically, a sudden transition from light to dark elicits an immediate spike in locomotor activity, whereas a transition from dark to light interrupts movement as a freezing or resting response. This behaviour is described to represent a startle response that is parallel to an anxiety-like reaction. Given the widespread use of light-dark locomotion assays, significant effort has been devoted to standardization and interpretation of factors that influence

the output. For instance, a study that utilizes alternating light-dark stimuli demonstrates that illumination parameters as differences in light intensity, exposure duration, and whether light-dark cycles are continuous or alternating are critical for larval behaviour (Tuz-Sasik et al., 2022). In addition, experimental variables such as time of day, larval age, maintenance conditions, and even well size has been shown to impact baseline activity in zebrafish larvae. Moreover, repeated alternating light-dark stimuli has been shown to result in a swimming pattern in which a pronounced increase in activity during each dark phase relative to the prior light phase is observed. For protocol optimization and normalization, a standardized light-dark assay on 4 dpf larvae was proposed with the incorporation of 30-minute light acclimation and optimized cycle lengths (Hillman et al., 2024). It has been suggested that proper acclimation significantly enhances the consistency of the dark phase hyperactivity. A high-throughput developmental neurotoxicity screen of environmental chemicals using larval light-dark locomotion assay has revealed that several compounds induced significant behavioural changes despite although they haven't caused any sign of developmental defect, suggesting their impact as early warning indicators of neurodevelopmental disruption (Jarema et al., 2022). In another alternating light-dark assay, lead (Pb) exposed larvae have been shown to exhibit hyperactive locomotion under light, with increased distance travelled and swim speed compared to controls (Kataba et al., 2020). This locomotor activity was accompanied by molecular signs of oxidative stress, with disrupted expression of genes encoding antioxidant proteins and apoptosis regulators in the larvae, that associated with hyperactive phenotype. Another study on 7 dpf larvae has termed a larval diving response as an alternative approach to characterize avoidant and anxiety-like behaviour (Fontana & Parker, 2022). Zebrafish larvae also exhibit a neural process termed as prepulse inhibition (PPI) of the startle response, where a weak pre-stimulus can suppress the magnitude of the subsequent startle reaction. It has been shown that PPI parameters are strikingly similar to those used in human PPI assays (Burgess & Granato, 2007;

Read & Hindges, 2024). Larval zebrafish PPI has gained interest as a model for neuropsychiatric disorders, most notably schizophrenia, as patients with schizophrenia consistently show PPI deficits. This alignment has reinforced the translational relevance of zebrafish sensorimotor assays. Subsequently, an enhanced protocol to perform reliable PPI testing on 6 dpf larvae using a commercially available behavioural analysis system equipped with a fast camera and acoustic stimulator, coupled with automated tracking software was developed (Banono & Esguerra, 2020). These studies have enabled high-throughput sensorimotor phenotyping and screening for compounds that affect sensorimotor gating, with implications for disorders like schizophrenia, ADHD, or sensory processing disorders. Beyond PPI, other sensorimotor tests like the optomotor response, which refers to swimming in response to moving visual patterns, and habituation assays, which measure how responses are reduced upon repeated stimuli, are being employed to further characterize neural plasticity in larvae (Basnet et al., 2019).

Zebrafish larvae are highly responsive to a variety of sensory stimuli apart from light, such as touch, vibration, and sound, which are exploited in alternative protocols for quantifying sensorimotor behaviours that reflect underlying neural functions. The current goal for behavioural assays remains to be the standardization of protocols and respective behavioural paradigms for enhancing their translational relevance (Petersen et al., 2022). To address the need for standardized and automated behavioural analysis, a machine learning-based web application Marigold for high-throughput, precise zebrafish larvae pose tracking, facilitating robust quantification of sensorimotor behaviours without requiring specialized hardware or programming has been developed (Teicher et al., 2025). However, variability in outputs among existing behavioural tracking systems highlights the necessity for additional standardized platforms to improve reproducibility and validations across studies. Ongoing development and

integration of diverse analytical tools are crucial to fully leverage zebrafish larvae as models in behavioural neuroscience and pharmacological research.

2. AIMS AND RATIONALE

Previous studies in our lab have shown the efficacy of phenothiazines, in particular trifluoperazine, in combination with sorafenib as potent anticancer agents for hepatocellular carcinoma using Hep3B cells (Murat Yaman, PhD Thesis; Büşra Korkmaz, MSc Thesis) and for glioblastoma using U87-MG and A172 cells as models (Güneş Tok, MSc Thesis). Transcriptomic analyses of these treatments revealed modulation of key pathways, including cholesterol homeostasis and de novo lipid synthesis, aligning well with findings in the literature (Mazière et al., 1988). However, no study to date has characterized the global transcriptional response of U87-MG glioblastoma cells to trifluoperazine and/or sorafenib. Furthermore, although sorafenib toxicity in zebrafish embryos has been documented, there is a lack of data on how alternative kinase inhibitors in combination with trifluoperazine affect glioblastoma cell growth, early larval morphology, or healthy zebrafish glial cell development monitored by a *gfap*:GFP reporter. Moreover, while a brain-orthotopic human glioblastoma xenograft model in larval zebrafish has been proposed in the literature, no investigation has yet evaluated the resulting locomotor behaviour of U87-GFP injected versus mock injected or uninjected larvae (npj ; dis). Finally, a multivariate analysis pipeline to assess drug-induced changes or changes upon engraftment in larval locomotor behaviour under dark:light alternation was aimed to be standardized. Accordingly, this thesis will address the following questions:

1. How do trifluoperazine and sorafenib, individually and in combination
    a. distinctively reprogram the U87-MG transcriptome, and which pathways are most affected?
    b. impact early larval zebrafish development?
2. Which additional kinase inhibitors display robust, reproducible growth inhibition in U87-MG and A172 glioblastoma cells?

3. Does combining trifluoperazine with any identified kinase inhibitor produce additive or synergistic antiproliferative effects, and which combinations emerge as promising therapeutic candidates?
4. Do the prioritized kinase inhibitors
    a. induce adverse developmental effects in healthy zebrafish larvae in vivo?
    b. modulate *gfap*:GFP glial reporter expression in early zebrafish larvae?
    c. alter locomotor behavior in zebrafish larvae under dark:light alternation?
5. Is the brain orthotopic larval zebrafish xenograft model promising for drug testing?

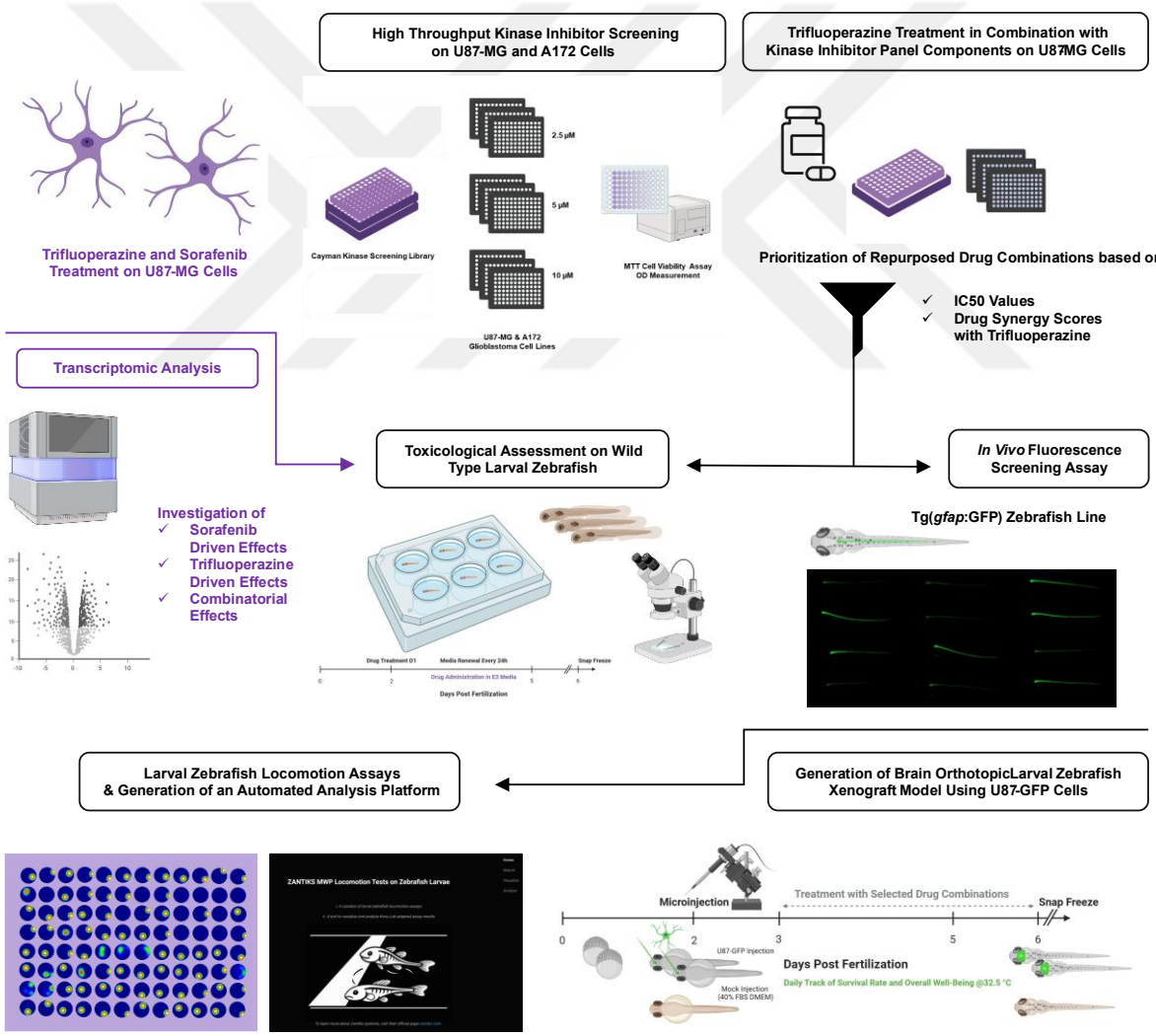

Figure 2.1. Representative workflow for the aim of the thesis.

3. MATERIALS AND METHODS

3.1 Materials

Table 3.1. Chemical reagents used for *in vitro* methods.

Product Name	Catalog No.	Company
Dimethyl sulfoxide Cell culture grade, 100 ml	A3672,0100	AppliChem, Germany
Dulbecco's Modified Eagle Medium (DMEM) High Glucose	BI01-052-1A	Sartorius, Germany
Dulbecco's Modified Eagle Medium (DMEM) High Glucose w/o phenol red	BI01-053-1A	Sartorius, Germany
Dulbecco's Phosphate Buffered Saline (D-PBS), 10X	BDL-002	Serena Europe, Australia
Fetal Bovine Serum (FBS)	04-001-1A	Biological Industries, USA
L-Glutamine Solution	B.X0550-100	Sartorius, Germany
MEM non Essential Amino Acids, 1X	X0557	Biowest, USA
Penicillin-Streptomycin Solution	BI03-031-1B	Sartorius, Germany
Trypsin-EDTA Solution, 10X	B.X0930-100	Sartorius, Germany
Sodium Pyruvate Solution, 100mM	BI03-042-1B	Sartorius, Germany
Sterile-filtered DNase/RNase/Protease free water	WAT333.1L	Bioshop, Canada

Table 3.2. Laboratory equipment used for *in vitro* and *in vivo* methods.

Equipment	**Company**
EVOS FL Auto Imaging System	Life Technologies, USA
MN120 Microbiological Safety Cabinet	Nüve, Türkiye
MZ10F Stereomicroscope	Leica, Germany
NB20 Water Bath	Nüve, Türkiye
NanoDrop ND-1000	Thermo Scientific, USA
Nuaire Autoflow IR Direct Heat CO2 Incubator	Nuaire, UK
PV830 Pneumatic PicoPump	World Precision Instruments, USA
Synergy HT Microplate Reader	BioTek, USA
SZX16 Stereomicroscope	Olympus, Japan
Universal 320 R Centrifuge	Hettich, Germany

3.2 Methods

3.2.1 In Vitro Methods

U87-MG and A172 glioblastoma cell lines were kindly provided by Dr. Tuğba Bağcı Önder and Dr. Ayça Arslan Ergül respectively.

3.2.1.1 Cell Culture

Cells were cultured in DMEM High Glucose (4.5g/l D-Glucose, 4mM L-Glutamine included; Sartorius, BI01-052-1A) supplemented with 10% (v/v) FBS (BI, 04-001-1A), 2% (v/v) Sodium Pyruvate Solution (Sartorius, BI03-042-1B), 1X MEM non Essential Amino Acids (Biowest, X0557), and 1% (v/v) Penicillin-Streptomycin Solution (Sartorius, BI03-042-1B). Cells were maintained under standard conditions at 37°C in a humidified incubator containing 5% CO_2. Growth media was refreshed every 2-3 days after washing with 1X PBS (Serena Europe, BDL-002) and cells were monitored regularly for contamination or aberrant growth. Cells were passaged at 80% confluency using 1X Trypsin-EDTA Solution (Sartorius, B.X0930-100) for detachment. Centrifugations were done at 210 x g for 5 minutes. For long-term storage, cells were cryopreserved in freezing media composed of 90% FBS and 10% DMSO (AppliChem, A3672,0100) and cryovials were stored in liquid nitrogen after gradual cooling. Cell thaws were done rapidly in a 37°C water bath followed by immediate transfer of cells into fresh growth medium for the removal of DMSO. All procedures were performed under UV-light pre-exposed laminar flow hood.

3.2.1.2 MTT Cell Viability Assay

Kinase Screening Library (Cayman Chemical, 10505) compounds (10 mM, 50 µL, n = 157) were aliquoted as 1 Master Plate (10 mM, 40 µL), 3 Mother Plates (10 mM, 10 µL) from the Master Plate, and 3 Daughter Plates (1 mM; 90% (v/v) DMSO, 20 µL) from each Mother Plate for both of the stock plates (Plate 1/2), and stored in film sealed 96-well microplates at -20°C.

For 3-dose single treatments of Kinase Screening Library compounds, U87-MG cells were seeded into 10 x 96-well cell culture plates at a density of 7 x 10^3 cells in 100 µL/well and let adhere for 24 hours under standard culture conditions. For the dilution of Plate 1 compounds (n = 80) in growth medium as 10 µM Experimental Plates, 297 µL/well growth medium was put in 3 x sterile 96-well plates and mixed with 3 µL compound from each well of a 1 mM Daughter Plate by vigorous pipetting using a multi-channel pipette. The well position of each compound was preserved, and triplicates were achieved in separate plates. For serial dilution to 5 µM Experimental Plates, 150 µL/well growth medium with 1% DMSO was put in 3 x sterile 96-well plates and mixed with 150 µL drug solution from each well of the 10 µM Experimental Plates. For serial dilution to 2.5 µM Experimental Plates, 150 µL/well growth medium with 1% DMSO was put in 3 x sterile 96-well plates and mixed with 150 µL drug solution from each well of the 5 µM Experimental Plates. Then, the growth media in each cell-seeded plate was renewed with drug solutions from the Experimental Plates in 100 µL/well. The well position of each compound was therefore preserved for each dose and replicate. The growth media in 8 wells of each cell-seeded plate was renewed with growth media with 1% DMSO as vehicle control. No cells were seeded in the remaining wells at the edges of the plate, and they were filled with 1X PBS to minimize variability in humidity across the plate and ensure even evaporation for accurate cell viability measurements. An additional plate was used for a control treatment of 700 µM TMZ (Cayman Chemical, 14163) in 5 replicates using 100

mM stock solution prepared by dissolving 10 mg TMZ in 515 µL DMSO. After treatment for 72 hours, 12 mM MTT (3-(4,5-dimethylthiazol-2-yl)-2,5- diphenyltetrazolium bromide; Invitrogen, 2277749) stock solution was prepared by dissolving 5 mg/mL MTT powder in sterile 1X PBS and filtered through 0.22 µm sterile filter. The prepared solution was then added into phenol red-free DMEM High Glucose (Sartorius, BI01-053-1A) in 100 µL/mL to avoid false absorbance measurements that can be caused by phenol-red. Drug solutions in growth media were carefully aspirated from the cell-seeded wells and replaced by 110 µL/well MTT solution/phenol red-free growth media mixture. The mixture was also put in 3 empty wells of each plate in 110 µL to be used as blank, i.e. triplicate background absorbance controls. After 4 hours of incubation at 37°C, 100 µL/well SDS-HCl solution, pre-prepared by adding 10 mL 0.01 M HCl solution per 1 g SDS (EMD Millipore, 822050) and dissolving the SDS salt by inversion and incubation in a 37°C water bath, was added to each well. Plates were incubated under cell culture conditions for 18 hours and absorbance was measured at 570 nm using *Synergy HT Microplate Reader* (BioTek). The same procedure was applied to evaluate Plate 2 (n = 77) compounds. The same set of experiments were performed on A172 cells, except that the seeding density in 96-well cell culture plates was 10^4 cells in 100 µL/well.

For the combinatorial treatments of 10 µM TFP (Sigma-Aldrich, T8516) and 2.5 µM Kinase Screening Library compounds, U87-MG cells were seeded into 3 x 96-well cell culture plates as above. 2 mM TFP stock solution was used to obtain a 20 µM TFP Experimental Plate in growth media. Then, a 5 µM Experimental Plate was prepared for Plate 1 components and the plates were vigorously mixed in 1:1 ratio, and DMSO content of all wells were maintained as 1%. The growth media of cell-seeded plates were renewed with the drug solutions within the combined Experimental Plate 24 hours post seeding. After treatment for 72 hours, MTT assay was performed as above.

For percent viability calculations, raw absorbance data of blank wells were subtracted from raw absorbance data of each well within the same plate for background normalization. Vehicle control wells containing 1% DMSO treated cells were used as 100% viability references. The background normalized values of each well were divided into the mean of control wells within the same plate, including that of each control well. All values were multiplied with 100 for percentage representation.

Percent cell viability values of cells exposed to 2.5, 5, and 10 μM Kinase Screening Library compounds in triplicates were used for nonlinear regression analysis over *GraphPad Prism 9* software. Drug concentrations were log-transformed using base 2 prior to curve fitting for calculation of half-maximal inhibitory concentrations (IC50 values). For each drug, the values of control wells, indicating 100% viability on average, from all plates in the assay were included to ensure standardized IC50 calculations. HillSlopes and IC50 values from log(inhibitor) vs normalized response curves with variable slope were recorded for the categorization of drug effects. Dose response matrices for combinatorial treatments were generated, and zero-interaction potency (ZIP) synergy scores were calculated using the `SynergyFinder` R package (version 3.10.3).

3.2.1.3 RNA Isolation from Cells

U87-MG cells were seeded into 6-well plates at a density of 2 x 10^5 cells in 2 mL/well. Cells were let adhere for 24 hours and treated for 72 hours. Phase-contrast images of cells were taken by *EVOS FL Auto* imaging system. Then, cells were washed twice with 1X PBS and let detach for 2 minutes in a 37°C incubator in 500 μL/well 1X Trypsin-EDTA solution covering the whole surface. Detached cells were collected in respective 1.5 mL Eppendorf tubes, washed with 1 mL 1X PBS, and immediately snap-freezed in liquid nitrogen as cell pellets. Samples

were stored at -80°C. RNA isolation steps were proceeded under chemical fume hood. 600 µL of QIAzol Lysis Reagent (Qiagen, 79306) was added per tube immediately after samples were taken from -80°C freezer. 120 µL chloroform (Sigma-Aldrich, 24216) was added on top, and the tubes were incubated at room temperature for 10 minutes after mixing the solutions by inverting 15 times. Then, the tubes were centrifuged at 16,200 x g for 20 minutes at 4°C for the separation of the supernatants into three phases, from which the upper aqueous RNA phase was transferred into new 1.5 mL Eppendorf tubes. Then, equal volume (380 µL) of 100% isopropanol (Sigma-Aldrich, 24137), filtered through a 0.45 µm sterile filter, was added on top of each tube. The solutions were mixed by inverting the tubes 5 times and then incubated at room temperature for 10 minutes. The tubes were centrifuged again at 16,200 x g for 10 minutes for the removal of the supernatant. Then, the pellets were washed with 1 mL/tube freshly prepared 75% ethanol (Sigma-Aldrich, B2221), filtered through a 0.2 µm sterile filter. After gently shaking, the tubes were centrifuged at 16,200 x g for 8 minutes at 4°C. After removal of the supernatant, the pellets were washed with 1 mL/tube 100% ethanol and centrifuged as the previous wash. The resulting RNA pellets were let air dry for 15 minutes at room temperature under fume hood. The pellets were dissolved in 20 µL in nuclease-free molecular biology water (Lonza, BE51200) and mixed well by pipetting. RNA concentrations and purity ratios were measured using NanoDrop ND-1000 (Thermo Scientific). Samples were stored at -80°C.

3.2.1.4 Cell Suspension Preparation for Microinjection

Stably transfected U87-GFP cells were thawed and plated in a T-25 flask and passaged into a 10 cm plate after 48 hours. Upon reaching 80% confluency, cells were let detach using 1X Trypsin-EDTA and collected in growth media for counting. 1 x 10^6 cells were collected in a 1.5 mL Eppendorf tube and centrifuged for obtaining a cell pellet. In a separate tube, 500 µL injection media, composed of an additional 40% (v/v) FBS in growth media to facilitate cells' adaptation to the host organism, was prepared. Cells were dissolved in 50 µL injection media. Remaining injection media was kept for mock injections. Both tubes were kept on ice before proceeding to larval zebrafish microinjection.

3.2.2 In Vivo Methods

3.2.2.1 Zebrafish Husbandry

Adult zebrafish were maintained under institutional and ethical guidelines for animal research. Fish were housed in 27±1°C circulating aquaculture system water in a 14:10 hour light-dark cycle for the maintenance of their circadian rhythm. Fish were fed twice with dry flake food and once with live artemia, and their health was routinely checked to monitor for signs of stress or disease.

Breeding setups were settled in mesh bottom tanks that promote natural spawning activity and prevent the predation of the parents on embryos. Zebrafish pairs or groups of 1:2 male to female ratio were acclimated within the tanks overnight with a separator between the male(s) and female(s). The separator was removed in the following morning to initiate spawning, and the embryos were collected at noon and transferred to 10 cm petri plates in E3 medium containing NaCl (Sigma-Aldrich, 13423), KCl (Sigma-Aldrich, 12636), CaCl2.2H2O (Carlo Erba,

327607), MgSO4.7H2O (Sigma-Aldrich, M2773), and methylene blue (Sigma-Aldrich, 115943) in distilled water. Unfertilized eggs or dead embryos were discarded and the plates were maintained at a 28°C incubator.

3.2.2.2 Larval Drug Treatment

AB wild-type or Tg(*gfap*:GFP) transgenic line zebrafish embryos were grown to 2 dpf in 10 cm petri plates with regular E3 media renewal. At 2 dpf, a substantial portion of the larvae still remains within their chorion structure. Therefore, physical dechorionation was applied under stereomicroscope using a sterile needle and forceps without harming any body part of the larvae. Tg(*gfap*:GFP) line larvae were categorized by their GFP reporter expression by signal checking under *Olympus SZX16* stereomicroscope equipped with fluorescence illumination. Dechorionated larvae were placed in 48-well plates as 6 larvae per well in 500 µL fresh E3 media. Drug solutions and dilutions were prepared in fresh E3 media with a final DMSO content of 0.25%. All treatments were applied in groups of triplicate wells. Drugs were administered to larvae by discarding the E3 media from wells and adding 500 µL of the drug solutions which were renewed daily until 5 dpf.

At 5 dpf, larvae were anesthetized using 0.04% tricaine (MS-222) solution and laterally positioned on 3% methylcellulose gel for imaging. Brightfield images were taken under *Leica MZ10F* stereomicroscope. Anesthetized larvae were collected in 1.5 mL Eppendorf tubes as 15 larvae per tube for each group and washed twice with 1X PBS. Larval pellets were obtained by completely discarding the PBS and the tubes were snap-freezed in liquid nitrogen. Samples were stored at -80°C. All larval handling was done in the scope of Ethical Protocol No: 2023/12.

3.2.2.3 RNA Isolation from Whole Larvae

Larval pellets were taken out of -80°C, carried in liquid nitrogen, and immediately mixed in 100 µL/tube NucleoZOL (Macherey-Nagel, 740404.200). For homogenization, an additional 400 µL/tube NucleoZOL was added and vigorously mixed by passing the suspension through sterile disposable 1 mL syringes up and down. For the precipitation of contaminants, 200 µL/tube nuclease-free water was added and mixed vigorously by inverting the tubes 15 times. After incubating for 15 minutes at room temperature, the tubes were centrifuged at 12,000 x g for 15 minutes at room temperature. Then, 500 µL of the upper, RNA phase supernatant was transferred into new Eppendorf tubes and 500 µL filtered, ice cold 100% isopropanol was added and mixed by flicking the tubes. Samples were stored at -20°C overnight to increase the yield of total RNA precipitation. Next day, samples were incubated at 4°C for 10 minutes and then centrifuged at 12,000 x g at 4°C for 10 minutes. After discarding the supernatant, RNA pellets were washed twice with freshly prepared, filtered, ice cold 75% ethanol in 500 µL/tube and centrifuged at 8,000 x g at 4°C for 3 minutes. RNA pellets were let air-dry for 15 minutes under fume hood and then dissolved in 20 µL nuclease-free water.

3.2.2.4 Brain Orthotopic Xenograft Model

AB wild-type larvae were grown to 2 dpf and dechorionated as previously described. 1.5% agarose gel was prepared by mixing 900 mg agarose in 60 mL E3 media. The mixture was heated in a microwave for 2 minutes and agarose was let dissolve completely by swirling. The solution was distributed into two 10 cm petri plates, separate for U87-GFP injections and mock injections, and cooled down to solidify with aligned toothpicks on top used as mold. Borosilicate glass microcapillary tubes (VitroTubes, CV8010-B-100) were heat-pulled from the middle by a micropipette puller. All equipment including petri plates, needles, tweezers,

agarose plates, microcapillary tubes, pipettes, and freshly prepared E3 media was sterilized and exposed to UV-light for 20 minutes. 8 µL U87-GFP cell suspension was loaded into a pulled microcapillary tube using microloader pipette tips (Eppendorf, 5242956003) without forming any air bubble stuck within the tube. The microcapillary tube was placed in the micromanipulator associated with the *PV830 Pneumatic PicoPump* (World Precision Instruments) microinjector. Larvae were anesthetized with tricaine and aligned in ventral position on the agarose plate, and microinjections were performed by inserting the microcapillary in between the two eyes for the ejections to target the midbrain. The ejections were performed in a controlled pressure ranging from 10 to 15, and a timed ejection period of 4. Ejected cell count was adjusted to 300 by counting them on agarose plate prior to microinjection into larvae. Injected larvae were GFP signal checked under fluorescent stereomicroscope, recovered in fresh E3 media, and grown in a 32°C incubator until 5 dpf. Mock injections were performed by injecting only the injection media under the same conditions. At 5 dpf, larvae were anesthetized, imaged, and snap-freezed. Bright field and fluorescent images were merged using *ImageJ* software.

3.2.2.5 Fluorescence Screening Assay

Zebrafish larvae from the Tg(*gfap*:GFP) transgenic line were used with the objective of evaluating possible changes in *gfap* expression upon drug treatment. Larvae were imaged at 2 dpf pre-treatment and at 5 dpf post-treatment to assess the emitted GFP signal over time. Larvae were anesthetized using tricaine and laterally positioned in 3% methylcellulose gel on microscope slides. Fluorescent imaging was done using *EVOS FL Auto Imaging System*, which features a lid to reduce background noise. Image acquisition parameters, including exposure time and light intensity, were optimized using the brightest fluorescent signal among the larvae

at 2 dpf to prevent photobleaching and data loss. These parameters were then kept constant for all larvae during both 2 dpf and 5 dpf imaging. Larvae were tracked individually across timepoints to account for inherent differences in baseline *gfap*:GFP expression. Signal intensities were quantified using *ImageJ*, and signal modulations were calculated as the log2 ratio of integrated fluorescence intensity between 5 dpf and 2 dpf.

3.2.2.6 Larval Locomotion Assay

Locomotion assays were performed by utilizing the *Zantiks MWP* system (Zantiks Ltd.). Larvae were placed in 96-well plates, individually in each well, in 100 µL/well fresh E3 media 2 hours before the *Zantiks* run for their acclimation to the well plate. The internal standard temperature of the system was set to 28°C and the external room temperature was stabilized to 27°C. After placing the well plate in the testing chamber, the protocol, consisting of a 10 minute acclimation period in the dark without data collection, followed by a 10 minute *DARK I* period, a 10 minute *BRIGHT* period, a 10 minute *DARK II* period, a 30 second *Startle Light* stimulus, and a *FINAL DARK* period, was run. Data collection for total distance travelled in each well was done periodically with a 30 seconds time bin throughout all light-dark periods. The overhead illumination was used for the *BRIGHT* period and the light stimulation plate was used for the *Startle Light* stimulus.

3.2.3 In Silico Methods

3.2.3.1 Bulk RNA-seq Data Analysis of U87-MG Cell Samples

Raw fastq sequencing data was preprocessed over *Galaxy*. Read quality control was done using `FastQC`. The paired end library was mapped to the human genome assembly GRCh38 using the `HISAT2` algorithm. Raw count data from the resulting BAM files was generated using GRCh38.84 gene annotation file via `featureCounts`.

All analyses were performed in R (version 4.3.3). Ensembl gene IDs were converted to gene symbols using `biomaRt` (version 2.58.1). Among two replicates of *DMSO*, *TFP*, *SFB*, and *TFP_SFB* groups, one replicate of *DMSO* was discarded from the analysis due to poor sequence quality, content, and duplication levels. DESeq2 (version 1.42.1) was used to integrate the design matrix to the count data and create an object for differential gene expression analysis. Genes having low or zero count among all samples, with sum of counts ≤ 1, were filtered out. The baseline group, *DMSO*, was set as the reference level. Variance stabilizing transformation (VST) was applied to the normalized dataset to prepare for downstream analyses by increasing the consistency of variance across all expression levels. Principal component analysis (PCA) was conducted on the transformed dataset and principal components with high proportion of variance (> 0.1) were plotted with the percent variance displayed by each component. Plots were generated using `ggplot2` (version 3.5.1). Log2 fold change results of each dual contrast were saved. Volcano plots for each contrast were generated for the visualization of gene expression modulations, with log2 fold change values on the x axis, and their statistical significance, with negative log10-transformed p values on the y axis. A gene list reported to have a statistically significant impact on cell growth in sensitive cell lines, referred to as essential genes, was curated from *shinyDepMap*. Genes on the volcano plot were color coded by significance categories of *Significant*, if their adjusted p value was lower than 0.05 and their

log2 fold change value was higher than an absolute value of 1, *Significant Essential*, if they were both essential and present in the essential gene list, and *NS*, if non-significant. Non-overlapping gene name labeling was done using `ggrepel` (version 0.9.6). For gene set enrichment analysis (GSEA), the gene statistics (stat), from the *DESeq2* differential expression analysis output, were assigned to a ranked list in decreasing order and the gene symbols that were used as identifiers were converted to Entrez IDs using `org.Hs.eg.db` (version 3.18.0), ensuring unique mapping. *Hallmark Gene Sets (H)*, *Canonical Pathways (CP)* within *Curated Gene Sets (C2)*, and *Gene Ontology (GO)* gene sets from the Molecular Signatures Database (*MSigDB 3.0*) were retrieved using the `msigdbr` package (version 7.5.1). Enrichment was performed using `clusterProfiler` (version 4.10.1) on the ranked gene list with the selected MSigDB collections as reference, and with 0.05 as the p value threshold for enriched pathways. Pairwise term similarities of enrichment results were calculated using `enrichplot` (version 1.22.0) and the terms were shown in clustered tree plots. GSEA plots that mimic plots generated by Broad Institute's *GSEA* software were generated using the `gseaplot2` function for top enriched terms. Clustered heatmaps were generated using `ComplexHeatmap` (version 2.18.0) to visualize the differential expression of genes that fall into specific gene sets of interest, including MSigDB Hallmark; *Hypoxia* (M5891), *Epithelial to Mesenchymal Transition* (M5930), *Cholesterol Homeostasis* (M5892), *mTORC1 Signaling* (M5924), and KEGG pathway; *Cell Cycle* (hsa04110), *Apoptosis* (hsa04210), *Glioma* (hsa05214) gene sets. Custom color mapping of log2 fold change values and p values was done using `circlize` (version 0.4.16). To visualize significant gene expression modulations in a specific KEGG pathway, i.e. *Calcium Signaling Pathway* (hsa04020), log2 fold change values of genes with p values lower than 0.05 were extracted. Filtered log2 fold change values were mapped to the human pathway ID using `pathview` (version 1.42.0), highlighting upregulated, near zero, and downregulated genes in distinct colours.

3.2.3.2 Survival Analysis on TCGA-GBM Cohort

Survival analysis was performed on primary-tumour samples from the TCGA-GBM cohort ($n = 372$). Raw counts were TMM-normalized and transformed to logCPM using `edgeR` (version 4.0.16). Gene identifiers were mapped from *Ensembl* to *HGNC* symbols via `org.Hs.eg.db` (version 3.18.0). Gene signatures for volasertib vs DMSO (VOL) and sorafenib vs DMSO (SFB) were defined as those with absolute log2 fold-change > 1.5 and adjusted $p < 0.05$ in respective differential expression analyses. Sample-level z-scores were computed by `GSVA` (version 1.50.5) for each *Up* and *Down* gene set as described by Hänzelmann et al., and composite signature scores (*Up* - *Down*) were dichotomized at the cohort median into *High* vs *Low* groups as described by Vinik et al. (Hänzelmann et al., 2013; Vinik et al., 2025). Clinical endpoints (vital status, days to death or last follow-up) were extracted from the metadata, and Kaplan-Meier curves stratified by signature group were fit with *survfit* from `survival` (version 3.5-8) and compared by log-rank test (95% CI by default). Curves, risk tables, and p-values were plotted using *ggsurvplot* from `survminer` (version 0.5.0).

3.2.3.4 Development of R Shiny Application

An interactive web application was developed using the R `Shiny` (version 1.8.1.1) framework to streamline the visualization and statistical analysis of zebrafish larval locomotion data recorded on *Zantiks MWP* system. The application's user interface was styled with `bslib` (version 0.8.0) and organized into a navigation bar containing four main tabs. The *Home* tab displayed described the automated analysis platfrom. The *Search* tab was generated for users to explore a table of published locomotion studies or review detailed *Zantiks* protocol

schematics. The *Visualize* tab permitted upload of raw *Zantiks* CSV exports and group annotation files with well plate design that should be generated by the user, which were ingested reactively and displayed in a scrollable table, and passed to custom plotting routines that produced SVG outputs through `svglite` (version 2.1.3), `ComplexHeatmap` (version 2.18.0), and `ggplot2` (version 3.5.1). Finally, the *Analyze* tab offered two analytical modules: a period boxplot generated by utilizing `reshape2` (1.4.4) and `ggpubr` (version 0.6.0) and a period-specific distance-time graph with overlaid linear slopes and ANCOVA statistics produced by leveraging `broom` (version 1.0.7), `emmeans` (version 1.10.5), and `patchwork` (version 1.3.0) for model fitting and pairwise trend tests. All server logic resided in a single server function, which monitored file inputs, re-read data reactively, and re-rendered tables and images on demand whenever users uploaded new files or selected different analysis options. The UI layout, constructed with *fluidPage*, *navbarPage*, and conditional panels, guided users seamlessly through data upload, exploration, visualization, and statistical interpretation, providing a robust, reproducible environment for high-throughput behavioural phenotyping of 4-6 dpf zebrafish larvae in a 96-well plate setup.

4. RESULTS

4.1 Combinatorial Effects of Trifluoperazine and Sorafenib on U87-MG Transcriptome

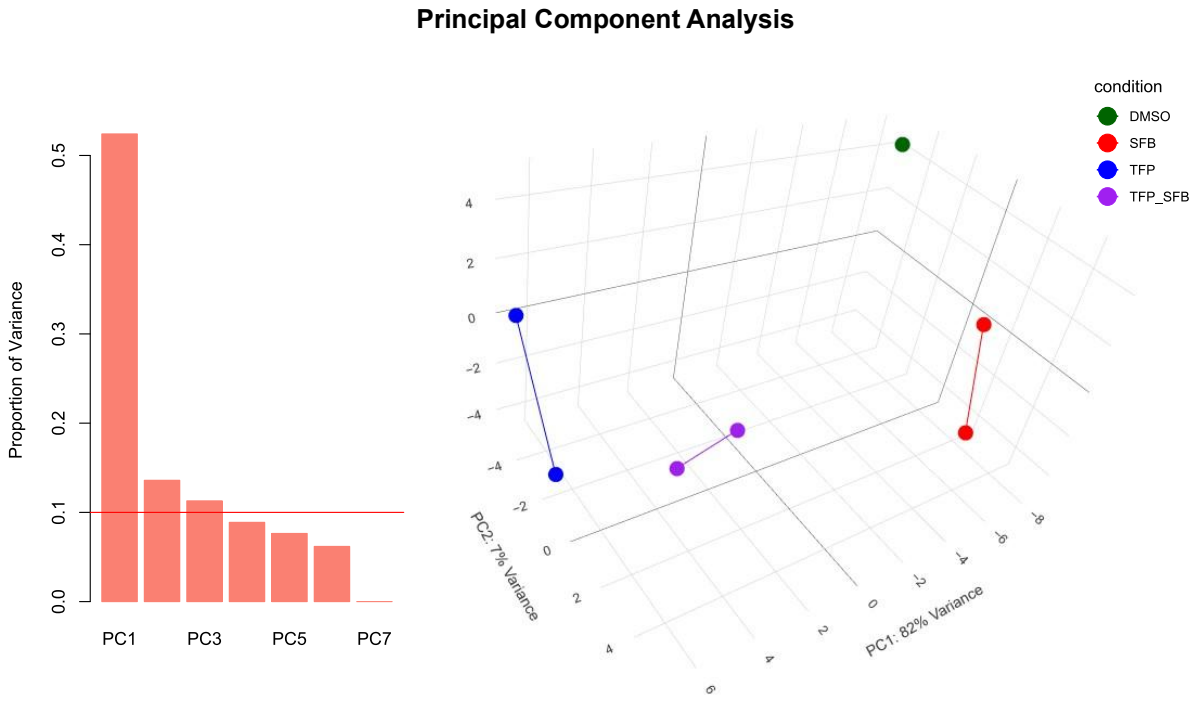

Figure 4.1. PCA plots of RNA-seq results from $TFP_{10\ \mu M}$ and/or $SFB_{2.5\ \mu M}$ treated U87-MG cell samples.

PCA plots shown in Figure 4.1 reveal that the first three principal components account for a proportion of variance greater than 10%. The experimental groups, including 1 replicate of *DMSO* and 2 replicates of *TFP*, *SFB*, and *TFP_SFB* each, were seen to be clearly dispersed and replicates within each group were seen to be closely clustered, indicating differences in the transcriptional profiles of the experimental conditions with low intra-group variance. *TFP* and *TFP_SFB* seem to be the closest groups, indicating overlapping but distinct profiles driven by the combinatorial treatment. In addition, the positioning of *TFP_SFB* in between *TFP* and *SFB* indicates its intermediate profile influenced by both treatments.

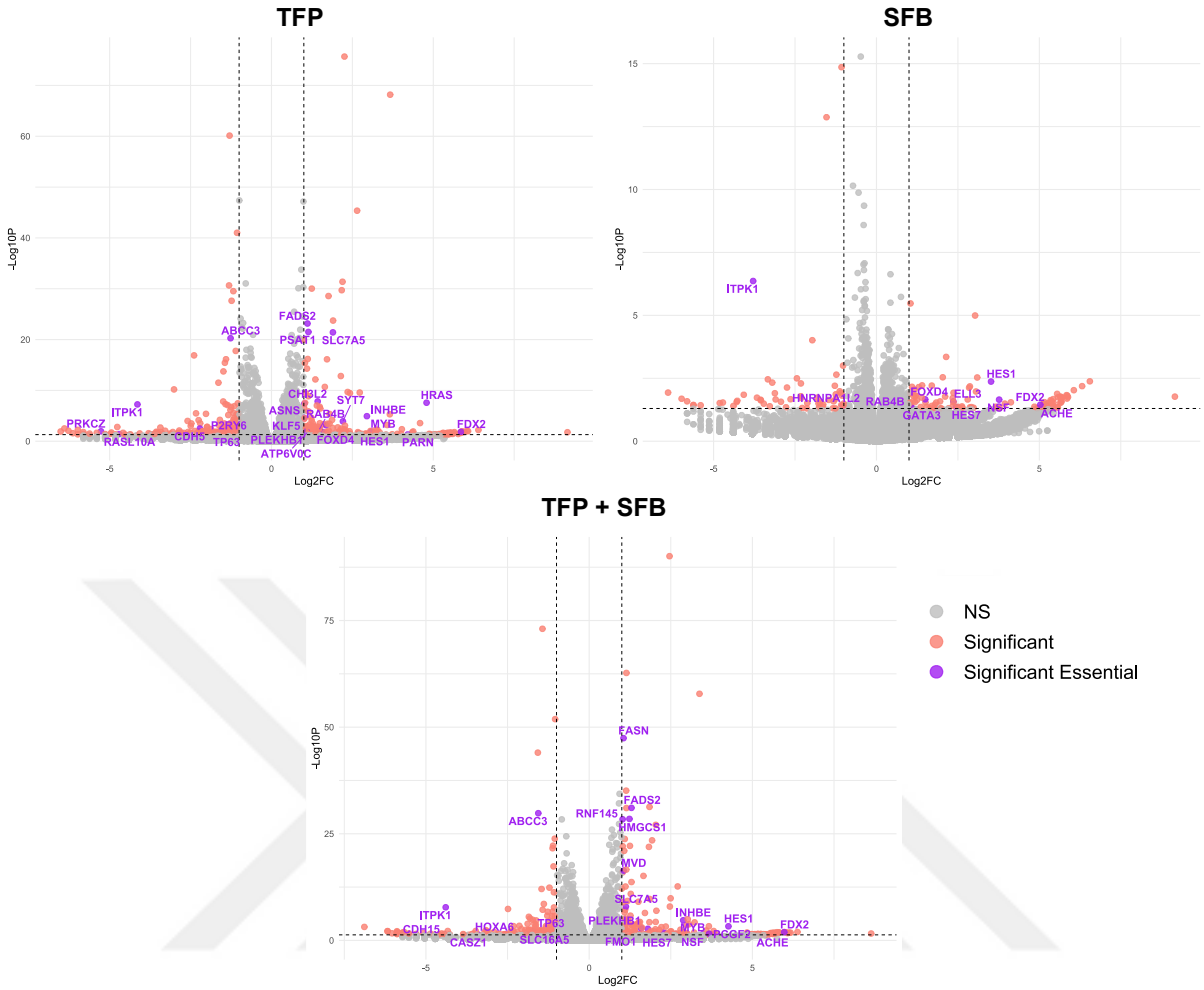

Figure 4.2. Volcano plots showing significantly modulated (p-value < 0.05, absolute log2 fold-change > 1) *DepMap* essential genes from differential gene expression analysis results by DESeq2 ($TFP_{10\ \mu M}$ and/or $SFB_{2.5\ \mu M}$ vs DMSO).

The differential gene expression analysis of TFP (10 µM) treatment versus DMSO control revealed significant modulations of several *DepMap* essential genes, including *FADS2*, *PSAT1*, *SLC7A5*, *HRAS* upregulation and *ABCC3, PRKCZ* downregulation shown in Figure 4.2. Although it is seen from the second volcano plot that SFB (2.5 µM) treatment versus DMSO control had modulated a fewer portion of statistically significant genes, *ACHE, NSF, ELL3* were upregulated and *HNRNPA1L2* was downregulated. The upregulation of *FDX2, HES1* and

downregulation of *ITPK1* were similar upon both single treatments. TFP (10 µM) + SFB (2.5 µM) combinatorial treatment versus DMSO control revealed uniquely upregulated essential genes including *FASN*, *HMGCS1*, *RNF145*, and *MVD*.

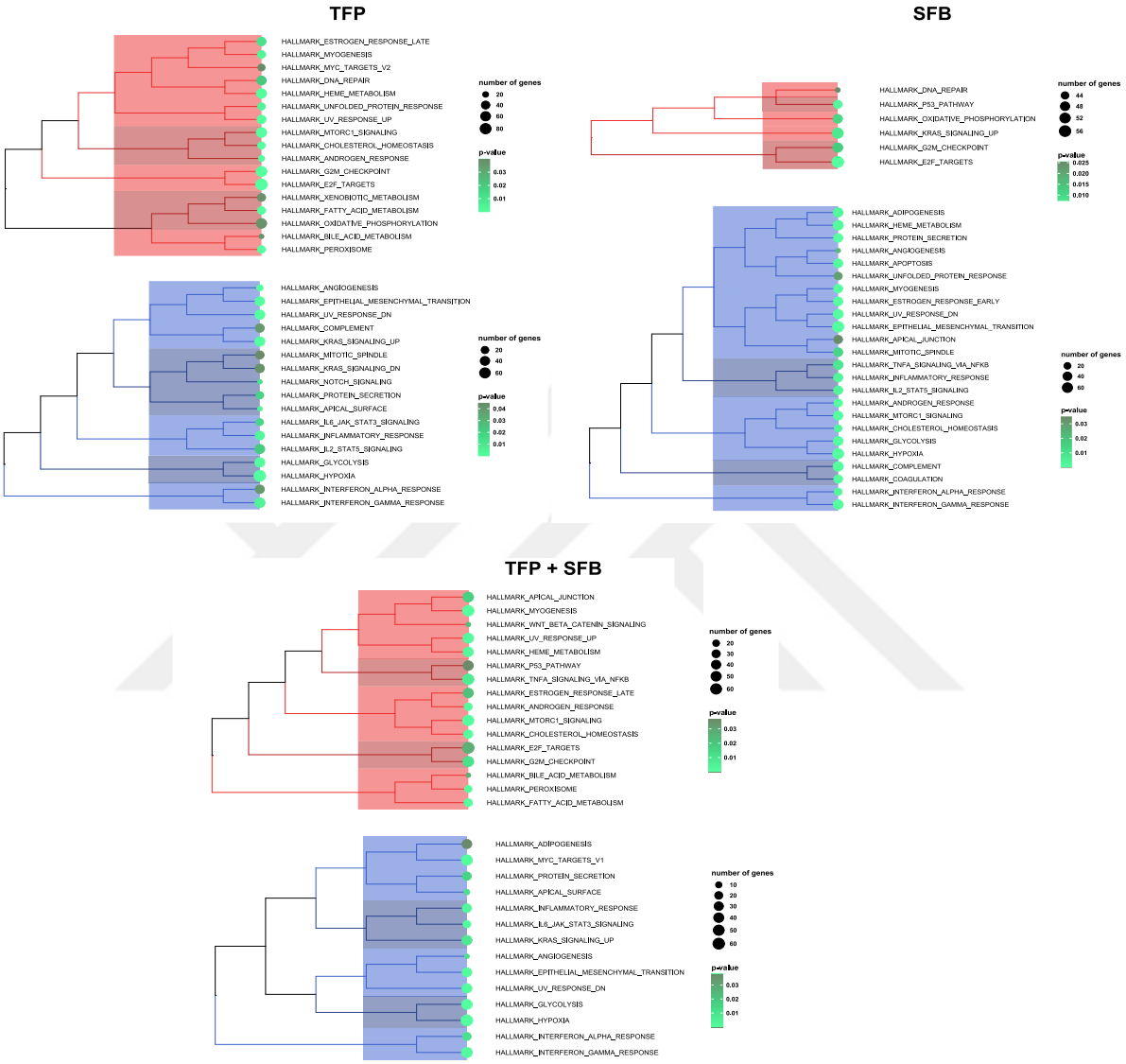

Figure 4.3. MSigDB Hallmark gene set enrichment analysis results using DESeq2 statistics covering log2 fold-change values and standard error ($TFP_{10\ \mu M}$ and/or $SFB_{2.5\ \mu M}$ vs DMSO; p-value < 0.05 enrichment cutoff).

Pre-ranked gene set enrichment analysis results for TFP alone versus DMSO showed that top modulated gene sets were involved in terms that together associate with significant metabolic reprogramming, by activated mTORC1 signaling, fatty acid metabolism, cholesterol homeostasis, heme metabolism, and repressed glycolysis; and with cell cycle regulation and stress adaptation, by activated E2F targets and G2M checkpoint, and repressed hypoxia and KRAS signaling (Figure 4.3). Activated myogenesis, and repressed EMT, hypoxia, and inflammation by TNFa signaling via NF-kB, interferon alpha and gamma response, IL2-STAT5 signaling, and IL6-JAK-STAT3 signaling were also seen to show up among top enriched gene sets, reflecting a shift of the gene expression profile to an adaptive state of cancer cell plasticity in this non-muscle cell context. Apart from several similar enriched terms for top modulated genes by SFB alone versus DMSO, activation of genes involved in DNA repair and the p53 pathway and repression of genes involved in mTORC1 signaling, cholesterol homeostasis, coagulation, and apoptosis were observed. TFP + SFB combinatorial treatment vs DMSO, was seen to modulate genes associated with terms that overlap with those from TFP and/or SFB single treatments. To further investigate biological processes by which TFP acts synergistically with SFB on U87-MG cell viability, GSEA results using Gene Ontology (C5) gene sets were visualized by a ridge plot (Figure 4.4). 20 out of 282 terms supportive of the enriched Hallmark gene sets were shown by the gene statistic distribution density plot.

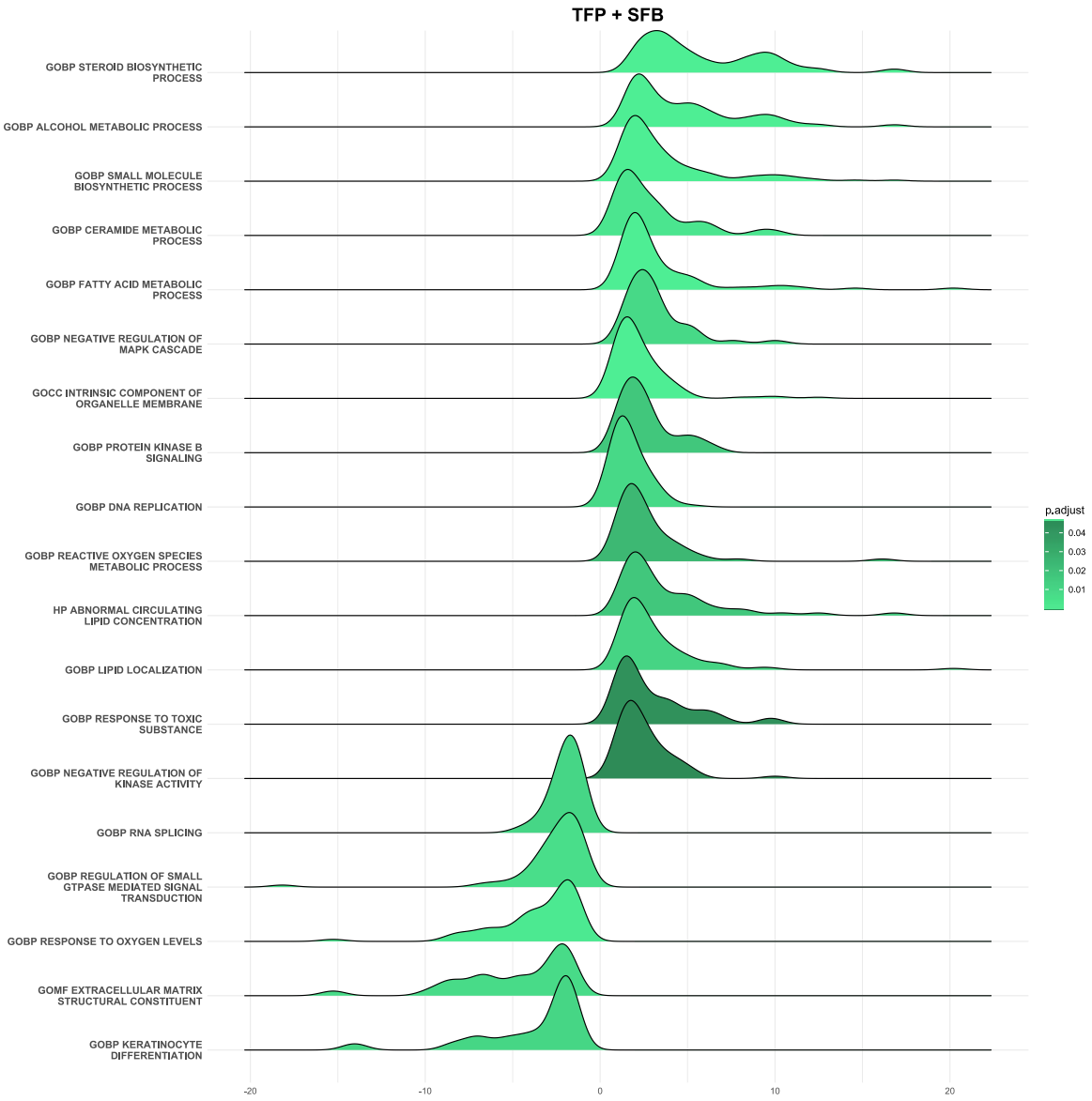

Figure 4.4. Ridge plot for top gene set enrichment analysis results of TFP + SFB vs DMSO using Gene Ontology (C5) terms (20/282 enriched terms; p-value < 0.05 enrichment cutoff).

4.1.1 Sorafenib-Driven Effects

The effects of the TFP + SFB combinatorial treatment on U87-MG cells that was driven majorly by SFB was aimed to be investigated. Given the intermediate transcriptional profile induced by the combinatorial treatment (Figure 4.1), the focus was on evaluating the influence of TFP on pathways that were dominantly modulated by SFB alone, and whether it further modulates or counterbalances the effects in key cellular processes.

Figure 4.5 shows that SFB alone modulated gene sets that are mostly enriched with hypoxia, epithelial to mesenchymal transition, UV response, protein secretion, and coagulation pathway components; all with negative normalized enrichment scores (NES) lower than -2.25. Top enriched Hallmark gene sets for the contrast of TFP + SFB vs TFP alone were visualized for evaluating SFB driven and/or synergistically modulated pathways upon combinatorial treatment. The top significantly upregulated pathway was observed to be cholesterol homeostasis with 2.58 NES. TGF-beta signaling pathway was also positively enriched, with 2.13 NES. E2F target, MYC target, and G2M checkpoint gene sets were negatively enriched with NES' lower than -2.09.

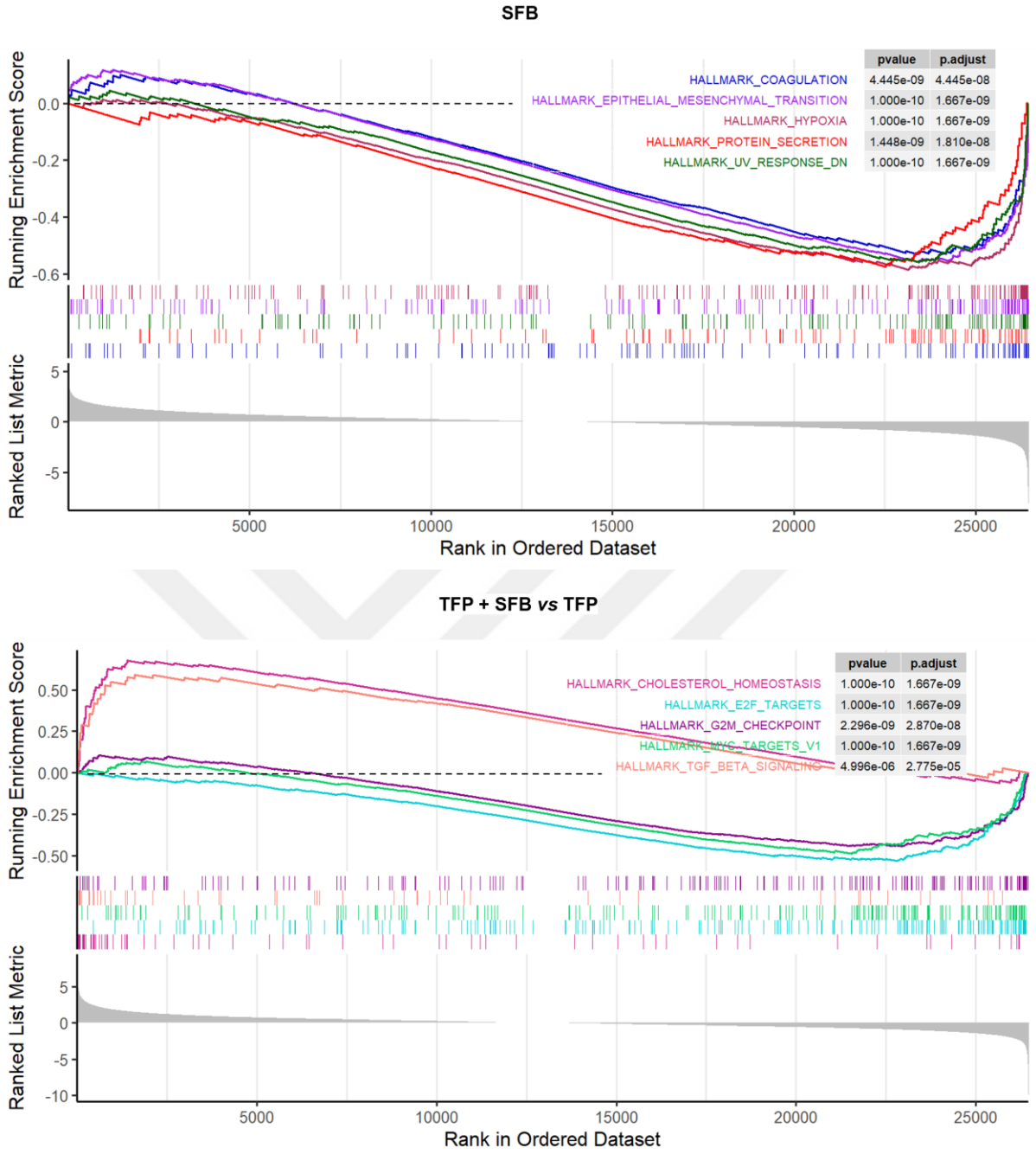

Figure 4.5. Visualization of top 5 gene set enrichment results using DESeq2 statistics covering log2 fold-change values and standard error ($SFB_{2.5\ \mu M}$ vs DMSO, $TFP_{10\ \mu M}$ + $SFB_{2.5\ \mu M}$ vs $TFP_{10\ \mu M}$; p-value < 0.05 enrichment cutoff).

Genes within the top enriched pathways by SFB treatment were investigated further by their log2 fold change values in all contrasts (TFP vs DMSO, SFB vs DMSO, TFP + SFB vs DMSO, TFP + SFB vs TFP, and TFP + SFB vs SFB) for investigating the leading genes that account for SFB driven effects, and their modulation by TFP. Therefore, heatmaps of genes having the statistical significance threshold of $p < 0.05$ for SFB vs DMSO within the hypoxia and EMT gene sets were generated (Figure 4.6). It was seen that the majority of hypoxia associated genes were downregulated by SFB, and *PDK1*, *NDRG1*, *SLC2A1*, *LDHA*, *KDM3A*, *PGK1*, *GBE1*, *KLF7*, *CA12*, *DTNA*, *BNIP3L*, *TGFBI*, and *GAPDH* were further downregulated significantly by the combinatorial treatment with TFP. On the other hand, the expression levels of a smaller cluster of genes, including *SDC2*, *PAM*, *KLF6*, *FOXO3*, and *BHLHE40* were seen to be rescued upon the combinatorial treatment. Among EMT associated genes significantly upregulated by SFB, either a significant downregulation (*FZD8*, *ITGA2*, *NT5E*) or a non-significant modulation that approaches downregulation by the combinatorial treatment was observed. Among downregulated genes by SFB, some of them (*SCG2*, *MYL9*, *LUM*, *TIMP1*, *SNAI2*, *CALU*, *TPM4*) were significantly upregulated while some of them (*COL1A1*, *MEST*, *GJA1*, *FBN1*, *TGFBI*, *VIM*, *MYLK*, *FSTL1*, *TGM2*, *SPARC*) were further downregulated upon combinatorial treatment.

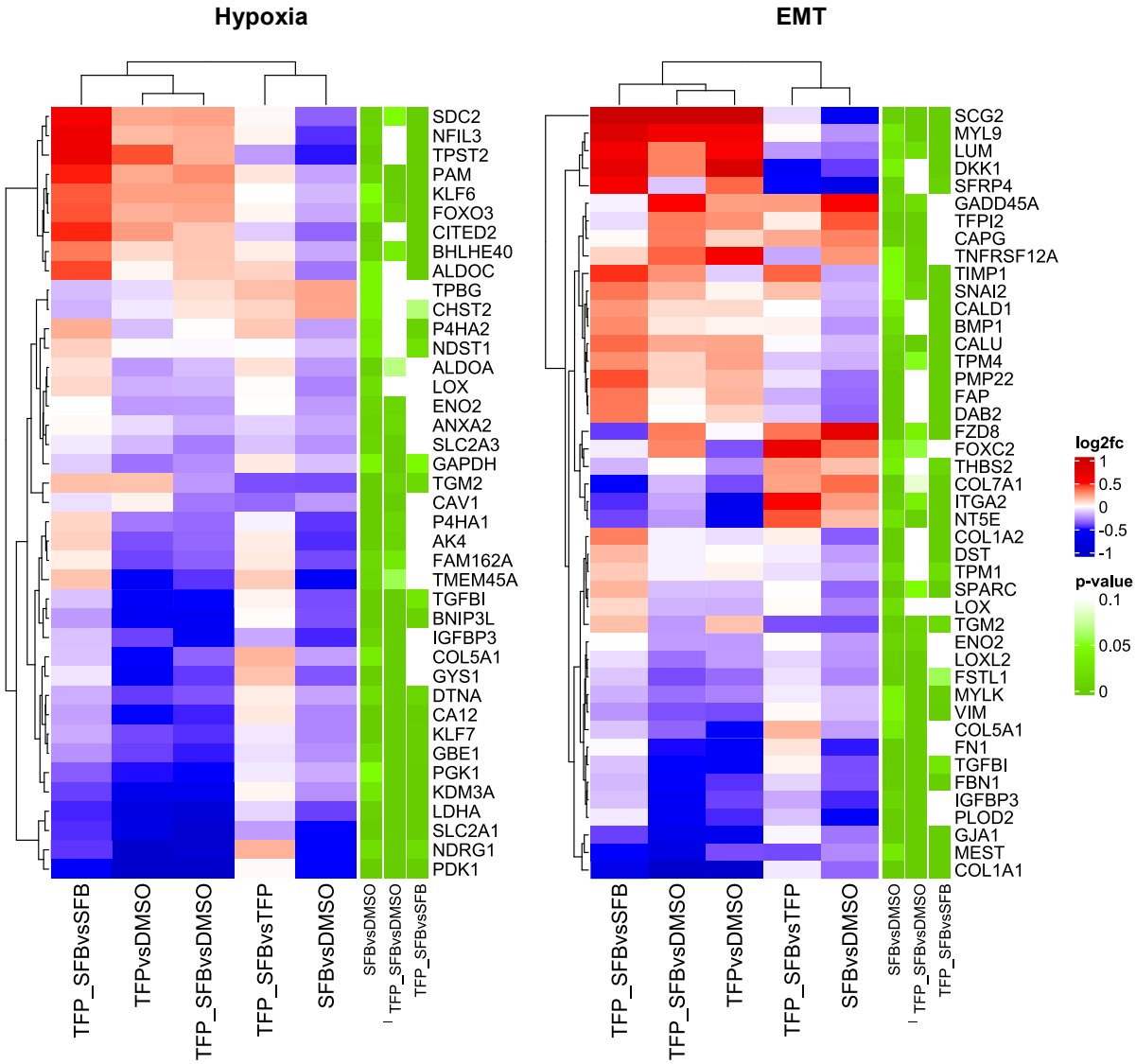

Figure 4.6. Log_2 fold-change heatmaps of significantly modulated (p-value < 0.05 for $SFB_{2.5\ \mu M}$ vs DMSO) MSigDB hypoxia *(M5891)* and epithelial to mesenchymal transition *(M5930)* gene sets among samples.

4.1.2 Trifluoperazine-Driven Effects

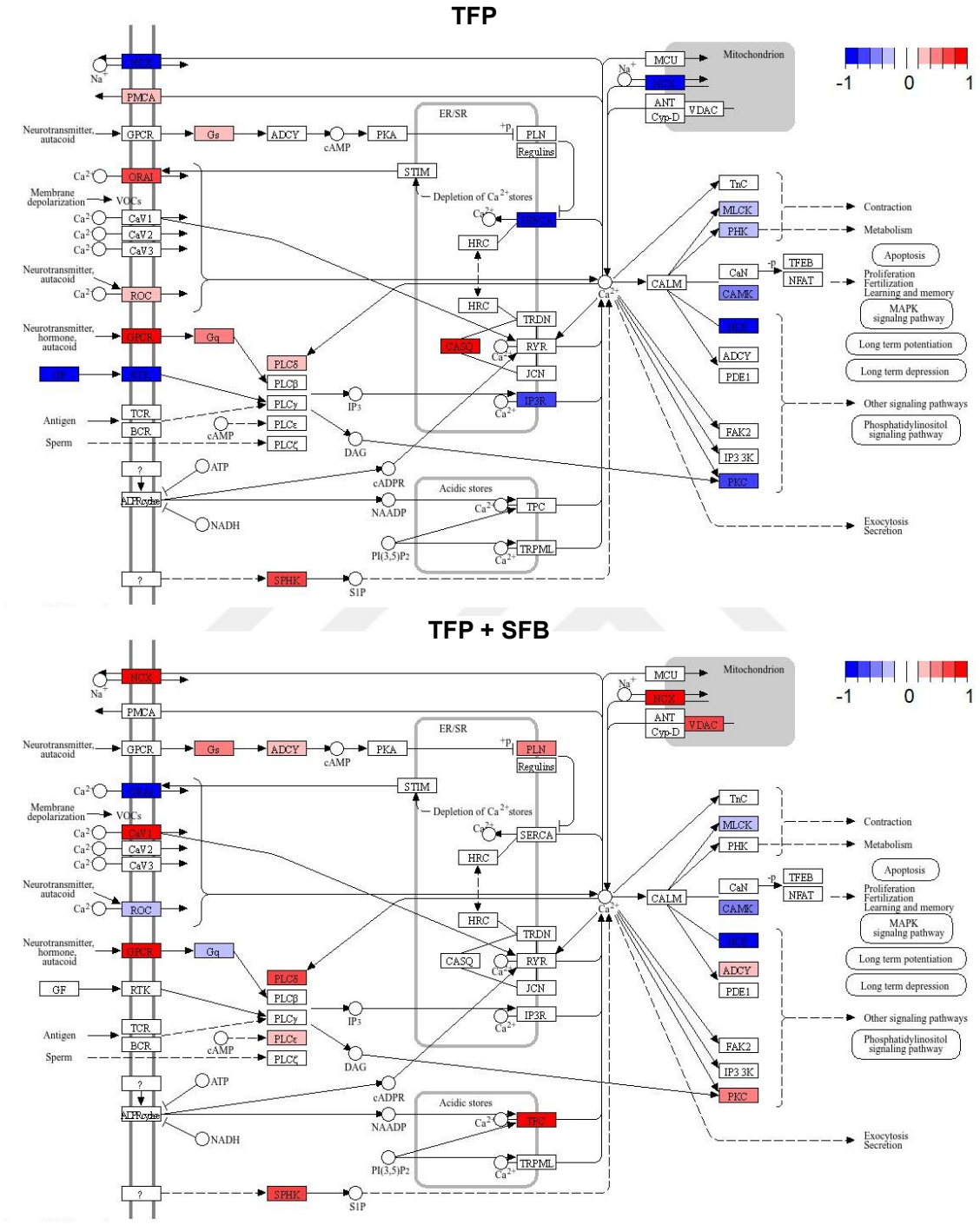

Figure 4.7. KEGG calcium signaling pathway (hsa04020) components color coded by log2 fold-change values ($TFP_{10\,\mu M}$ + $SFB_{2.5\,\mu M}$ vs DMSO and $TFP_{10\,\mu M}$ vs DMSO; p-value < 0.05).

The Kyoto Encyclopedia of Genes and Genomes (KEGG) calcium signaling pathway components were visualized based on their log2 fold change values for TFP alone and TFP + SFB to highlight the relevance of this pathway due to the role of TFP as a CaM antagonist that directly interferes with calcium signaling (Figure 4.7). Given its targeted impact, mapping the differential expression of calcium signaling pathway components was aimed to provide insight into its mechanistic effects and how they may be involved in suppressing cell viability upon combinatorial treatment. As anticipated, TFP was seen to significantly reduce the expression of IP3R and CaM downstream effectors including MLCK, PHK, CAMK, NC6, and PKC. Upon TFP + SFB combinatorial treatment, PLC gamma, PLC epsilon, ADCY and PKC were seen to be upregulated, yet still under the influence of dysregulated CaM signaling.

Given the TFP driven upregulation of cholesterol homeostasis and mTORC1 components (Figure 4.3), their differential expression levels among all contrasts were visualized by a heatmap for genes that are significantly modulated by TFP with a p value threshold of 0.05 (Figure 4.8). *ACAT2*, *MVD*, *FASN*, *FDPS*, *FDF1*, and *ACSS2* were observed to be further significantly upregulated by TFP + SFB compared to TFP alone among cholesterol homeostasis components while *DHCR24* and *G6PD* were, among mTORC1 signaling pathway components. *FADS2*, *HMGCS1*, *DHCR7*, *SQLE*, *HMGCR*, *TMEM97*, and *EBP* were involved in both pathways in the same trend.

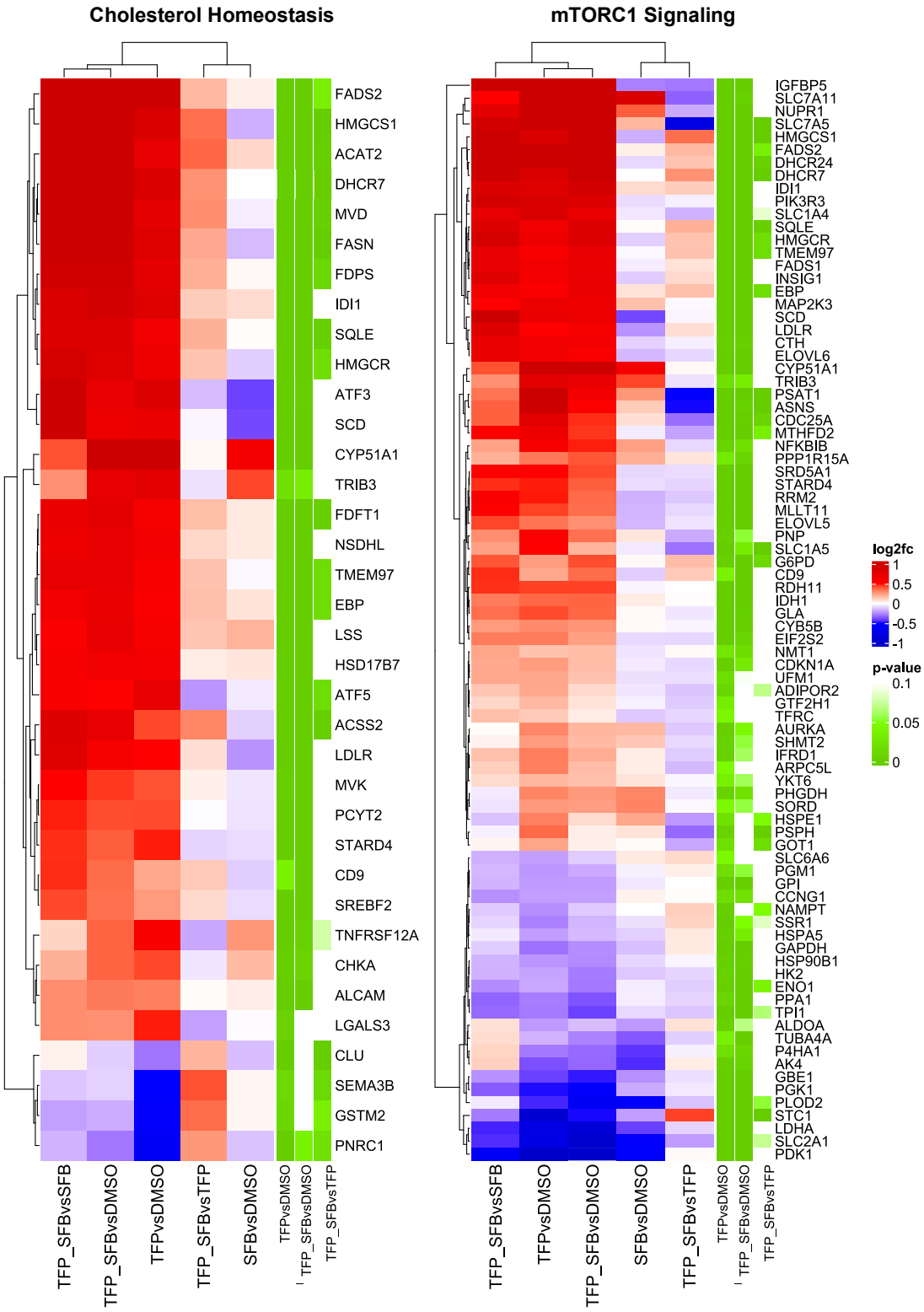

Figure 4.8. Log_2 fold-change heatmaps of significantly modulated (p-value < 0.05 for $TFP_{10\ \mu M}$ vs DMSO) MSigDB cholesterol homeostasis *(M5892)* and mTORC1 signaling *(M5924)* gene sets among samples.

4.2 Larval Zebrafish Toxicological Assessments for Trifluoperazine and Sorafenib

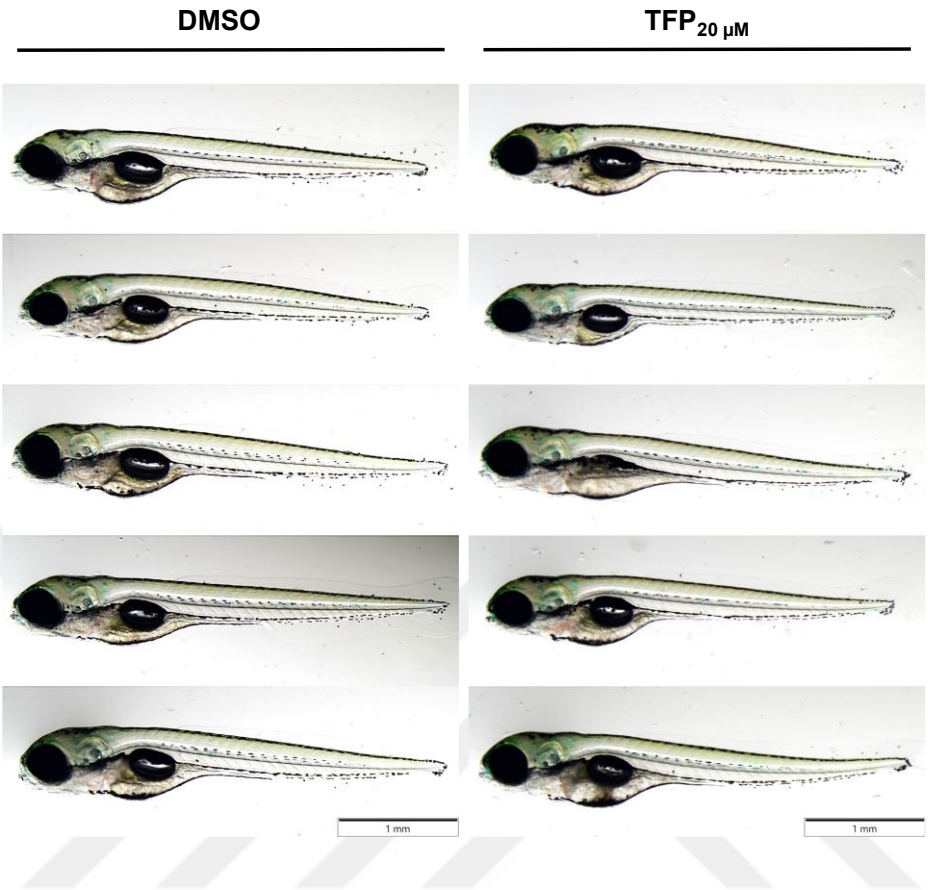

Figure 4.9. Bright field images of 5 dpf AB strain zebrafish larvae treated with DMSO control and $TFP_{20\mu M}$ for 72h; 3.2X magnification.

Figure 4.9 shows that 72h TFP exposure did not cause any developmental and morphological defects. 2 out of 24 larvae in the DMSO group, and 1 out of 24 larvae in the TFP group at 3 dpf, due to random causes. Hence, it was inferred that no striking toxicity was induced by TFP even at 20 µM, which was double the dose of interest.

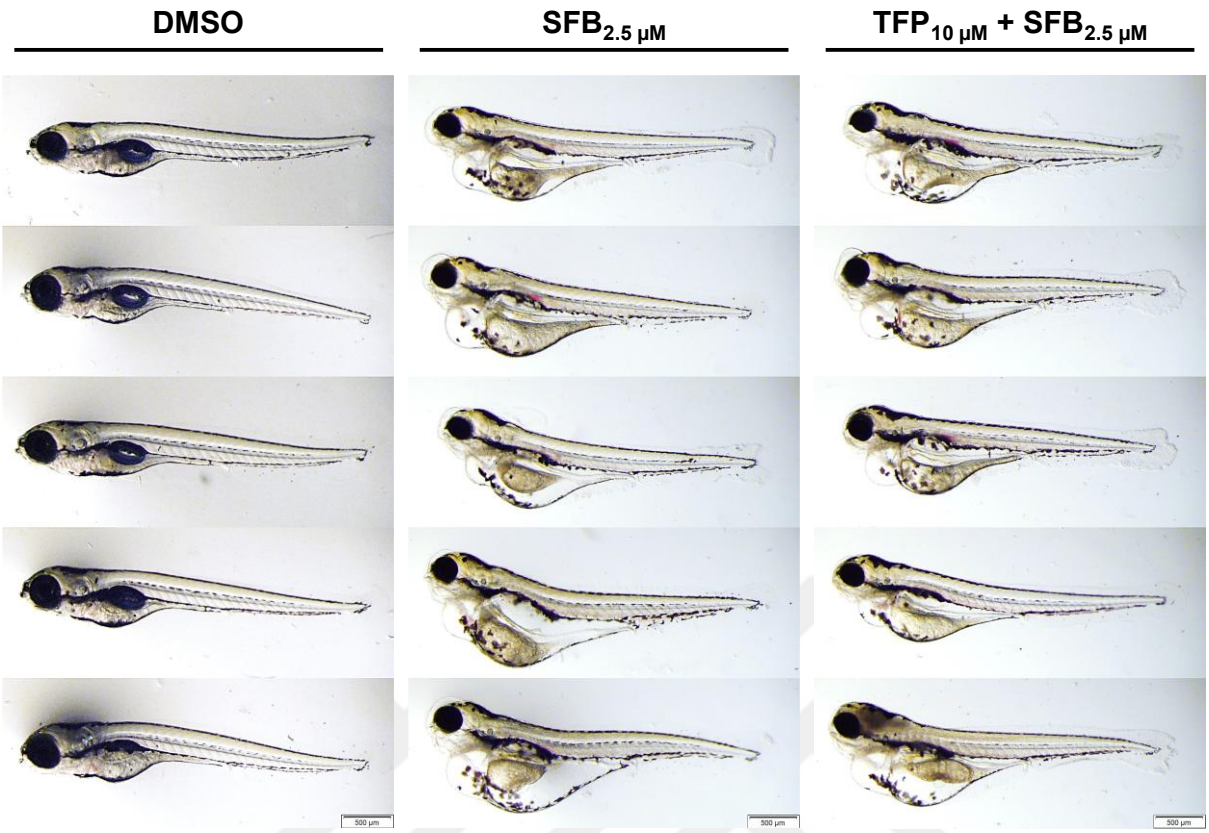

Figure 4.10. Bright field images of 5 dpf AB strain zebrafish larvae treated with DMSO control, $SFB_{2.5\ \mu M}$ and $TFP_{10\ \mu M}$ + $SFB_{2.5\ \mu M}$ for 72h; 3.2X magnification.

Figure 4.10 shows that 72h SFB exposure at 2.5 µM caused severe pericardial and yolk sac edema as well as body shortness in 100%, and periorbital edema in 40% of the treated AB wild type larvae (n = 48). Most of them were near dead, with 10% having tissues that had started to rot. There was no substantial difference between the group treated with SFB alone and the group treated with SFB in combination with 10 µM TFP, except that there were 2 more larvae having tissue rot in the combinatorial treatment group.

4.3 Impact of Kinase Inhibitors on U87-MG and A172 Cell Viability

A high-throughput drug screening assay was conducted on U87-MG and A172 cells using a predefined dose range of 2.5, 5, and 10 μM kinase inhibitors from the Cayman Kinase Screening Library. IC50 values were plotted with their sensitivity information, and AUC values were plotted with their standard errors for each drug on both cell lines (Figure 4.11). Among 157 drugs, 9 drugs had no impact on U87-MG cell viability, 26 drugs had no impact on A172 cell viability, and 20 drugs had no impact on the viability of either cell line. 12 drugs were highly effective at the target dose range of under 5 μM. The response curves of both lines for the effective drugs were shown in Figure 4.12, and their target kinase(s) and clinical information was stated in Table 4.1.

Among kinase inhibitors effective at low doses under 5 μM, staurosporine was seen to reduce the viability to near 0% at all concentrations used, hence the effective dose range was likely to be even lower than 2.5 μM on both cell lines. PIK-75 was also seen to reduce the viability to near 0% at all concentrations used on U87-MG cells, yet a slight resistance was observed at 5 and 10 μM in A172 cells, with a lower HillSlope value. The remaining 10 drugs induced similar percent cell viability reduction in U87-MG and A172 cells in all three doses. Most of them, including CRT0066101, CAY10626, Torin 1, Bisindolylmaleimide IX, NH125, and BMS 345541, were reported to remain in the preclinical stage, indicating early-stage investigation of their efficacy and safety. In contrast, R406 and AZD 7762 have advanced to clinical trials, with a maximum phase of 2 and 1, respectively. Notably, INK128 has progressed to phase 2 clinical trial, specifically in GBM, while volasertib has reached a maximum phase of 3 in acute myeloid leukaemia, highlighting its more advanced clinical evaluation.

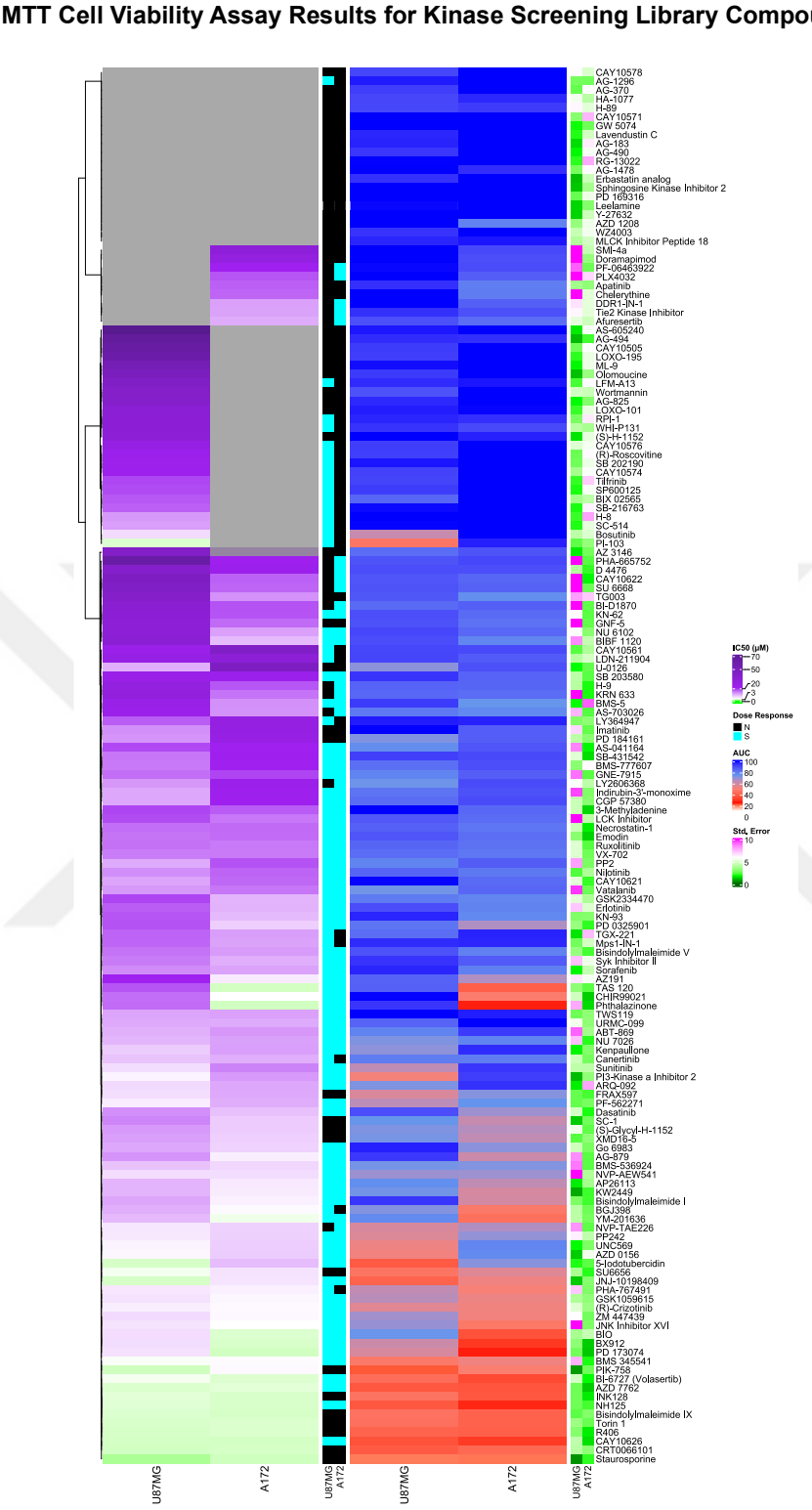

Figure 4.11. Impact of *Cayman Kinase Screening Library* compounds on U87-MG and A172 cell viability shown by IC_{50} values, dose sensitivity, and area under dose response curve (AUC) with standard errors calculated using 3 replicates each for 2.5, 5, and 10 μM compound treatment.

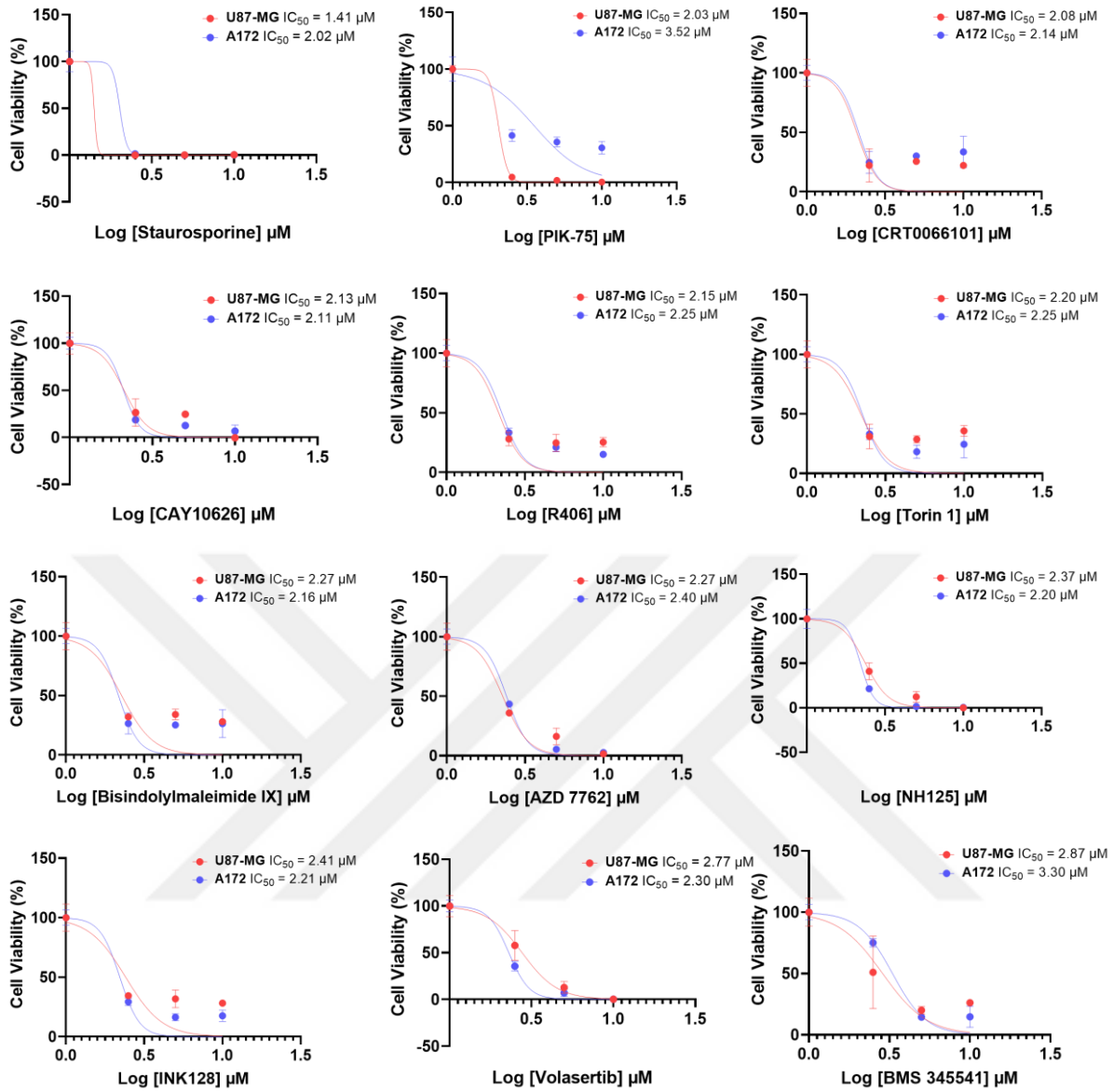

Figure 4.12. Dose response curve graphs of drugs from *Cayman Kinase Screening Library* compounds having IC_{50} values lower than 5 µM for both U87-MG and A172 cell lines.

Table 4.1. Targeted kinases by inhibitory drugs from *Cayman Kinase Screening Library* compounds having IC_{50} values lower than 5 μM for both U87-MG and A172 cell lines.

Inhibitory Drug	Target Kinase(s)	Clinical Information
Staurosporine	PKC (serine/threonine kinase)	Preclinical
PIK-75	PI3K p110α/γ	Preclinical
CRT0066101	PKD (serine/threonine kinase)	Preclinical
CAY10626	PI3Kα/mTOR	Preclinical
R406 (Tamatinib)	Syk (tyrosine kinase)	Max Phase: 2 (GBM -)
Torin 1	mTOR (serine/threonine kinase)	Preclinical
Bisindolylmaleimide IX	GSK3/PKC (serine/threonine kinase)	Preclinical
AZD 7762	Chk1/2 (serine/threonine kinase)	Max Phase: 1 (GBM -)
NH125	eEF2K/CAMKIII (serine/threonine kinase)	Preclinical
INK128 (Sapanisertib/MLN0128)	mTOR (TORC1/2) (serine/threonine kinase)	Max Phase: 2 (GBM Phase 1)
Volasertib (BI-6727)	PLK1 (serine/threonine kinase)	Max Phase: 3 (GBM -)
BMS 345541	IKKα/β (serine/threonine kinase)	Preclinical

4.4 Impact of Kinase Inhibitors in Combination with TFP on U87-MG Cell Viability

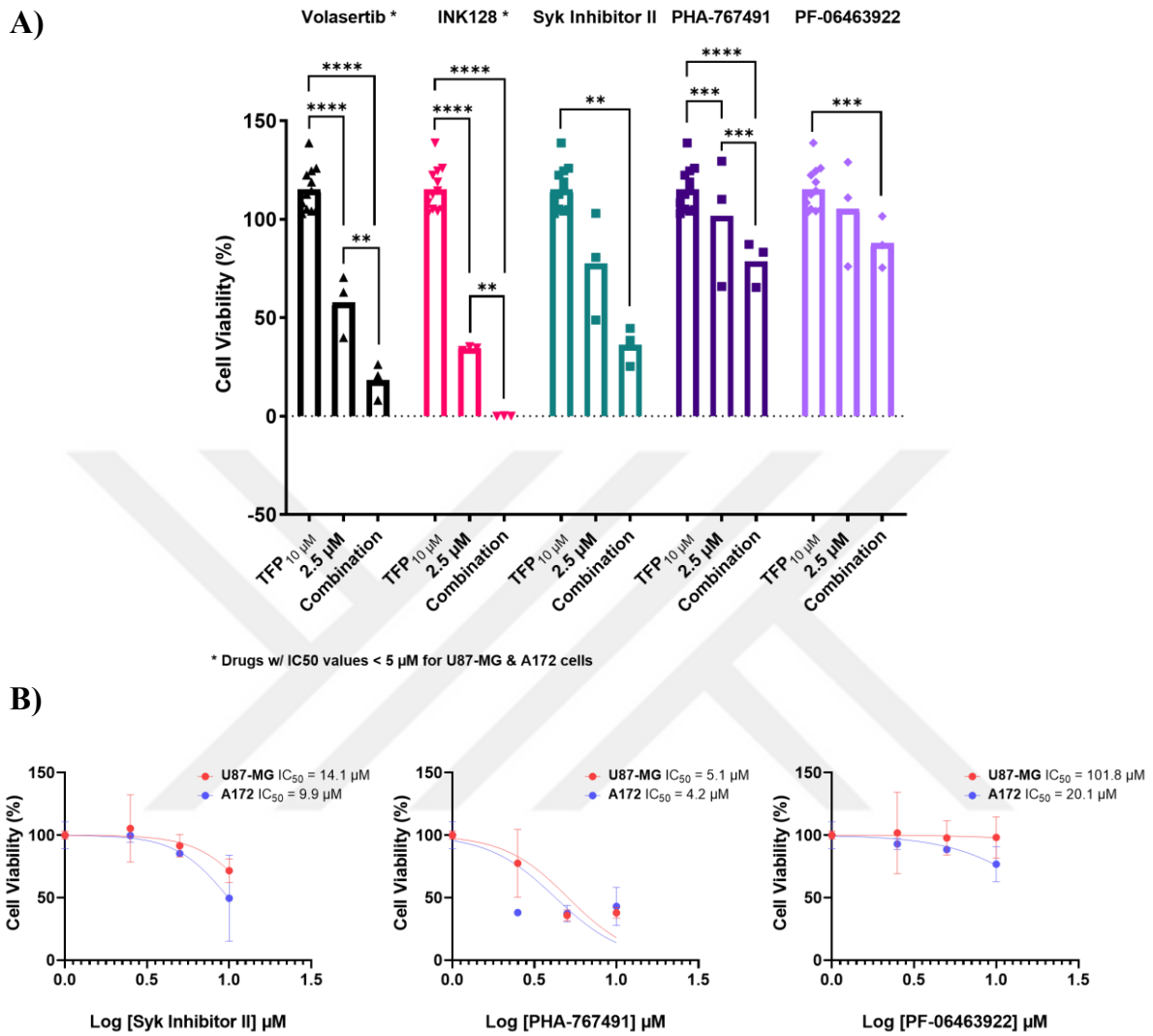

Figure 4.13. *Cayman Kinase Screening Library* (Plate 1) compounds exhibiting synergy with TFP$_{10\,\mu M}$. **A)** Bar plots showing percent cell viability of treated U87-MG cells. **B)** Dose response curve graphs of shown drugs among *Cayman Kinase Screening Library* compounds.

Kinase inhibitors from Plate 1 Kinase Screening library were administered in 2.5 μM in combination with 10 μM TFP, and 5 drugs among 80 were observed to synergistically reduce U87-MG cell viability, with high statistical significance of at least 0.006 adjusted p-value (PHA-767491) by two-way ANOVA, upon combinatorial treatment although TFP alone was

observed to slightly enhance cell viability at 10 μM (Figure 4.13A). It was seen that, among previously prioritized drugs by dose sensitivity at 2.5 μM, volasertib and INK128 were seen to be acting synergistically with TFP, and hence further prioritized for *in vivo* investigation. Figure 4.13B shows the IC50 curves of the remaining three drugs that further reduce U87-MG cell viability in combination with TFP compared to their single treatments.

Table 4.2. Targeted kinases by inhibitory drugs from *Cayman Kinase Screening Library* compounds acting synergistically with 10 μM TFP on U87-MG cell viability at 2.5 μM.

Inhibitory Drug	Target Kinase(s)	Clinical Information
PHA-767491	Cdc7 (serine/threonine kinase)	Preclinical
PF-06463922 (Lorlatinib)	ALK (tyrosine kinase)	Max Phase: Approved (GBM - ;Neuroblastoma Phase 3)
Syk Inhibitor II	Syk (tyrosine kinase)	Preclinical

The preclinical drug, Syk Inhibitor II, and the FDA approved anaplastic lymphoma kinase (ALK) inhibitory drug for metastatic non-small cell lung cancer (NSCLC), PF-06463922, did not significantly impact U87-MG cell viability alone, as they had higher estimated IC50 values of 14.1 and 101.8 μM respectively, but reduced it to 87.9% and 78.6% respectively in combination with TFP. The preclinical Cdc7 inhibitory drug, PHA-767491, reduced the cell viability to 77.5% on average when administered alone, while it reduced further to 36.1% when in combination with TFP, and with higher statistical significance.

Figure 4.14. Dose response matrices with ZIP synergy scores for *Cayman Kinase Screening Library* (Plate 1) compounds exhibiting synergy with TFP$_{10\,\mu M}$.

Figure 4.14 shows the percent inhibition matrices of drugs at 2.5, 5 and 10 µM without TFP, 2.5 µM in combination with 10 µM TFP, and TFP alone. Missing values were imputed by the estimated calculations of the *SynergyFinder* scoring model. Volasertib exhibited a percent inhibition of 81.75 in combination with TFP, with a high ZIP synergy score of 35.55. INK128 had higher percent inhibition both alone and in combination with TFP, yet its ZIP synergy score,

14.06, was lower compared to that of volasertib. Although the remaining drugs had less impact on cell viability, they had relatively high ZIP synergy scores with TFP, all three of them being above 25.

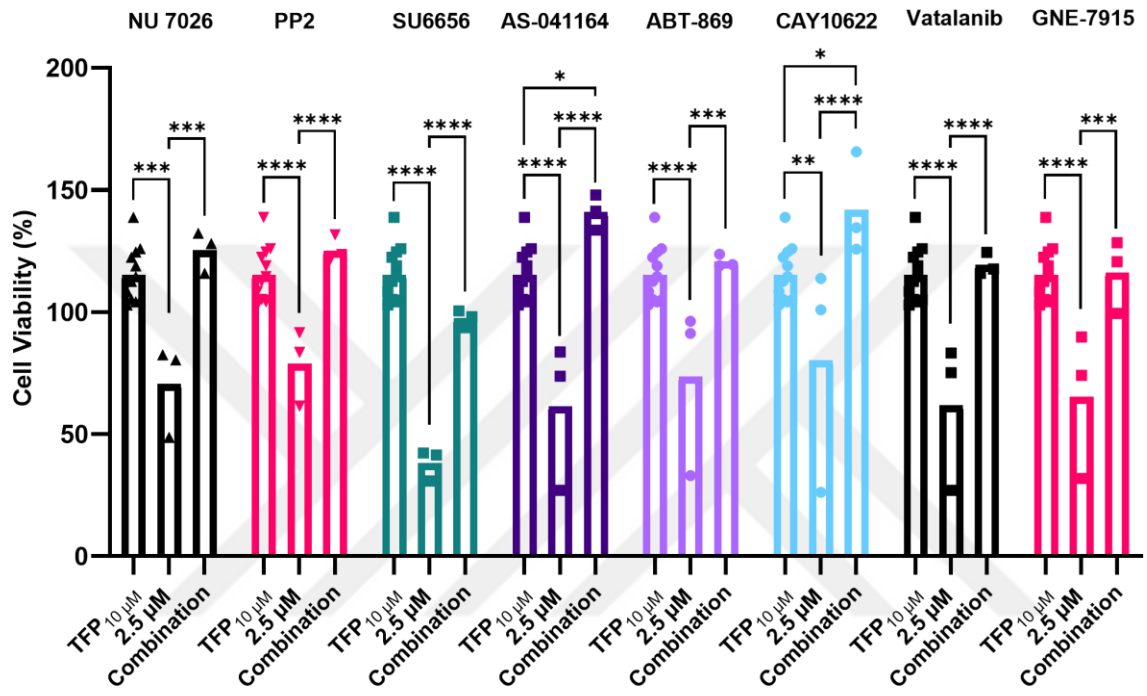

Figure 4.15. Bar plots showing percent cell viability of U87-MG cells treated with $TFP_{10\,\mu M}$ and/or *Cayman Kinase Screening Library* (Plate 1) compounds that significantly reduce cell viability when administered alone but exhibit significantly reversed effects in combination with $TFP_{10\,\mu M}$.

Drugs that significantly reduce U87-MG cell viability by their single treatment at 2.5 µM, but not in combination with 10 µM TFP, were shown in Figure 4.15. The preclinical drugs, NU7026, PP2, and GNE-7915 significantly reduced cell viability to 70.5%, 78.8%, and 65.2% respectively when administered alone, but the impact was reversed significantly by combinatorial treatment. Similarly, ABT-869 that has reached a maximum phase of 3 in clinical

trial for hepatocellular carcinoma, and Vatalanib that has reached a maximum phase of 3 in clinical trials for colorectal neoplasms and phase 2 trials for GBM, lost their inhibitory effect significantly in combination with TFP. The preclinical drugs, AS-041164 and CAY10622 reduced cell viability, yet they enhanced cell proliferation further in TFP co-treatment even compared to the single treatment with TFP, with adjusted p-values of 0.022 and 0.016 respectively.

The target kinases of the drugs were provided in Table 4.3 for the evaluation of potential antagonistic interactions and potential crosstalk between their downstream pathways and TFP's mechanism. Targets included the DNA-dependent protein kinase (DNA-PK) that is involved in DNA damage repair, the proto-oncogenic Src family of kinases involved in cell survival, the G protein-coupled receptor-activated phosphoinositide 3-kinase gamma (PI3Kγ) that is involved in the regulation of immune stimulation or suppression, the vascular endothelial growth factor receptor (VEGFR) and platelet derived growth factor receptor (PDGFR) that are involved in angiogenic signaling, the rho-associated coiled-coil-containing protein kinase (ROCK1/2), and the leucine-rich repeat kinase 2 (LRRK2). These results may elucidate the nature of TFP-mediated drug resistance in contrast with the synergy induced by different types of kinase inhibitors. However, drug prioritization was done regarding effective kinase inhibitors in a low micromolar dose range that act synergistically with 10 μM TFP.

Table 4.3. Targeted kinases by inhibitory drugs from *Cayman Kinase Screening Library* compounds that significantly reduce U87-MG cell viability at 2.5 μM alone, but have reversed impact in combination with 10 μM TFP.

Inhibitory Drug	Target Kinase(s)	Clinical Information
NU 7026	DNA-PK (serine/threonine kinase)	Preclinical
PP2	Src (tyrosine kinase)	Preclinical
SU6656	Src (tyrosine kinase)	Preclinical
AS-041164	PI3Kγ	Preclinical
ABT-869	VEGFR/PDGFR (tyrosine kinase)	Max Phase: 3 (GBM -)
CAY10622	ROCK1/2 (serine/threonine kinase)	Preclinical
Vatalanib	VEGFR (tyrosine kinase)	Max Phase: 3 (GBM Phase 2)
GNE-7915	LRRK2 (tyrosine kinase-like)	Preclinical

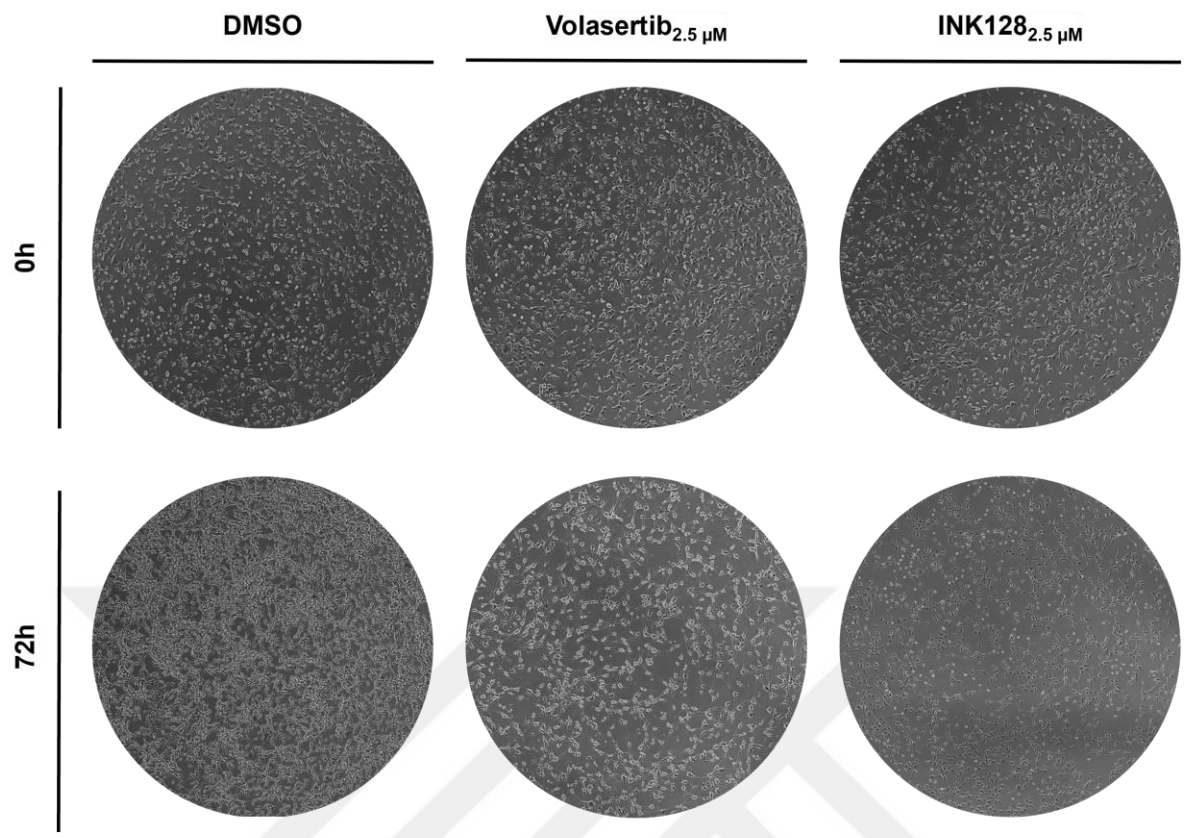

Figure 4.16. Phase contrast images of U87-MG cells treated with DMSO control, Volasertib$_{2.5\mu M}$, or INK128$_{2.5\mu M}$ for 72h; 4X magnification.

As seen in Figure 4.16, 72h treatment with volasertib at 2.5 μM caused an evident reduction in cell density compared to DMSO control with more rounded cellular shape that potentially indicates cell stress or mitotic arrest, which align with its known role as a PLK1 inhibitor, disrupting cell cycle progression and inhibiting proliferation. 72h treatment with INK128 at 2.5 μM caused more severe inhibition of proliferation with cells appearing spaced out and potentially undergoing detachment, which also align with its function as an mTOR inhibitor suppressing cell growth and inducing apoptosis. Based on these pronounced phenotypic effects and its prognostic signature, volasertib was prioritized for detailed mechanistic studies and subsequent in vivo evaluation in larval zebrafish models.

4.5 Survival Analysis on TCGA-GBM Cohort Using Sorafenib and Volasertib Induced Gene Signatures

RNA-seq data was generated for U87-MG cells treated with 2.5 μM volasertib using the same pipeline as for 2.5 μM sorafenib to obtain SFB and VOL gene signatures by differentially expressed genes with absolute log2FC > 1.5 and $p < 0.05$ for both dataset, and to use them for evaluating their clinical relevance (Figure 4.17). When SFB (80 upregulated, 41 downregulated genes) and VOL (239 upregulated, 940 downregulated genes) gene signatures were scored in 372 TCGA-GBM samples by GSVA and composite signature scores were grouped based on cohort median expression into High and Low, log rank testing showed that the sorafenib signature did not separate patient survival (log rank $p = 0.75$), whereas patients with a high volasertib signature experienced significantly longer overall survival compared to the low group (log rank $p = 0.0071$).

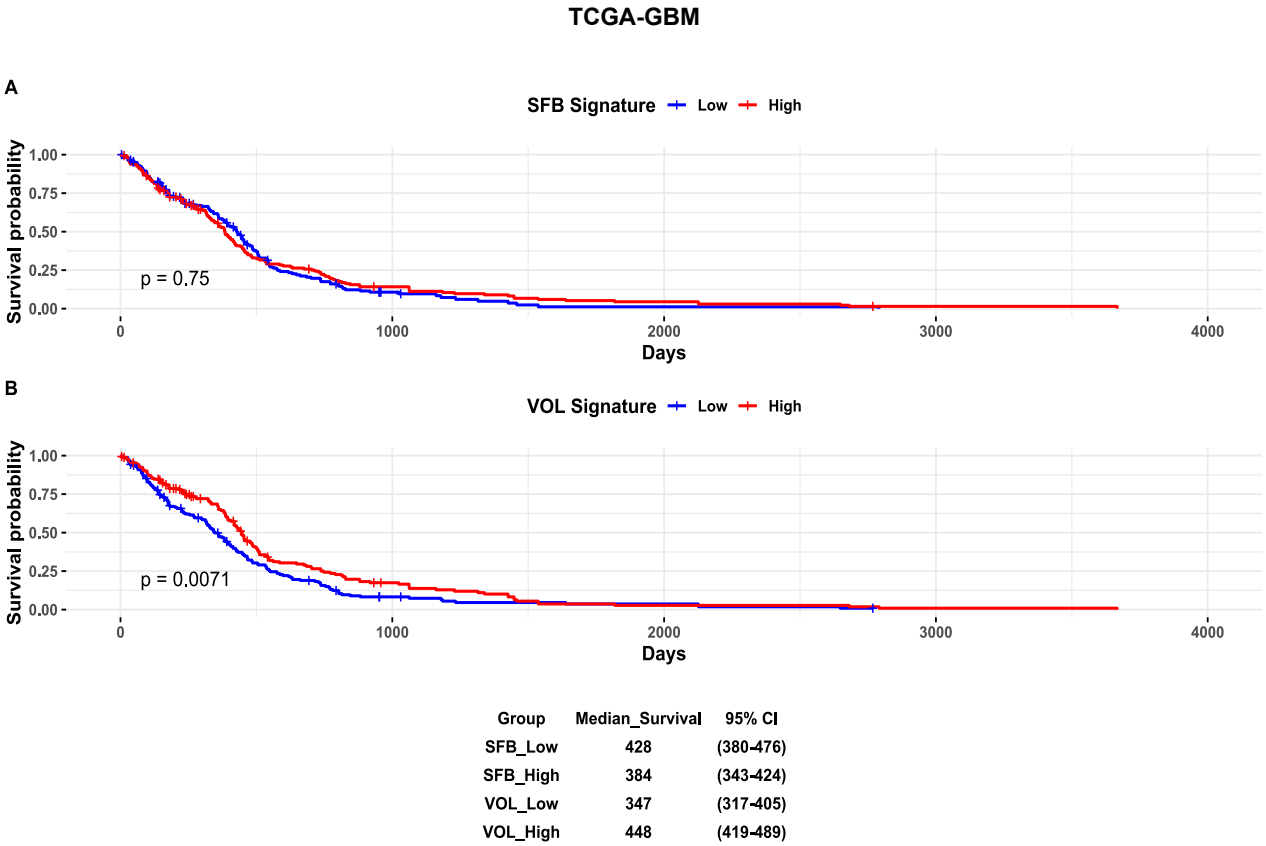

Group	Median_Survival	95% CI
SFB_Low	428	(380-476)
SFB_High	384	(343-424)
VOL_Low	347	(317-405)
VOL_High	448	(419-489)

Figure 4.17. Kaplan-Meier curves from survival analysis of **A)** 2.5 µM sorafenib vs DMSO (SFB) and **B)** 2.5 µM volasertib (VOL) vs DMSO gene signatures in TCGA-GBM cohort.

4.6 Larval Zebrafish Toxicological Assessments for Prioritized Drugs

Effective drugs prioritized from cell viability assays were evaluated for their toxicity similarly on AB wild type larvae (Figure 4.18). INK128, SU6656 and Volasertib at 2.5 µM did not cause any phenotypic difference that indicates toxicity. Treatment with Volasertib in combination with 10 µM TFP also did not cause any aberrant morphological change and stress phenotype (Figure 4.19).

Figure 4.18. Bright field images of 5 dpf AB strain zebrafish larvae treated with DMSO control, $INK128_{2.5\ \mu M}$, $SU6656_{2.5\ \mu M}$, $Volasertib_{2.5\ \mu M}$ for 72h; 3.2X magnification.

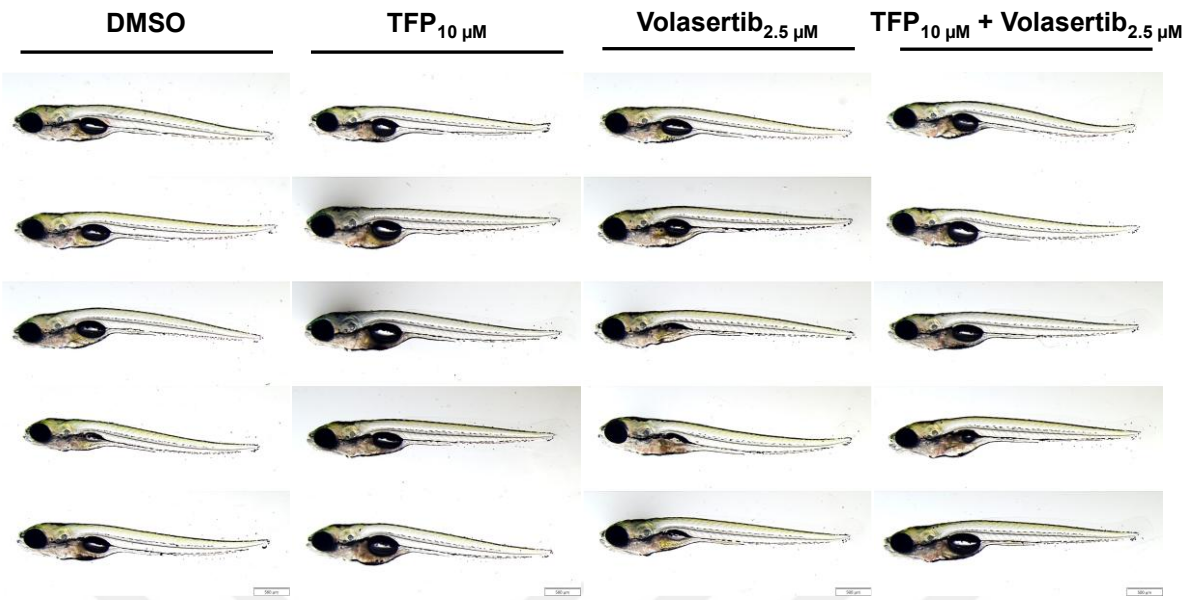

Figure 4.19. Bright field images of 5 dpf AB strain zebrafish larvae treated with DMSO control, $TFP_{10\ \mu M}$ and/or $Volasertib_{2.5\ \mu M}$ for 72h; 3.2X magnification.

4.7 Fluorescence Screening for Larval Zebrafish GFAP Expression

The GFP reporter expressing GFAP transgenic zebrafish larvae were evaluated by the ratio of their log2-transformed fluorescent signal measurements before and after drug treatment for investigating the pharmacological effect on zebrafish astrocytes. Volasertib treatment at 1.25 and 2.5 μM did not significantly alter the GFP signals compared to those from DMSO control group larvae, quantified from the 2D lateral images at 2 and 5 dpf (Figure 4.20).

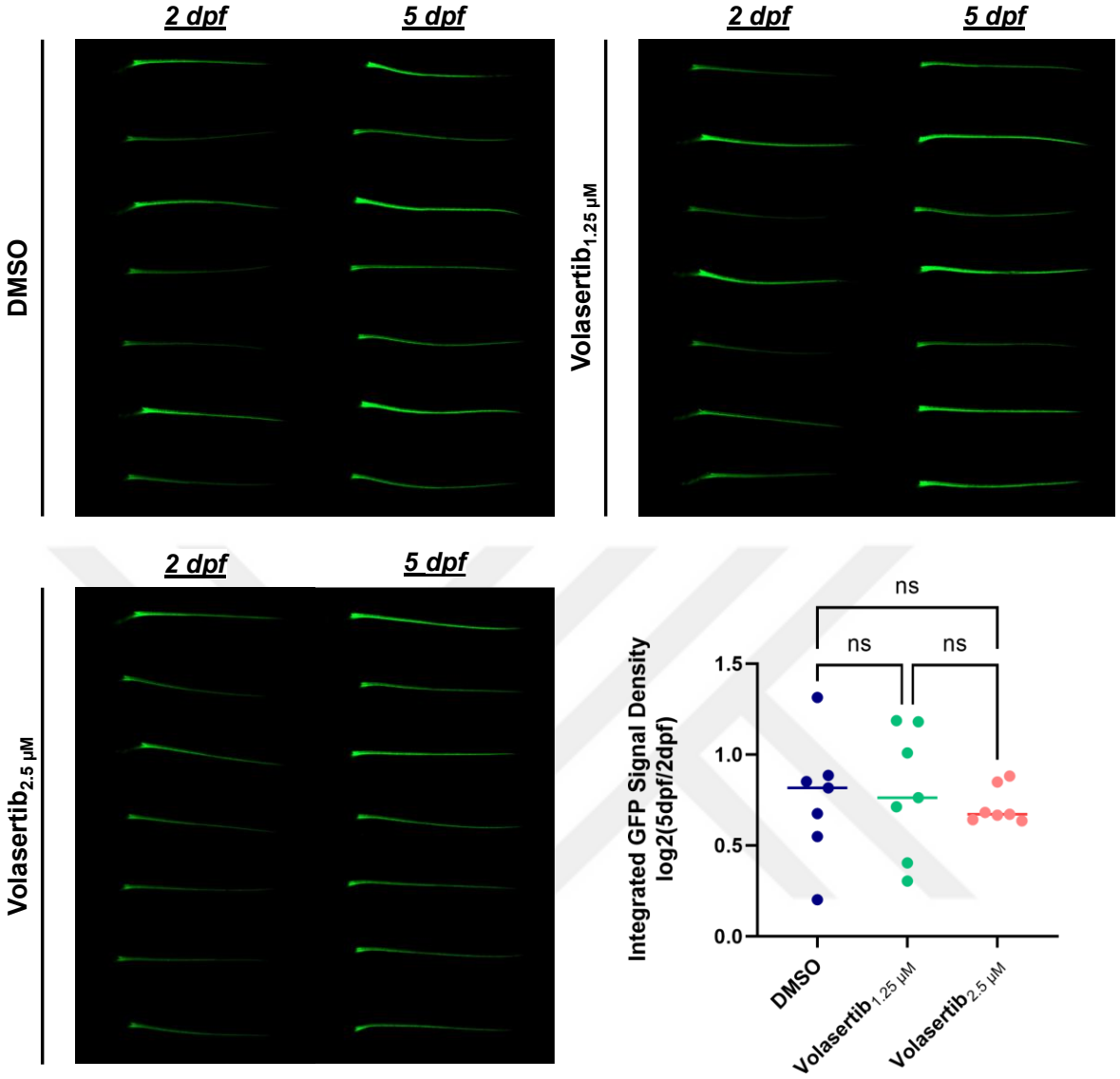

Figure 4.20. Fluorescent images of 5 dpf Tg(*gfap*:GFP) strain zebrafish larvae treated with DMSO control, Volasertib 1.25 µM and 2.5 µM for 72h; 3.2X magnification.

4.8 Development of LDexplore as an Automated Analysis Platform for Larval Zebrafish Locomotion Assays

An interactive web application, *LDexplore: ZANTIKS MWP Locomotion Tests on Zebrafish Larvae*, was developed using the R Shiny framework to facilitate streamlined visualization and statistical analysis of larval zebrafish locomotion data recorded using the *Zantiks MWP* system.

The application was structured into four primary tabs, designed to sequentially guide the user through data handling and analysis. The *Home* tab provided a comprehensive overview describing the capabilities and purpose of the automated analysis platform (Appendix Figure 7.1). The *Search* tab allowed users to browse a curated table of 19 published locomotion studies from 2007 to 2024, focused on light-dark assays, and review detailed schematics of established *Zantiks* protocols (Appendix Figure 7.2). The *Visualize* tab was designed for users to upload raw data files exported as CSV from the *Zantiks* system, along with custom group annotation files detailing the experimental layout of the 96-well plates. Uploaded data were reactively ingested, displayed dynamically in an interactive, scrollable table, and subsequently passed to plotting functions (Appendix Figure 7.3). The *Analyze* tab encompassed two distinct analytical modules for comprehensive data interpretation. First, a period boxplot module was implemented to visualize activity metrics across defined experimental periods. Second, a period specific distance-time graph was developed, incorporating corresponding slope comparisons with ANCOVA statistical assessments and pairwise trend comparisons. The application's server logic, which continuously monitored user inputs, enabled sequential steps of data upload, exploration, visualization, and interpretation. Collectively, these features established a reproducible analytical environment tailored for high-throughput behavioural phenotyping of 4-6 days post-fertilization zebrafish larvae in a standardized 96-well plate format.

4.8.1 Larval Zebrafish Locomotion Assays for Toxicological Assessment

Using the *Zantiks MWP* system, 5 dpf AB wild-type larvae exposed to 5, 10, or 20 µM TFP for 72 hours were monitored under alternating 10-minute dark and bright periods and a 30-second startle light pulse in between, in the scope of the *Startle Response Model* (Appendix Figure 7).

Figure 4.21A presents a heatmap of distance travelled by each larva in 30-second time bins, with white indicating no movement and red indicating maximal movement. The x-axis time legend was colour coded, black for *DARK* periods and red for *BRIGHT* period and light induction, allowing visualization of instantaneous responses. It was seen, from side bar annotations denoting treatment groups, that although DMSO vehicle treated controls were enriched in clusters of low movement and 20 µM TFP treated larvae formed small clusters of heightened locomotion, all larval groups remained intermingled across clusters, indicating no pronounced separation of locomotor profiles. The distance-time graph shown in Figure 4.21B depicted that 5 dpf larvae displayed a normal swimming pattern of a baseline velocity in the initial 10-minute *DARK* period, followed by a significantly reduced velocity in the *BRIGHT* period, and a heightened velocity in the following *DARK* period with slight deceleration. The *STARTLE LIGHT* stimulus induced an instantaneous stillness before the *FINAL DARK* period that started with a peak velocity and had a higher deceleration rate compared to the second *DARK* period. 20 µM TFP treated larvae had the highest velocity peaks in both *BRIGHT-DARK* and *STARTLE LIGHT-DARK* transitions compared to 0, 5, and 10 µM TFP treated larvae. Figure 4.21C presents boxplots of total distance travelled by each larval group across each period. DMSO group larvae exhibited highly significantly lower total distance in every interval compared to all three TFP treated groups ($p < 0.001$). Variability in travelled distances were greatest during the *DARK II* and *FINAL DARK* periods. Notably, in the *BRIGHT* phase, characterized by generally low locomotion, 5 µM TFP treated larvae showed significantly higher activity than both vehicle controls and the 10 µM and 20 µM groups ($p < 0.05$). A similar pattern was observed in the *DARK I* baseline period. No significant difference was observed between 10 µM and 20 µM TFP treated larvae at *DARK* periods although maximum peaks were higher in the 20 µM group.

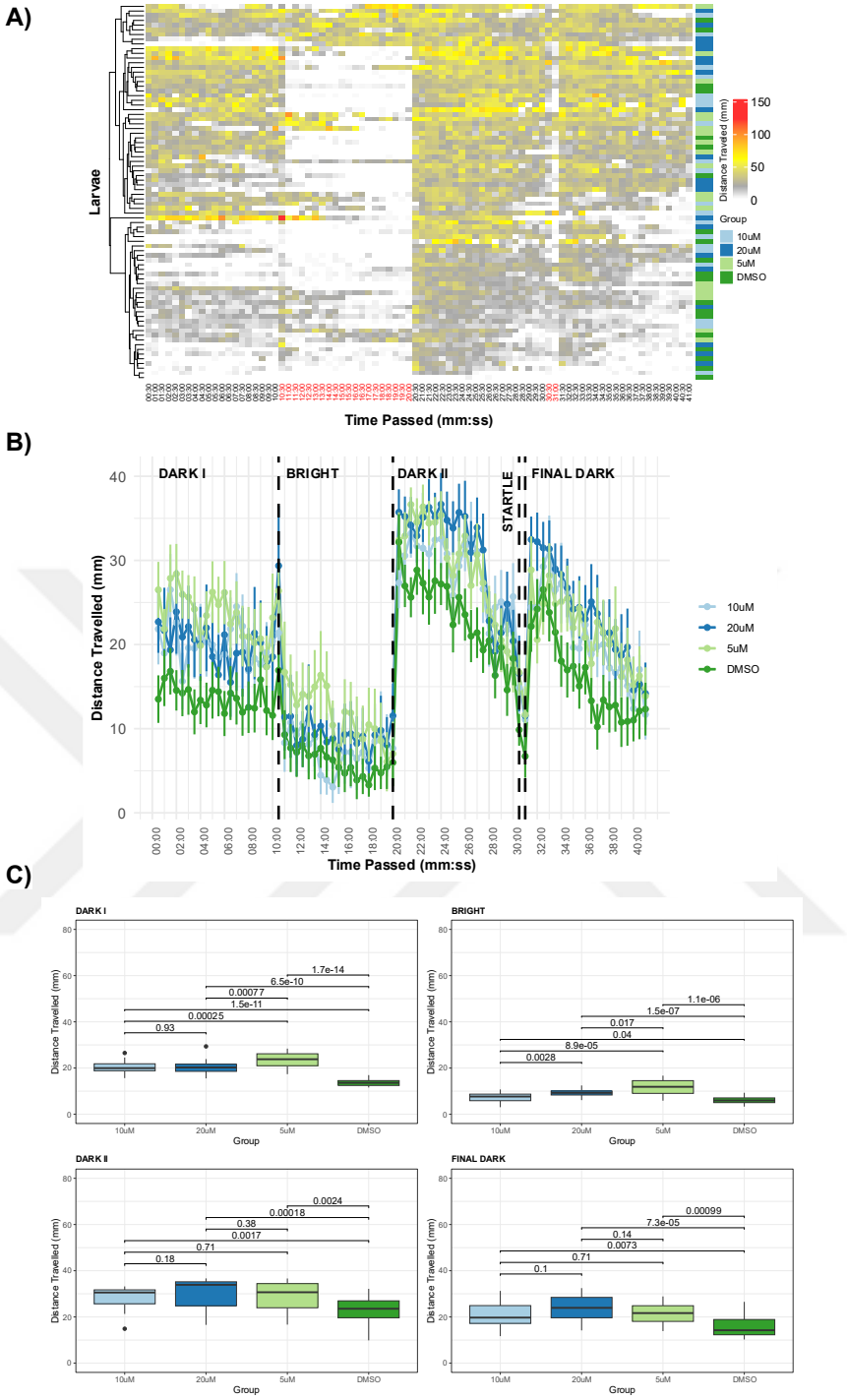

Figure 4.21. Locomotion assay results from Startle Response Model using Zantiks MWP system for 72h TFP exposed 5 dpf AB strain larvae at 5, 10, and 20 µM. **A)** Clustered locomotion heatmap of distance travelled per time bin for individual larva. **B)** Distance-time graph of larval groups with standard error. **C)** Boxplots for total distance travelled by each larval group across periods with student's t-test results; from Shiny app output. ($n_{DMSO} = 20$, $n_{5\ \mu M} = 19$, $n_{10\ \mu M} = 20$, $n_{20\ \mu M} = 21$)

The deceleration trends of each larval group during each *DARK* period were quantified by fitting linear slopes to the velocity curves (Figure 4.22). Analysis of covariance (ANCOVA) was used to test whether these slopes differed significantly across treatment groups, while pairwise estimated marginal trend comparisons were performed to identify which specific group differences reached significance. In the *DARK I* baseline period, which is followed by a 10-minute acclimation under dark without data collection, deceleration slopes for all groups were near zero and the ANCOVA yielded an F value of 0.96 ($p > 0.05$), indicating no significant difference in baseline locomotor slowing among DMSO and TFP treated larvae. During *DARK II* which starts from the transition immediately following the 10-minute *BRIGHT* phase, the absolute magnitude of deceleration was greatest in the 5 µM TFP group, followed by the DMSO control group. The ANCOVA F value increased to 2.27, with the p value approaching significance, suggesting a differential swimming trend across treatments. Pairwise comparisons implied that the 5 µM group decelerated more sharply than higher TFP doses, though they did not reach significance. In the *FINAL DARK* period, which starts immediately after the 30-second startle light stimulus, ANCOVA detected a significant effect of treatment on deceleration ($F = 3.17$, $p < 0.05$). Here, 20 µM TFP treated larvae exhibited the sharpest deceleration, followed by 10 µM and then 5 µM groups, before all treatments converged to a similar residual velocity of around 15 mm per 30 seconds. The increased deceleration in the *FINAL DARK* period for the 10 µM and 20 µM groups relative to *DARK II* reflects a dose dependent startle response, where the higher TFP concentration amplified the behavioural change post stimulus.

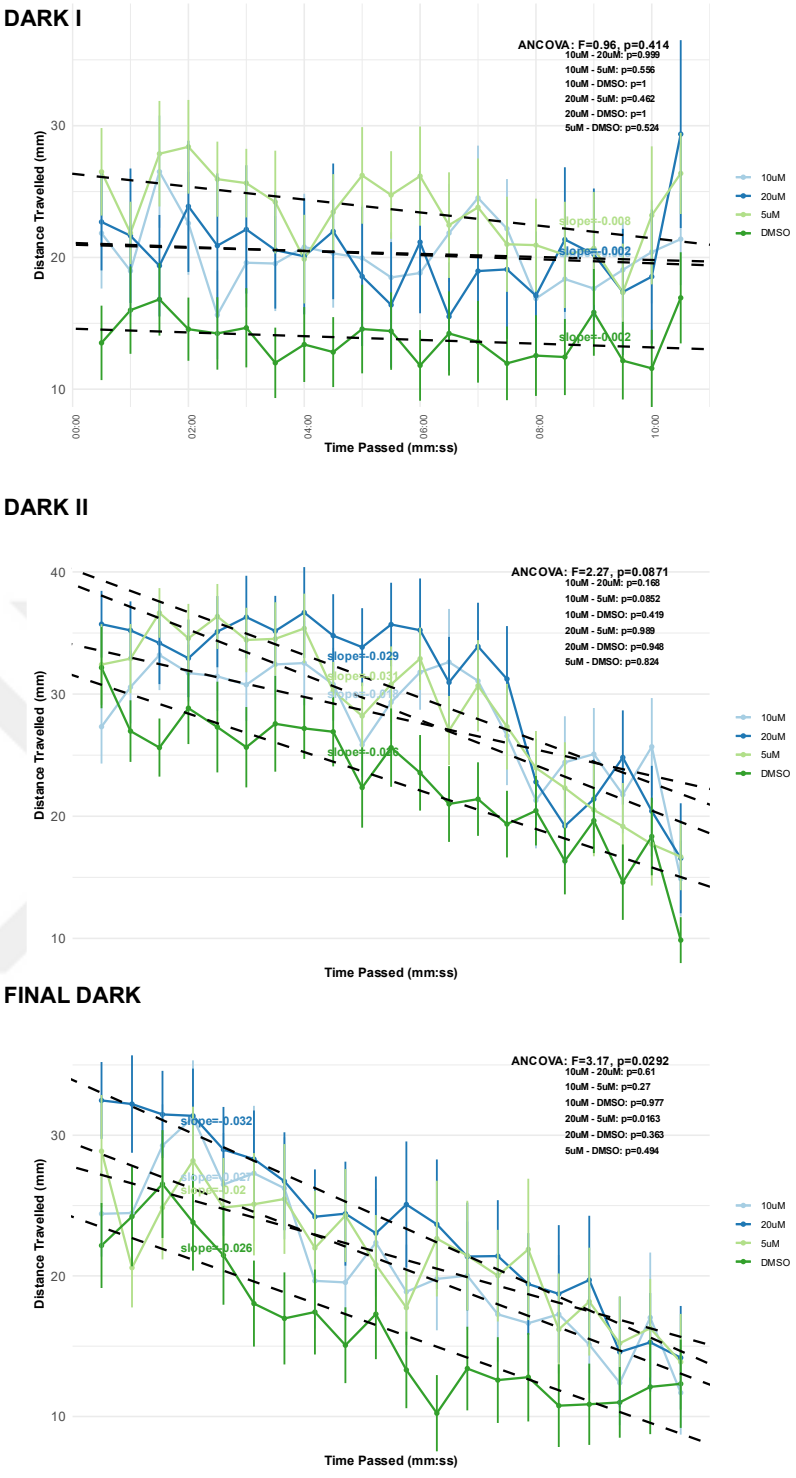

Figure 4.22. Locomotion assay results for deceleration patterns across DARK periods of 0 (DMSO), 5, 10, and 20 µM TFP treated larvae at 5 dpf, statistically tested by ANCOVA and pairwise estimated marginal trends; from Shiny app output. ($n_{DMSO} = 20$, $n_{5\ \mu M} = 19$, $n_{10\ \mu M} = 20$, $n_{20\ \mu M} = 21$)

Next, the same locomotion protocol was applied to another batch of 5 dpf AB wild-type larvae treated with 10 µM TFP, 2.5 µM volasertib, or their combination. In this assay, *DARK I* baseline velocities of both DMSO control and TFP groups were lower than those in the initial experiment, and neither group showed the typical deceleration upon transition to the *BRIGHT* period, highlighting inter-batch variability in unstimulated locomotor activity (Figure 4.23A). However, the overall swimming pattern in *DARK II* and the pronounced startle light induced deceleration in *FINAL DARK* closely mirrored earlier findings. Larvae treated with volasertib alone exhibited the highest baseline velocity, which dropped near zero during the *BRIGHT* phase, indicating robust sensitivity to light stimulus. Consistent with prior results, the TFP group maintained significantly greater activity than controls in the *BRIGHT* and *FINAL DARK* periods ($p < 0.05$). In *DARK II* and *FINAL DARK*, volasertib treated larvae swam significantly more than DMSO group ($p < 0.05$), although the TFP + VOL combination displayed higher variability and did not differ significantly from either monotreatment (Figure 4.23B).

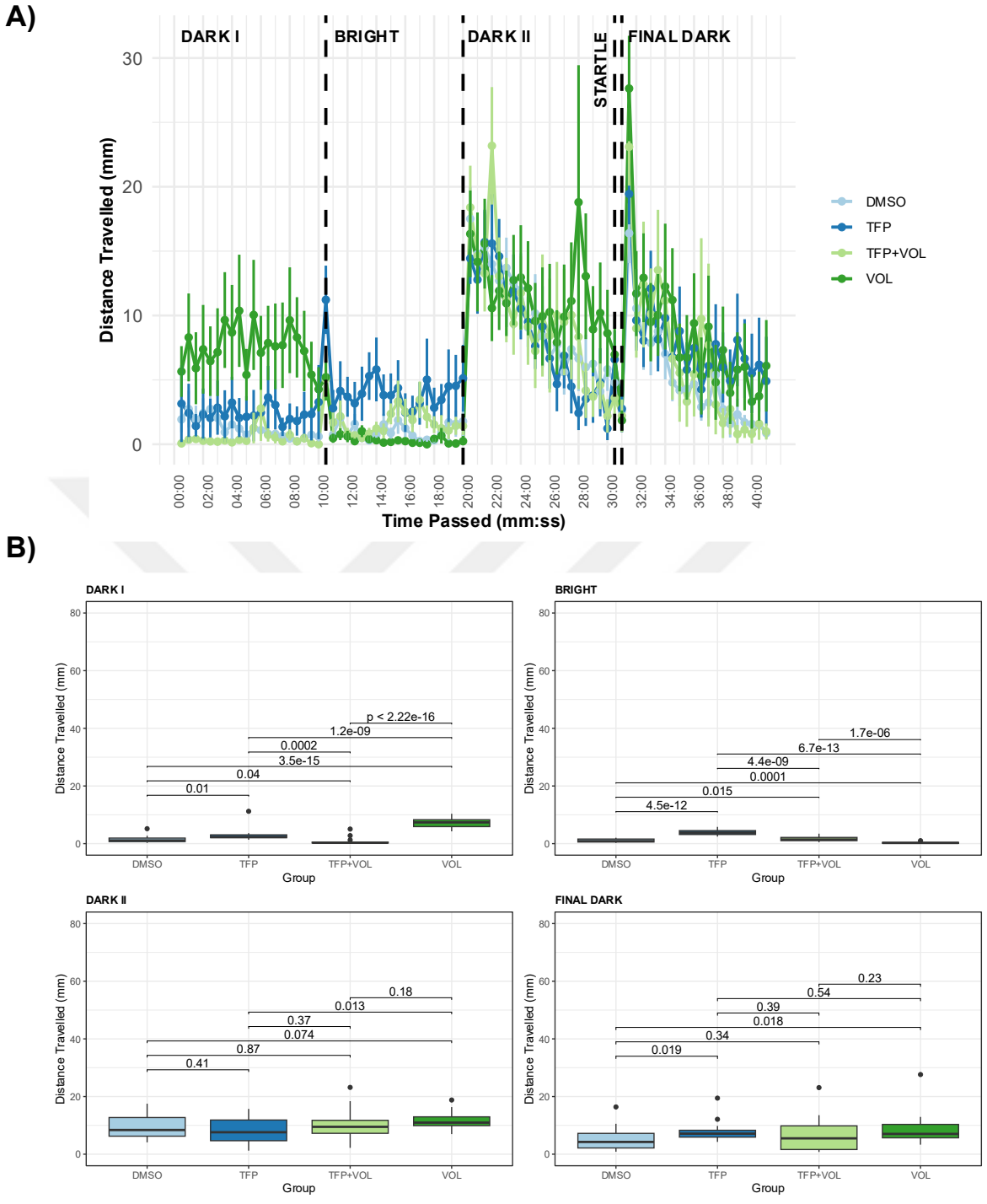

Figure 4.23. Startle Response Locomotion Assay results using Zantiks MWP system for 72h 10 µM TFP and/or 2.5 µM volasertib exposed 5 dpf AB strain larvae. **A)** Distance-time graph of larval groups with standard error. **B)** Boxplots for total distance travelled by each larval group across periods with student's t-test results; from Shiny app output. ($n_{DMSO} = 24$, $n_{TFP} = 20$, $n_{VOL} = 24$, $n_{TFP+VOL} = 21$)

4.9 Brain Orthotopic Larval Zebrafish Xenograft Model

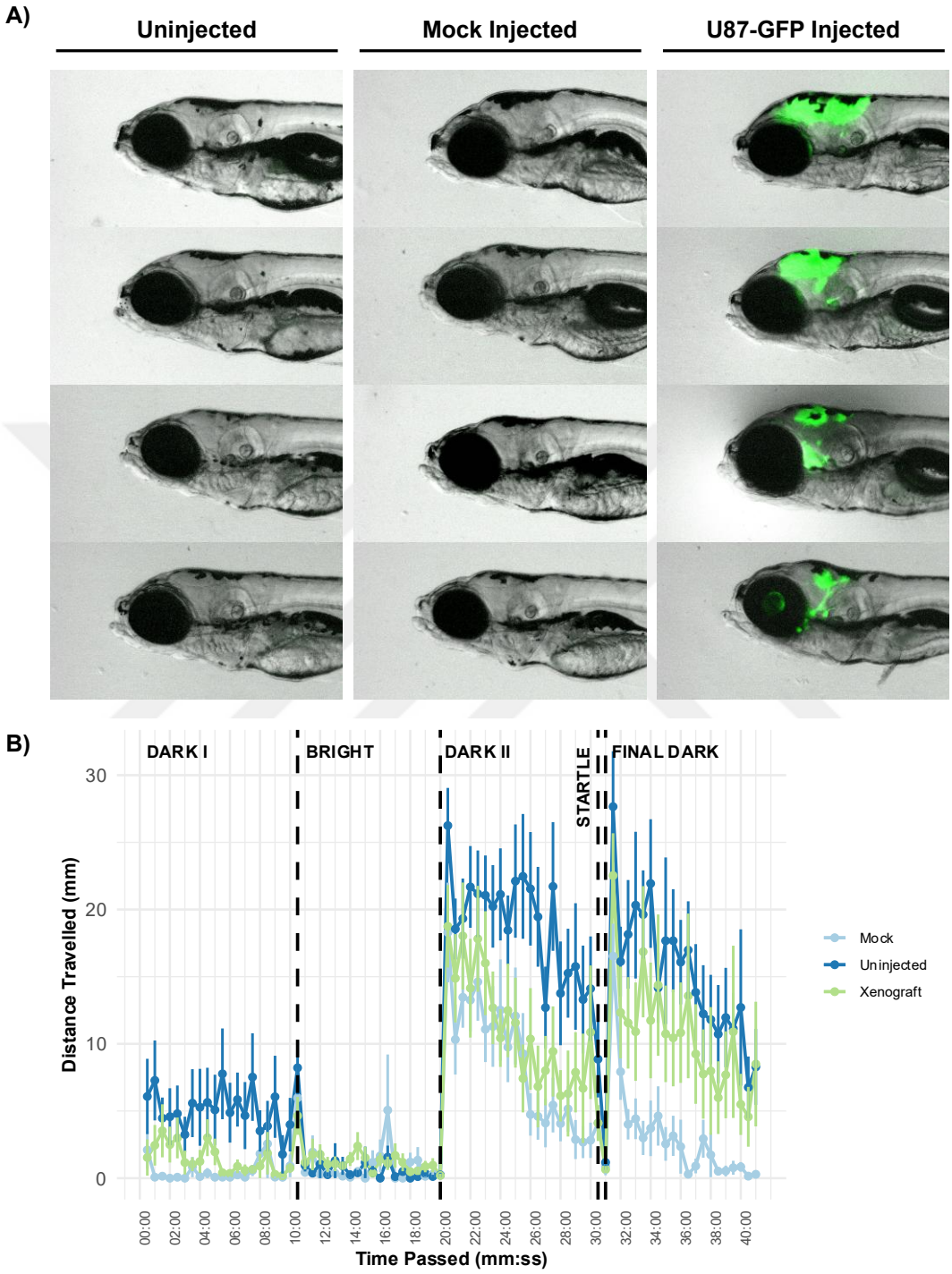

Figure 4.24. Brain orthotopic xenograft model. **A)** Bright field and fluorescent merged images of 5 dpf AB strain uninjected control, mock injected control, and U87-GFP microinjected zebrafish larvae (3 dpi); 8X magnification. **B)** Locomotion assay results at 5 dpf; from Shiny app output. ($n_{Uninjected} = 12$, $n_{Mock} = 20$, $n_{Xenograft} = 16$)

U87-GFP cells were successfully hosted by the larval zebrafish brain region for at least 3 dpi and no drastic developmental defect was observed in the mock or U87-GFP injected larvae, though some of them might have had slight damage in nearby tissues such as the eye (Figure 4.24A). The *Startle Response* locomotion assay was performed on the experimental groups grown at 32°C post microinjection. Results showed a reduced velocity of mock and U87-GFP injected larvae compared to uninjected larval group, which was observed to have a normal locomotion profile, in all three *DARK* periods (Figure 4.24B). Figure 4.25 validated that the uninjected larvae had significantly the highest total distance travelled in all *DARK* periods, and the mock injected group was observed to swim highly significantly less than the xenograft group only in the *FINAL DARK* period. Although sharp differences were observed among groups in terms of velocity, there was no significant difference in their deceleration pattern in any of the *DARK* periods.

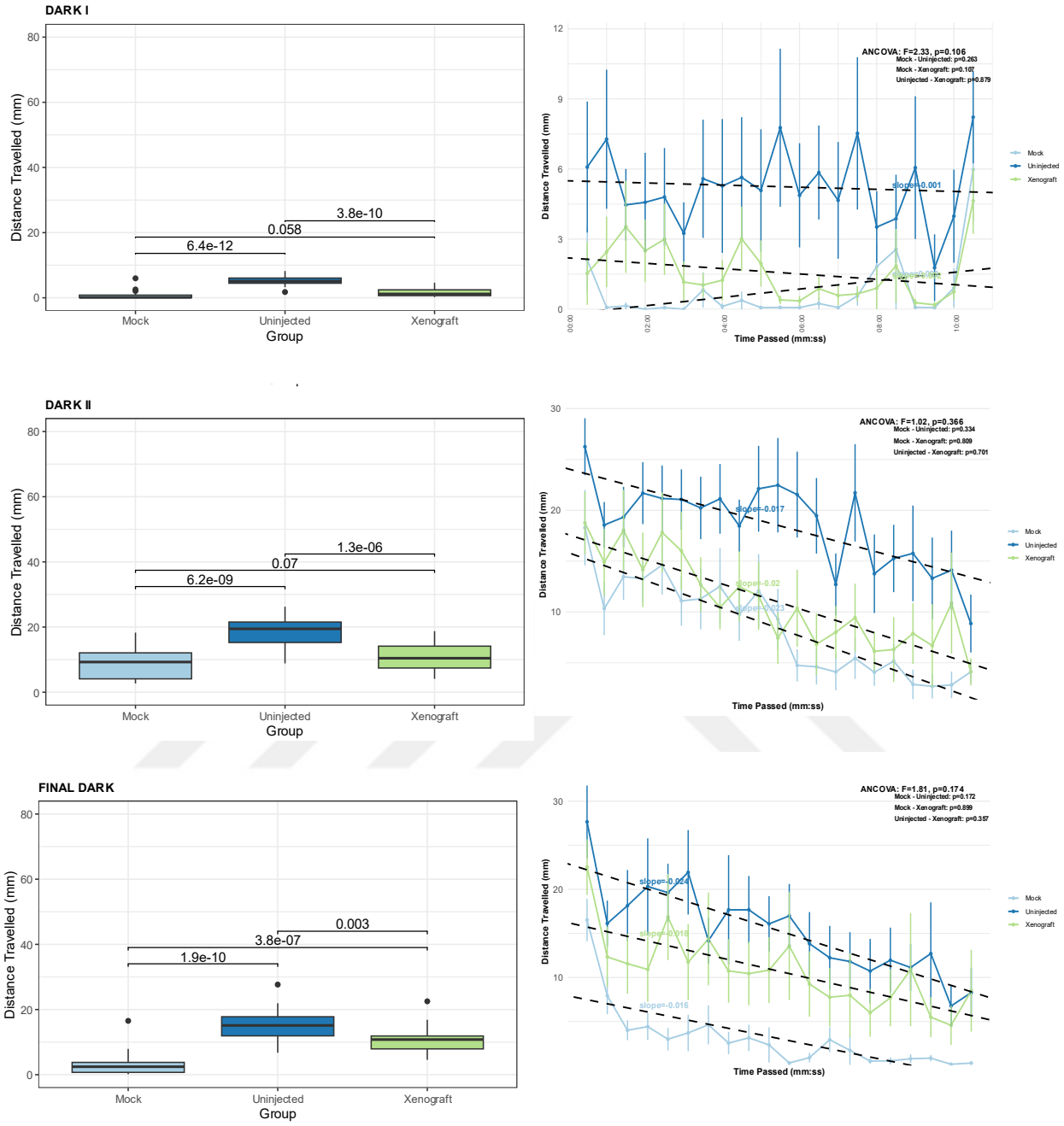

Figure 4.25. Locomotion assay results for total distance travelled (left) and deceleration patterns (right) across DARK periods of Uninjected, Mock, and Xenograft group larvae at 5 dpf, statistically tested by ANCOVA and pairwise estimated marginal trends; from Shiny app output. ($n_{Uninjected} = 12$, $n_{Mock} = 20$, $n_{Xenograft} = 16$)

5. CONCLUSION AND DISCUSSION

5.1 Transcriptional Profiles of Trifluoperazine and Sorafenib Treated U87-MG Cells

The investigation of RNA-seq data from TFP (10 μM) and SFB (2.5 μM), alone and in combination, treated U87-MG glioblastoma cells aimed to elucidate the mechanisms by which TFP acts synergistically with SFB, with the broader objective of understanding how TFP can be repurposed in combination with various kinase inhibitors. PCA analysis showed a clear clustering of replicates within each group, with close proximity of TFP and TFP_SFB groups, suggesting distinct but overlapping transcriptional responses that highlight the need for further investigation into the molecular mechanisms driving the synergy between TFP and SFB, particularly in the context of kinase inhibition strategies for glioblastoma therapy (Figure 4.1).

5.1.1 Trifluoperazine Modulates Essential Genes Involved in Metabolic Stress, Membrane Dynamics, and Drug Efflux

The differential gene expression analysis of each treatment group in contrast to the DMSO control group identified significant modulation of several *DepMap* essential genes, which are critical for cell survival and proliferation, making them particularly relevant for understanding drug-induced effects on glioblastoma cell viability (Shimada et al., 2021). The initial focus was on core essential genes that have been reported to be necessary for the survival of most cancer cell lines through CRISPR knockout screens, as they are typically involved in fundamental cellular processes and thus can facilitate the interpretation of the key targets that render cancer cells vulnerable to the repurposed drugs. TFP alone at 10 μM was shown to be slightly promoting U87-MG cell viability without statistical significance, but in repeated cell viability assay results, and the upregulation of *FADS2*, *PSAT1*, *SLC7A5*, *HRAS* by it aligned

well with the observed enhanced proliferation (Güneş Tok, MSc Thesis, Figure 4.2). Fatty acid desaturase 2 (FADS2) is a catalyser of the synthesis of polyunsaturated fatty acids (PUFA) with a critical role in membrane dynamics, and was shown to play role in glioblastoma tumour microenvironment (TME) adaptation (Korbecki et al., 2020). Phosphoserine aminotransferase 1 (PSAT1) is a critical enzyme in serine biosynthesis that was shown to have reduced expression in schizophrenia patients, and elevated expression in glioblastoma cells under metabolic stress conditions as hypoxia and glutamine deprivation, indicating a role in cancer cell adaptation (Ozeki et al., 2011; Tanaka et al., 2021). Hence, its upregulation highlights the effect of TFP in modulating glioblastoma cell metabolism besides its efficacy in its antipsychotic property. The L-type neutral amino acid transporter 1 (SLC7A5) is a critical mediator of essential amino acid, most notably leucine, uptake into cells thus its upregulation implies an increased efflux which in turn leads to mTORC1 activation that promotes proliferation, translational activations, and resistance to autophagy (Jewell et al., 2013; Milkereit et al., 2015). It was shown that GBM cell lines including U87-MG with increased levels of SLC7A5 were correlated with heightened mTORC1 activity and sustained survival under nutrient stress and hypoxia (Ozawa et al., 2021; X. Wang et al., 2022). HRAS, among the Ras GTPase family, is activated under tight regulation of guanine nucleotide exchange factors (GEFs) and GTPase-activating proteins (GAPs) upon RTK ligand binding to initiate the RAF-MEK-ERK signaling axis that promotes cell survival and EMT, as well as the PI3K/AKT signaling that promotes proliferation and protein synthesis (Shu et al., 2020). The upregulation of HRAS could be explained by a homeostatic response upon the disruption of the calcium/CaM signaling by TFP that could indirectly reduce GAP activity, thus downstream HRAS activity, by the inhibition of CaM binding to EGFR (Berchtold & Villalobo, 2014). Although protein levels would be needed for more precise understanding, the upregulation of these critical essential genes in cells, with slightly enhanced viability, shows that TFP alone at

10 μM could even be tumour promoting instead of inhibitory to cancer progression. On the other hand, the significant downregulation of *ABCC3*, *ITPK1* and *PRKCZ* suggested potential disruptions in drug efflux, inositol phosphate metabolism, and cellular survival mechanisms in glioblastoma cells, which was explanatory to the cell viability inhibitory effect of TFP on U87-MG and A172 cells at higher doses as 20 μM (Güneş Tok, MSc Thesis). ATP-binding cassette subfamily C member 3 (ABCC3) is a drug efflux transporter that is involved in the export of xenobiotics, as pharmaceutical compounds, and metabolites out of cells, and was reported to be associated with increased glioblastoma drug resistance when overexpressed, particularly to TMZ treatment (Shen et al., 2025). Therefore, its downregulation may imply a mechanism by which TFP sensitizes glioblastoma cells to SFB treatment with enhanced intracellular accumulation and efficacy. *PRKCZ* gene encodes for protein kinase C (PKC) zeta, an atypical member of PKC family involved in cell proliferation and survival, and its targeting has been reported to have disruptive impact on the oncogenic signaling cascades in glioblastoma through EGFR and the proinflammatory cytokine tumour necrosis factor-alpha (TNFα) pathways (Kusne et al., 2014).

5.1.2 Sorafenib Modulates Essential Genes Involved in ER Stress, Autophagy, and Apoptosis

SFB alone at 2.5 μM was seen to modulate certain essential genes that imply an anti-tumour efficacy as well as an adaptive response to the kinase inhibition stress on U87-MG cells (Figure 4.2). Acetylcholinesterase (AChE), besides its canonical synaptic role by hydrolysing acetylcholine (Ach) and modulating cholinergic signaling, was shown in different cancer types to play role in driving apoptotic pathways by caspase-3 activation, and influencing drug resistance mechanisms (Richbart et al., 2021). Sorafenib induced *ACHE* upregulation in U87-

MG cells implies accelerated Ach breakdown thus reduced Ach driven pro-growth signaling, which had potentially sensitized the cells to apoptosis. N-ethylmaleimide-sensitive factor (NSF) is an ATPase known to be involved in SNARE complex disassembly required for subsequent autophagosome-lysosome fusion cycles for autophagy (Vivona et al., 2013). Sorafenib was previously shown to induce autophagy in U87-MG cells by LC3 II accumulation and p62 degradation, therefore the upregulation of NSF potentially reflects a compensatory induction of SNARE complex disassembly for cells' autophagic demands (Siegelin et al., 2010). Elongation Factor RNA Polymerase II-Like 3 (ELL3) is known to be an embryonic stem cell (ESC) gene activator as a critical component of the Super Elongation Complex (SEC) and also to be enriched in testis with a p53 negative regulatory role for cell proliferation (Lin et al., 2013; Miller et al., 2000). In addition, it was shown in MCF-7 breast cancer cells to induce MEK/ERK signaling that increased proliferation and cancer stem-like cell population as well as promoted resistance to 5-fluorouracil induced disruption of DNA replication and repair systems (Ahn et al., 2013). Although less is known for ELL3 function in astrocytes, its upregulation in U87-MG cells could reflect an adaptive response to drive transcriptional programs for DNA repair and cell survival against SFB induced cytotoxicity. Heterogeneous Nuclear Ribonucleoprotein A1 Like 2 (HNRNPA1L2) is a critical member of the hnRNP A/B subfamily which is involved in pre-mRNA splicing, packaging, and export, and was shown to be amplifying pro-tumorigenic transcriptional programs through different steps of mRNA maturation in cancers including lung, colorectal and breast (Lu et al., 2022). Sorafenib was shown to be inhibiting RAF/MEK/ERK signaling as well as inducing ER stress over the eIF2α–ATF4 axis in hepatocellular carcinoma cells (Adjibade et al., 2015; Liu et al., 2006). *HNRNPA1L2* downregulation in U87-MG cells could therefore reflect an ERK-dependent suppression of pro-apoptotic splice variants or an ATF4-dependent induction of genes that activate the adaptive pathway of integrated stress response (ISR) that potentially leads to cell

death signals in the long run (Pakos-Zebrucka et al., 2016; Rutkowski et al., 2006). Interestingly, *FDX2*, *HES1*, and *ITPK1* levels were modulated in a similar trend by the single treatments of both TFP and SFB. Ferredoxin 2 (FDX2) is a critical electron donor for mitochondrial iron-sulphur cluster biogenesis that supports respiratory capacity and was shown to induce senescence, lipid peroxidation and ferroptosis upon its loss in ovarian cancer cells (Alhajala et al., 2020; Miyahara et al., 2024). Therefore, its upregulation in U87-MG cells would be expected to facilitate their metabolic stress adaptation for survival. Hairy and Enhancer of Split 1 (HES1) is a transcription factor associated with the activation of Notch signaling that promotes GBM cell proliferation and malignant progression, where its upregulation could as well be reflecting an adaptive response to therapeutic stress in the viable cells (Fan et al., 2006; S. Wang et al., 2024). Inositol-tetrakisphosphate 1-kinase (ITPK1) is a critical enzyme involved in the metabolism of inositol phosphates (IPs), phosphorylating inositol-1,3,4-trisphosphate (Ins(1,3,4)P3) and inositol-3,4,5,6- tetrakisphosphate (IP4) for their conversion into inositol-1,3,4,5,6-pentakisphosphate (IP5) and subsequently inositol hexakisphosphate (IP6) (Ng et al., 2025). Its direct regulatory role in the production of IP6, which has been reported to be involved in critical biological processes including DNA repair, RNA editing, necroptosis, and energy metabolism suggests a potentially disruptive impact of its downregulation on genomic stability and cancer cell survival (Chatree et al., 2020; Dovey et al., 2018; Kalam Shamsuddin & Bose, 2012).

5.1.3 Sorafenib in Combination with Trifluoperazine Enhances Upregulation of Essential Lipid-Biosynthetic and Mevalonate Pathway Genes

The combinatorial treatment of TFP + SFB was seen to be enhancing the upregulation of certain TFP induced genes as *FASN*, *HMGCS1*, *RNF145*, *MVD* (Figure 4.2) Fatty acid synthase (FASN), which is a key enzyme for *de novo* lipogenesis, was shown to be associated with GBM tumour growth and invasiveness (Yasumoto et al., 2016). Its upregulation in U87-MG cells therefore imply increased *de novo* lipogenesis that occurs at a higher rate in glioblastoma stem cells (GSCs) than in differentiated cells and indicates a shift to metabolic reprogramming in cancer cells for enhanced membrane biogenesis, lipidations, energy expenditure, and proliferation under drug induced stress (Ricklefs et al., 2020). Further increased upregulation upon TFP + SFB combinatorial treatment could likely be driven by TFP that had rendered the viability of cells more vulnerable to sorafenib's multi-kinase inhibition that induces ER stress. The mevalonate pathway is a metabolic route for the synthesis of isoprenoids, as cholesterol, from acetyl CoA, and was shown to be enhanced in GBM cells exposed to radiation and pharmaceuticals as dopamine receptor antagonists (He et al., 2024; Miziorko, 2011). Mitochondrial 3-hydroxy-3methygluaryl-CoA synthase (HMGCS1) is the initial player of the mevalonate pathway thus increases *de novo* cholesterol synthesis, and was shown to have supressed expression levels in GBM patient samples (Guo et al., 2022; Villa et al., 2016). Since glial cells have principal role in cholesterol biosynthesis in the brain, upregulation of *HMGCS1* by TFP in combination with SFB in U87-MG shows a tight regulatory response for increased need of cholesterol used in membrane formation, glucose transport, inflammatory signaling, and therapy resistance (Qian et al., 2022). Ring finger protein 145 (RNF145) is an E3 ubiquitin ligase residing in the ER and responsible for the turnover of HMG-CoA reductase, the rate limiting enzyme in the mevalonate pathway, at an accelerated rate upon cholesterol depletion (Menzies et al., 2018). Moreover, mevalonate

diphosphate decarboxylase (MVD) is a critical enzyme in the final step of the mevalonate pathway that converts mevalonate-5-disphosphate into isopentenyl diphosphate as building blocks of cholesterol (Miziorko, 2011). Altogether, their upregulation upon combinatorial treatment is supportive of metabolic reprogramming in U87-MG cells with increased demand for cholesterol biosynthesis.

5.1.4 Trifluoperazine Alone Modulates Signaling Networks Associated with Reduced Plasticity and Proliferative Adaptation

The overall effects of TFP treatment alone aligned well with the literature, primarily suggesting reduced plasticity and invasiveness in a proliferative state (Figure 4.3) (De Silva et al., 2025). Upregulation of genes involved in cholesterol homeostasis was an expected consequence of calmodulin blockade by TFP for the maintenance of membrane integrity and steroid signaling (Bkaily et al., 1984). Significant enrichment of mTORC1 signaling was supportive of essential amino acid transporter upregulations and suggested a metabolic adaptation for cell growth together with the significant enrichment of genes involved in oxidative phosphorylation (Panwar et al., 2023; Saxton & Sabatini, 2017). Upregulation of genes involved in UV response associated with G2/M checkpoint together with E2F targets implied enhanced cell cycle progression against G0/G1 arrest observed in other cancer types upon TFP treatment (Feng et al., 2018; Filipovich et al., 2025; Xia et al., 2019). Although GBM cells do not encounter canonical estrogen response, upregulation of late acting genes overlaps with the induction of pro-proliferative networks as E2F and MYC signaling (Alles et al., 2009; Lan et al., 2017; Miller et al., 2011; Wan et al., 2018). Simultaneous downregulation of genes involved in KRAS signaling implies that the activations serve as compensatory mechanisms for disrupted PI3K/Akt signaling (Martini et al., 2014). A switch to a non-invasive phenotype

was interpreted from negatively enriched EMT, interferon alpha and gamma pathways, and STAT-bearing immune pathways that indicated reduced growth cytokine signaling and stemness phenotype (Fu et al., 2023; Lee et al., 2014). Upregulation of myogenic signature genes also supported a phenotypic transition without the adoption of invasive EMT traits (Kim et al., 2021).

5.1.5 Sorafenib Alone Induces p53 Pathway and KRAS Signaling Components

SFB treatment alone in U87-MG cells was seen to induce an overall response to mitotic stress and to suppress invasiveness as expected (Carra et al., 2013). The upregulation of genes involved in the p53 pathway together with activated G2/M checkpoint, E2F targets and repressed UV response implied significant cell cycle dysregulation and growth inhibition (Collin et al., 2018). The significant upregulation of KRAS signaling components seen with the repression of mTORC1 signaling components likely reflects a compensatory survival pathway against AMPK activation, supportive of the upregulated essential genes by SFB (Figures 4.2-3) (Gulhati et al., 2012). Upregulation of genes involved in oxidative phosphorylation and downregulation of those in metabolic processes of glycolysis, cholesterol homeostasis, adipogenesis, and heme metabolism supported reverse Warburg effect with increased need of mitochondrial respiration, which aligned well with the impact of sorafenib in inducing metabolic stress response and reducing cell proliferation (Cortes Ballen et al., 2024). Downregulation of genes involved in coagulation, angiogenesis, and hypoxia was an expected consequence of VEGFR and PDGFRβ inhibition by sorafenib, supporting the reduced proliferative state of U87-MG cells (Liu et al., 2022). Downregulation of genes involved in protein secretion and unfolded protein response was also expected due to SFB induced ER stress (Lorenz et al., 2021; Simbilyabo et al., 2024). Downregulation of genes involved in EMT

together with those involved in myogenesis, unlike upon TFP treatment alone, suggested reduced cell motility with reduced capacity of cellular reprogramming (Lee et al., 2014). Downregulation of genes associated with immune suppression by single treatments of both TFP and SFB could be interpreted for their combinatorial treatment to have additively reductive impact on invasiveness (Bhat et al., 2020). Activations of distinct and contrasting compensatory mechanisms for survival and against metabolic stress by TFP and SFB would imply U87-MG cells to have a potential of gaining partial chemoresistance under single treatments, but to be more vulnerable to co-targeted pathways under their combinatorial treatment.

5.1.6 Combined Trifluoperazine and Sorafenib Treatment Modulates Gene Expressions Associated with Growth Arrest, Senescence Entry, and Metabolic Reprogramming

TFP + SFB in combination were seen to induce overall effects against cancer cell proliferation and aggressiveness that supported its synergistically inhibitory effect on U87-MG cell viability (Güneş Tok, MSc Thesis). The upregulation of p53 signaling components and the downregulation of MYC target genes together with repressed inflammatory response reflected growth arrest with enhanced tumour suppressive signaling and reduced proliferative drive, which could have potentially suggested TFP + SFB as a promising combinatorial treatment (Porter et al., 2017; Trejo-Solís et al., 2024). In addition, the upregulation of KRAS signaling as an escape mechanism by SFB treatment alone, yet its downregulation by SFB in combination with TFP reflected a potential cell cycle arrest state that was not as significantly entered upon single treatment (Gawi Ermi & Sarkar, 2024). *TP53* and *CDKN1A* (p21) were seen to be further upregulated and *CDK4* was seen to be further downregulated significantly upon combinatorial treatment compared to SFB treatment alone, strongly supporting an entry to partial cell senescence (Appendix Figure 4) (B. Wang et al., 2022; Wei et al., 2015). However, although it

would initially halt tumour growth, prolonged maintenance of a senescent phenotype could lead to drug resistance that would potentially risk cancer cells to transform into a drug tolerant phenotype in the long run (L. Wang et al., 2022). Upregulation of genes involved in myogenesis, TNFα signaling via NFkB, estrogen and androgen response, mTORC1 signaling and metabolic pathways suggested an attempt for cellular reprogramming that was insufficient for maintaining cell survival rate (Achinger-Kawecka et al., 2020; Battistelli et al., 2022; Panopoulos et al., 2012; Soria-Valles et al., 2015). Further functional annotations for the impact of TFP + SFB treatment that associated with stress adaptation and metabolic rewiring were obtained from Gene Ontology gene set enrichment results (Figure 4.4). Downregulation of the RNA splicing machinery supported shutdowns of gene expression programs, typically seen in senescence and apoptosis (Deschenes & Chabot, 2017; Schwerk & Schulze-Osthoff, 2005). Downregulation of genes involved in regulation of small GTPase-mediated signaling supported the repression of KRAS signaling gene expressions and reduced proliferative state (Baltanás et al., 2023; Hillig et al., 2019). Downregulation of genes involved in response to oxygen levels, ECM structure, and keratinocyte differentiation supported reduced invasiveness and increased plasticity (Abou Khouzam et al., 2023; Leduc & Etienne-Manneville, 2015; Winkler et al., 2020). Lastly, upregulation of genes involved in steroid biosynthetic and small molecule biosynthetic processes, protein kinase B (Akt) signaling, fatty acid, ceramide, alcohol and ROS metabolic processes, and abnormal circulating lipid concentration and lipid localization suggested a profound metabolic rewiring toward stress adaptive lipid and redox homeostasis, strongly supporting a compensatory survival response for maintaining membrane integrity and oxidative balance under cytotoxic pressure (Koundouros & Poulogiannis, 2020; Masci et al., 2024). However, their activation together with the upregulation of DNA replication genes and mitotic stress signatures, as well as with the observed HRAS inducing effect of TFP, could suggest mitotic catastrophe followed by autophagy-dependent or -associated cell death

(Sazonova et al., 2021). Altogether, although the protein levels and activity statuses should be further investigated, these enriched gene sets reflect a complex cellular response marked by growth arrest, reduced invasiveness, and metabolic stress, highlighting the potential of TFP + SFB combinatorial treatment to synergistically suppress tumorigenic traits in U87-MG cells while exposing key vulnerabilities in survival pathways that could be exploited for the combination of TFP with other target kinase inhibitions.

5.1.7 Sorafenib Modulates Gene Expressions Associated with p53-Driven Growth Arrest and Suppressed Invasiveness in Combinatorial Treatment

Sorafenib, as a multi-kinase inhibitor, simultaneously blocks key drivers of proliferation and angiogenesis, by inhibiting RAF kinases that then block the MEK/ERK pathway and lead to G1 arrest, by inhibiting VEGFR and PDGFRβ that then reduce vasculature density and stability, and by inhibiting c-KIT, FLT3, FGFR1 that then disrupt PI3K/Akt signaling (Colardo et al., 2021; Fan et al., 2024; D. Li et al., 2020; Wilhelm et al., 2008). Therefore, the top enriched terms of EMT, hypoxia response, coagulation, protein secretion pathways, and UV response, which were observed to be similarly and significantly repressed, validated the expected capacity of sorafenib to restrict invasion, resilience, and survival pathways with significant cytotoxic pressure (Figure 4.5). Although the anti-cancer efficacy of SFB in combination with TFP was previously shown in Hep3B hepatoma cells that have epithelial phenotype, are p53-null, and have low PTEN expression, the driving mechanisms would be expected to differ in U87-MG cells that are of astrocytic origin with mesenchymal-like phenotype, have wild-type p53, and are PTEN-null (Murat Yaman, PhD Thesis) (Augello et al., 2016; Schulz et al., 2022). When the log2 fold-changes from RNA-seq were evaluated by regression analysis for Hep3B hepatoma cells, which have a doubling time of about 28

hours, treated with 12 μM trifluoperazine combined with 2 μM sorafenib for 48 hours and for U87-MG glioblastoma cells, which have a doubling time of about 39 hours, treated with 10 μM trifluoperazine combined with 2.5 μM sorafenib for 72 hours, the resulting regression models produced near-zero coefficients of determination and minimal slopes. Even for the subset of genes significantly modulated in both cell lines, the regression slope and r-squared value remained low at only 0.16 and 0.02 respectively, highlighting that the same combination in parallel treatment duration and doses engaged largely distinct transcriptional profiles in these two cancer models (Appendix Figure 1). U87-MG cells are likely to engage in p53-driven p21 induction for growth arrest on top of ER stress and autophagy overload upon sorafenib treatment, as well as higher activation of Akt signaling due to PTEN loss (Datta et al., 2002; Georgescu, 2010; He et al., 2021). Significant negative enrichment of E2F targets and G2M checkpoint genes showed that although they were seen to be positively enriched upon TFP + SFB treatment compared to DMSO control, they were not activated as much as upon TFP treatment alone, suggesting reduced ability for compensatory cell cycle progression (Benary et al., 2020). The significant negative enrichment of MYC targets, which were seen to be activated by TFP treatment alone while being majorly repressed by the combinatorial treatment, further implied a profound cell cycle blockade induced by SFB (García-Gutiérrez et al., 2019). However, E2F and MYC targets were seen to be majorly influenced by TFP treatment, as TFP + SFB were clustered the closest with TFP treated sample in their corresponding heatmaps (Appendix Figure 2). In addition, cholesterol biosynthesis pathways were seen to be upregulated upon TFP alone and further positively enriched upon combinatorial treatment, reflecting a mechanism to reinforce membrane integrity against increased drug induced stress (Figure 4.5, Appendix Figure 3) (Mok & Lee, 2020). Positive enrichment of TGFβ signaling when the TFP + SFB group was compared to the single TFP treated group also suggested cytokine response for survival mechanisms as it was linked to adaptive therapy resistance in

GBM while transiently enhancing cell cycle arrest (David & Massagué, 2018; Golán-Cancela & Caja, 2024).

The detailed investigation of significantly modulated genes within the top two enriched hypoxia and EMT pathways provided further insight into how sorafenib driven transcriptional changes are modulated by trifluoperazine in glioblastoma cells (Figure 4.6). Consistent with previous observations of sorafenib's capacity to impair hypoxia related adaptation mechanisms, the majority of hypoxia associated genes were downregulated upon sorafenib treatment alone, aligning well with its known suppression of HIF-1α stabilization and downstream glycolytic signaling (Méndez-Blanco et al., 2018). Critical hypoxia-responsive genes that have established roles in metabolic adaptation and cellular survival under hypoxic conditions were seen to undergo even greater downregulation when sorafenib was combined with trifluoperazine (Qannita et al., 2024). Most strikingly, the pyruvate dehydrogenase kinase 1 gene PDK1 and the lactate dehydrogenase gene LDHA, which redirect pyruvate from the TCA cycle and promote lactate production, were further attenuated by the addition of trifluoperazine (Shaikat et al., 2025). Likewise, SLC2A1 (GLUT1), central to HIF-mediated glycolysis, displayed marked reduction under combinatorial therapy, indicating a collapse of hypoxic adaptation pathways (Jiang et al., 2018). These suggested that trifluoperazine amplifies sorafenib's inhibitory effect on metabolic flexibility essential for glioblastoma cell survival under hypoxic stress (Méndez-Blanco et al., 2018). However, the combinatorial treatment also induced compensatory responses in a subset of hypoxia associated genes whose expression levels were partially restored compared to single sorafenib treatment. This likely suggested a cellular feedback mechanism attempting to counteract the severe metabolic disruption and sustain limited survival signaling, potentially through the observed modulation of transcription factors such as FOXO3 and KLF6 that can activate stress response pathways or alternative survival mechanisms under therapeutic pressure (Bakker et al., 2007; Huang et al., 2008). In

the context of EMT signaling, sorafenib-alone significantly increased the expression of several genes implicated in promoting invasive and mesenchymal traits in glioblastoma cells, and combinatorial treatment with trifluoperazine was seen to revert this effect, either by significantly downregulating them or partially reducing their expression. Specifically, Integrin α2 (ITGA2), previously shown to be overexpressed in high-grade gliomas and linked to enhanced cell migration, invasion, stemness, and resistance via AKT signaling pathways, emerged as a potential driver of glioma cell invasiveness (L. Wang et al., 2024; Zhang et al., 2024). Similarly, although Frizzled 8 (FZD8) is less studied in gliomas, its overexpression in various cancers was associated with enhanced proliferation, invasiveness, and poor prognosis (Yang et al., 2017). Furthermore, NT5E (CD73), known to be significantly upregulated in glioblastoma, contributes to tumour invasion, angiogenesis, and immune suppression through adenosine production (Wang et al., 2021). Elevated NT5E levels have been correlated with poor survival outcomes in GBM patients, highlighting its critical role in tumour progression and aggressiveness (Wang & Matosevic, 2019). Conversely, the combination treatment upregulated a set of genes that were downregulated by sorafenib alone, possibly indicating a partial reversion of mesenchymal phenotype. Notably, SCG2 which has been demonstrated as a prognostic marker associated with immune modulation and angiogenesis, was seen to be in this cluster (H. Wang et al., 2022). Studies in different cancer models have suggested that SCG2 can exhibit context dependent roles, where its overexpression inhibits tumour growth by disrupting angiogenesis, indicating its potential as an alternative signaling mediator upon combinatorial treatment (Fang et al., 2021). Another cluster of genes was further downregulated by the combinatorial treatment, suggesting an enhanced suppression of mesenchymal characteristics and ECM remodelling. Specifically, COL1A1, which has been recognized as an invasion related gene in glioma enriched in extracellular matrix remodelling and linked with glioblastoma cell invasion with poor clinical outcomes, as well as Vimentin

(VIM), the canonical mesenchymal marker that has been strongly associated with increased invasiveness, stemness, and poorer prognosis in glioblastoma models, were observer to be in this cluster (Doroszko et al., 2025; Ren et al., 2022; Sun et al., 2018; Zottel et al., 2023). Overall, these gene level observations supported that trifluoperazine amplifies the inhibitory effects of sorafenib on hypoxia and EMT associated signaling, enhancing its therapeutic potential by targeting the adaptive flexibility of glioblastoma cells. However, the activation of the abovementioned gene cluster implies possible escape routes that could limit long term efficacy, highlighting the need for further mechanistic investigation to enhance therapeutic strategies combining trifluoperazine with kinase inhibitors for glioblastoma treatment.

5.1.8 Trifluoperazine Suppresses Calcium-Calmodulin Dependent Signaling While Sorafenib Upregulates PLC, ADCY, and PKC in Combinatorial Treatment

Trifluoperazine's primary mode of action as a calmodulin (CaM) antagonist led to the examination of its impact on the calcium signaling cascade, a pathway known to regulate migration and invasiveness in GBM cells (So et al., 2021). By overlaying log2 fold-change values from RNA-seq onto the KEGG calcium signaling map, it was observed that TFP alone substantially downregulated key upstream receptors and effectors, most notably the inositol 1,4,5-trisphosphate receptor (IP3R) and CaM-dependent kinases such as MLCK, CAMK family members, NC6, and PKC isoforms, consistent with disrupted calcium-CaM signaling (Figure 4.7). Inhibition of myosin light-chain kinase (MLCK) in glioblastoma cells has been shown to impair actomyosin contractility and reduce invasive behaviour by suppression of extracellular matrix remodelling (Cheng et al., 2018). Similarly, reduced expression or pharmacological inhibition of calcium/calmodulin-dependent protein kinase II (CaMKII) isoforms has been shown to diminish glioblastoma stem-like cell viability and sphere-forming

capacity (Ronnen et al., 2024). In parallel, downregulation of the sodium–calcium exchanger (NCX) in GBM cells has been shown to disrupt calcium homeostasis, triggering calcium dependent cell cycle arrest and apoptosis without affecting healthy astrocytes (Hu et al., 2019). Finally, suppression of specific PKC isoforms, most notably PKCδ, has been shown to significantly decrease migration and invasion of U87 and patient-derived GBM cells (Hwang et al., 2015). Therefore, this broad suppression likely contributes to reduced cytoskeletal contractility and cell motility, as well as impaired activation of downstream proliferative signals. Interestingly, when TFP was combined with sorafenib, several nodes including PLCγ, PLCε, adenylate cyclase (ADCY), and PKC showed relative upregulation, suggesting a compensatory feedback response to sustained CaM inhibition. PLCγ (PLCG1) overexpression has been directly linked to enhanced proliferation and poor prognosis in glioma, with PLCG1 knockdown reducing tumour cell growth and sensitizing GBM models to targeted therapies (Li et al., 2022; Walker et al., 2018). In contrast, PLCε (PLCE1) has been shown to support glioma stem cell survival and self-renewal via the JNK axis, and its silencing has been shown to impair tumour initiation *in vivo* (Okada et al., 2022). Similarly, adenylate cyclase 5 (ADCY5) functions as a tumour suppressor in GBM, where reduced ADCY5 expression has been shown to correlate with poorer patient outcomes, and its rescue has been shown to attenuate glioblastoma cell viability through cAMP-mediated pathways (Can et al., 2024). Finally, specific PKC isoforms, notably PKCδ, have been shown to promote U87 cell invasion and GBM patient-derived cell survival (Carmo et al., 2013; Hwang et al., 2015). Taken together, upregulation of these calcium signaling components may represent an intrinsic feedback loop to counteract TFP induced CaM blockade, yet under conditions of sustained pathway dysregulation, these changes likely contribute to diminished viability and enhanced sensitivity to sorafenib. Together, these findings highlight calcium signaling dysregulation as a central

mechanism by which trifluoperazine exerts its anticancer efficacy and enhances sorafenib's activity.

5.1.9 Combined Trifluoperazine and Sorafenib Treatment Amplifies Lipid Biosynthetic and Cholesterol Homeostasis Gene Expression

The combination of trifluoperazine and sorafenib elicited an even greater induction of several lipid biosynthetic and cholesterol homeostasis genes compared with trifluoperazine alone, reflecting an intensified metabolic adaptation (Figure 4.8). Among them, MVD and FASN were previously identified as significantly modulated essential genes (Figure 4.2). In addition, ACAT2, responsible for converting free cholesterol into storage esters, has been implicated in tumour progression and may protect cells against excess free cholesterol under dual treatment (Guo et al., 2022). Similarly, elevated FDPS expression can augment prenylation of small GTPases, reinforcing proliferative and survival signaling, while FDFT1 upregulation promotes squalene synthesis and has been shown to sustain glioblastoma stemness through AKT pathway activation (Abate et al., 2017; Mo et al., 2024). The acetate-activating enzyme ACSS2, linked to survival under metabolic stress, was also further induced, indicating an increased reliance on acetate as an alternative carbon source for acetyl-CoA production (Qiu et al., 2021). Notably, induction of the mevalonate pathway and more broadly the cholesterol homeostasis genes are mechanistically linked to suppression of ferroptosis via the FSP1–CoQ10 axis and cholesterol buffering of lipid peroxidation (Hadian & Stockwell, 2020; J. Li et al., 2020). Sorafenib has been shown to provoke ferroptotic stress in several cancer models, most notably HCC, though not uniformly across cell lines (Zheng et al., 2021). Also, TFP has been shown to induce autophagic flux in GBM cells, possibly engaging ferroptosis (Zhang et al., 2017). Indeed, it has been shown to induce ferroptosis by increasing lipid-ROS in oral

squamous carcinoma (Tsai et al., 2024). Thus, an upregulated cholesterol homeostatic signature under TFP + SFB in U87-MG cells implies a counter-ferroptotic program likely by increased lipid-ROS and ferroptotic pressure in the remaining viable cells. An anti-ferroptotic program might be activated upon accumulation of squalene/cholesterol to physically quench lipid radicals, restoring redox balance, by enriched cholesterol homeostasis despite the reduced overall cell viability upon the combinatorial treatment (Hadian, 2020; Sun et al., 2023).

Within the mTORC1 signaling module, enhanced DHCR24 expression may protect cells from oxidative damage by reinforcing membrane raft integrity, and higher G6PD levels will generate additional NADPH for reductive biosynthesis and antioxidant defence, a feature known to promote GBM cell survival and resistance (Mashimo et al., 2014). Collectively, this further upregulation across both cholesterol biosynthesis and mTORC1 pathways underscores a robust compensatory metabolic reprogramming in U87-MG cells that may help resist CaM antagonism and kinase inhibition, while also revealing vulnerabilities in lipid metabolism for future therapeutic targeting.

5.2 Trifluoperazine Exhibits a Favourable Early Larval Safety Profile, While Sorafenib Induces Severe Developmental Toxicity

Trifluoperazine, administered at concentrations up to 20 μM between 2 and 5 dpf, produced no observable morphological abnormalities or developmental defects, indicating a favourable safety profile in early development (Figure 4.9). In contrast, sorafenib treatment at 2.5 μM over the same window consistently induced severe cardiac edema, pronounced yolk-sac enlargement, and partial to complete tissue necrosis, reflecting its well-documented cardiotoxic and embryotoxic liabilities in zebrafish models (Figure 4.10) (R. Li et al., 2020). Previous studies have similarly reported that 2-3 μM sorafenib exposures in zebrafish embryos and

larvae induce pericardial edema, yolk-sac swelling, cardiac dilation, and impaired organogenesis, establishing a reproducible developmental toxicity profile (Cheng et al., 2011; Chimote et al., 2014; Kawabata et al., 2015). This toxicity profile likely stems from sorafenib's multi-kinase inhibition, which disrupts critical angiogenic and cell-survival pathways during organogenesis. Although the combinatorial treatment with the *in vitro* dose of 10 µM TFP used in this study was not observed to enhance the severity of 2.5 µM sorafenib induced phenotype, it raised valid concerns about off-target toxicity that compromise tolerability. A 48-hour 12 µM TFP and 2 µM sorafenib combinatorial treatment had also been previously explored in 4 dpf zebrafish larvae and observed to induce cardiac edema, but without yolk sac swelling (Büşra Korkmaz, MSc Thesis). This prompted the search for alternative kinase inhibitors that might demonstrate synergistic anticancer activity without developmental toxicity in zebrafish. In a clinical context, rigorous *in vivo* safety profiling in mammalian models would be essential to ensure a favourable balance between efficacy and potential side effects on healthy tissues.

5.3 High-Throughput Viability Screening in U87-MG and A172 Cells Identifies Low-Dose Kinase Inhibitors with Potent Growth-Inhibitory Activity

Potent kinase inhibitors identified by drug panel screening in U87-MG and A172 cells align with established vulnerabilities in GBM signaling networks (Figures 4.11-12, Table 4.1). These cell lines are widely used and well-characterized, yet an important limitation is that both are EGFR wild-type, whereas EGFR amplification and activating mutations such as the EGFRvIII variant are among the most frequent alterations in glioblastoma, present in approximately 40–50% of patient tumours, driving constitutive oncogenic signalling (Pearson & Regad, 2017; Rodriguez et al., 2023). Thus, while U87-MG and A172 provide a robust foundation for high-throughput screening, the efficacy of multi-kinase inhibitors like sorafenib

may be influenced by their EGFR status. Given that both U87-MG and A172 lines are PTEN-null, resulting in hyperactivation of the PI3K/AKT/mTOR axis, it is particularly insightful that multiple PI3Kα and/or mTOR inhibitors demonstrated high potency at low micromolar concentrations, highlighting the pathway's therapeutic tractability in these GBM models (Singh et al., 2023). The PI3Kα inhibitor PIK-75 has been shown to drive apoptosis via robust PI3K/Akt suppression in U87-MG and LN229 cells, yet it hasn't been studied further due to its limited in vivo stability (Cheng et al., 2012). Although CAY10626 has not been used in preclinical studies on GBM therapy, dual PI3Kα/mTOR inhibition by other strategies has been demonstrated to halt glioma growth by inducing G1 cell cycle arrest, apoptosis, and radiosensitization (Gil del Alcazar et al., 2014; Shi et al., 2017). Moreover, blockade of mTOR signaling by Torin1 has been shown to consistently inhibit glioblastoma cell proliferation, migration, and S-phase entry while reducing S6K and 4E-BP1 phosphorylation (Amin et al., 2021). Dual inhibition of mTORC1 and mTORC2 by INK128 has also been shown to exhibit potent antiproliferative effects on GBM cells, and has advanced into phase 2 clinical trials, demonstrating its translational promise (Singh et al., 2023). Furthermore, the screen uncovered additional kinase vulnerabilities, spanning PKC, PKD, Syk, DNA damage response and translational regulators, highlighting diverse signaling dependencies in glioblastoma for the search of synergistic combinations. It has been shown that the PKC inhibitor staurosporine induces complete growth arrest in human glioma cell lines accompanied by downregulation of CDK2, CDC2, Cyclin A/B and upregulation of p21, highlighting its broad anti-mitotic effects in gliomas (Baltuch et al., 1993; Harmalkar & Shirsat, 2006). PKC inhibition by bisindolylmaleimide IX has been shown to potentiate TNF-mediated apoptosis by disrupting survival signaling in prostate cancer cells, although it has not been studied for gliomas (Rokhlin et al., 2002). Targeting protein kinase D with CRT0066101 has been shown to induce G2/M arrest across solid tumours (Harikumar et al., 2010). Syk inhibition by R406 has been shown

to shift glioma stem cells from a glycolytic to an oxidative phenotype, enhancing temozolomide sensitivity *in vivo* (Sun et al., 2019). Checkpoint kinase inhibition via AZD7762 has been shown to radiosensitize GBM models, validating DNA damage response targeting strategies in glioma therapy (Ferri et al., 2020). However, although AZD7762 had reached Phase I clinical trials, it has been shown to induce to cardiotoxicity issues (Tang et al., 2012). Modulators of translational control such as the eEF2K/CAMKIII inhibitor NH125 has been shown to disrupt elongation factor-mediated pathways to impair cancer cell growth (Chen et al., 2011). PLK1 blockade by volasertib has been shown to disrupt YBX1 phosphorylation and nuclear localization, precipitating DNA damage and apoptotic signaling, thereby combining mitotic inhibition with transcriptional dysregulation to enhance antitumor efficacy in GBM models (Dong et al., 2018; Li et al., 2023). Finally, BMS-345541, which induces NF-kB dysregulation through IKK inhibition, has been shown to sharply diminish glioma cell proliferation and inflammatory cytokine production (Du et al., 2012). Collectively, while many of these kinase inhibitors have undergone preclinical or clinical evaluation in various glioma contexts, the IC50 values determined here for U87-MG and A172 cells established a quantitative baseline for subsequent studies, particularly for their repurposing in combination with trifluoperazine. Although deriving IC50 values from only three concentration points offers limited precision and would benefit from a broader dose range, this first-pass screen provided valuable insight into relative potencies of diverse and clinically compelling candidates for glioblastoma treatment.

5.4 Trifluoperazine Synergizes with Diverse Kinase Inhibitors in U87-MG Cells

Combinatorial treatment with TFP showed promise in sensitizing glioblastoma cells to various kinase inhibitors, highlighting their repurposing potential. When U87-MG cells were

exposed to 2.5 μM of each kinase inhibitor with 10 μM TFP, 5 compounds were identified to be inducing significantly higher viability loss compared to single treatments, despite TFP alone slightly enhancing cell growth (Figure 4.13, Table 4.2). The use of a 2.5 μM concentration for each kinase inhibitor aimed a low-dose threshold that minimizes off-target toxicity while remaining within pharmacologically relevant ranges for preclinical GBM models. Notably, the PLK1 inhibitor volasertib and the dual mTORC1/2 inhibitor INK128, which were also among potent low dose inhibitors, exhibited the strongest synergy, achieving over 80% growth inhibition and ZIP scores of 35.6 and 14.1, respectively (Figure 4.14). Three additional agents, Syk Inhibitor II, the ALK/ROS1 inhibitor lorlatinib, and the Cdc7/CDK9 inhibitor PHA-767491, showed limited single agent efficacy with IC50 values greater than 10 μM but markedly suppressed viability to 88%, 79%, and 36% when combined with TFP. While all 5 synergistic agents could be explored further in combination with TFP, volasertib and INK128 exhibited the most robust synergy and have relatively established clinical profiles, which had prioritized them for follow-up toxicity tests.

5.5 Trifluoperazine Causes Reversal of Growth Inhibition Efficacy of Diverse Kinase Inhibitors in U87-MG Cells

While TFP synergized with certain kinase inhibitors, it paradoxically antagonized several others whose activation or localization likely relies on TFP's multifaceted actions including calmodulin dependent PKC inhibition, and P-glycoprotein blockade (Figure 4.15). The DNA-PK inhibitor NU7026 significantly reduced cell viability alone but was ineffective when combined with TFP. Since DNA-PK is regulated by CaMKK-mediated calcium-calmodulin signaling and by PKA downstream of D2R activity, TFP’s disruption of these inputs might have preserved DNA-PK function and negate NU7026’s effect (Amatya et al., 2012).

The growth inhibitory effects of the Src inhibitors, PP2 and SU6656, were also abrogated by TFP. Since calmodulin directly activates c-Src and regulates its membrane localization, TFP's CaM antagonism might have prevented the access to this drug target (Stateva et al., 2015). Significant reduction of cell viability by the PI3Kγ inhibitor AS-041164 was also reversed by TFP. Since PI3Kγ activation critically depends on CaM binding to its p101/p87 regulatory subunits and on Gβγ-mediated membrane recruitment, altered membrane lipid dynamics might have blocked the engagement of the inhibitor (Vandonselaar et al., 1994). VEGFR/PDGFR inhibition by the clinical drugs ABT-869 and vatalanib might as well rendered ineffective with TFP due to the blockade of engagement with their targets since VEGFR2 dimerization, autophosphorylation, and plasma-membrane retention was shown to be regulated by calmodulin interactions (Tilak et al., 2021).

Moreover, the Cdc7/CDK9 inhibitor PHA-767491 and ROCK1/2 inhibitor CAY10622 not only lost efficacy but paradoxically enhanced proliferation when combined with TFP, possibly reflecting feedback activation of survival pathways. Likewise, the LRRK2 inhibitor GNE-7915 might have lost its inhibitory effect in combination with TFP, due to LRRK2's requirement for CaM binding to achieve proper conformation and subcellular targeting that has been defined in neuronal systems (O'Day, 2022). Additionally, TFP's inhibition of P-glycoprotein efflux may alter intracellular concentrations of co-administered kinase inhibitors, further contributing to antagonistic interaction (Silva et al., 2015; Zhang et al., 2017). Collectively, these data reveal that TFP's interference with membrane-associated, CaM, PKC, and D2R-dependent kinase activation can reverse the growth inhibitory effects of specific inhibitors. Effective combination strategies should therefore focus on kinases whose function is independent of these TFP targeted pathways.

5.6 Volasertib Treated U87-MG Gene Signature Associates with Improved Clinical Prognosis in GBM

Volasertib's ability to induce pronounced mitotic arrest in U87-MG cells, evidenced by cell rounding and density reduction at a low dosage of 2.5 μM, mirrors its established role as a PLK1 inhibitor that disrupts spindle dynamics and triggers apoptosis in glioma models (Figure 4.16) (Dong et al., 2018). Besides its synergy with TFP, volasertib's cytotoxic profile highlights its promise for further experimentation both as a single agent and in combination. The ability of the volasertib gene signature to distinguish TCGA-GBM patient survival, where high composite scored patients were seen to have significantly longer overall survival, further elevates its translational potential (Figure 4.17). Unlike the gene set modulated by sorafenib in U87-MG cells, those modulated by volasertib captured tumour vulnerabilities that correlate with improved clinical outcomes, suggesting its effects extend beyond in vitro cytotoxicity (The Cancer Genome Atlas Research Network, Nature 2008). In addition, it has been reported that GBM patients with low PLK1 expression exhibit significantly improved survival outcomes compared to those with high expression (Li et al., 2023). Importantly, the *in vitro* concentration of 2.5 μM used in this study falls within the range of clinically achievable plasma levels observed in patients, where phase I trials reported peak concentrations of around 3–4.5 μM (Schöffski et al., 2012). This overlap supported the translational relevance of the experimental dose. Taken together, the convergent evidence of potent mitotic disruption, robust synergy with TFP, and a prognostic volasertib gene signature justify further mechanistic studies and in vivo evaluation in larval zebrafish xenograft models to assess the therapeutic potential of the TFP and volasertib combination for glioblastoma.

5.7 Volasertib Exhibits a Favourable Toxicological Safety Profile in Early Zebrafish Larval Development

Effective kinase inhibitors prioritized from cell viability assays were evaluated for developmental toxicity in wild-type AB zebrafish larvae to leverage the proven suitability of this intact vertebrate as an excellent model for preclinical toxicology screening (Tal et al., 2020). Unlike sorafenib, none of the tested compounds at 2.5 μM induced pericardial edema, yolk-sac abnormalities, or other morphological defects from 2 to 5 dpf, indicating high tolerability commencing from hatching period (Figure 4.18). Although volasertib emerged as the highest priority candidate based on its in vitro potency and prognostic signature, the mTOR inhibitor INK128 was also included in the larval assay due to its low dose efficacy, strong synergy with TFP, advanced clinical trajectory. Additionally, the Src inhibitor SU6656 was tested to enable future investigation of the antagonistic interactions observed with TFP, despite its efficacy as a single agent.

Volasertib administered at 2.5 μM in combination with 10 μM TFP also produced no observable developmental or stress related phenotypes (Figure 4.19), further supporting the utility of this repurposed drug combination. When volasertib treated Tg(*gfap*:GFP) larvae were quantified by the log2 based ratio of GFP fluorescence before and after drug exposure to assess effects on glial populations, it was observed that GFP signals relative to DMSO controls were not significantly altered by either 1.25 μM or 2.5 μM concentration (Figure 4.20). The absence of *gfap*:GFP perturbation suggested that volasertib treatment does not drastically impair glial viability or differentiation during early zebrafish development. While this 2D lateral imaging approach offers a rapid, first-pass assessment of large-scale changes in *gfap*:GFP reporter expression, it lacks the spatial resolution and volumetric accuracy required for precise quantification of glial alterations. Future studies should integrate three-dimensional imaging

modalities and GFAP protein level quantifications to validate and refine these initial findings. Enhancing the methodology would strengthen the reliability of in vivo glial toxicity assessments. Taken together, these results confirm the safety of volasertib and TFP in zebrafish larvae, justifying the rationale for further testing the combinatorial treatment on xenograft models.

5.8 R Shiny Based Web Application *LDexplore* Automates Analysis of Larval Locomotion and Startle Response

A custom R Shiny based platform, LDexplore, was developed to enable high throughput, automated analysis of zebrafish larval locomotion under alternating dark:light periods and light induced startle stimuli. This tool streamlined data processing by extracting velocity metrics, generating heatmaps, and performing statistical analyses on deceleration trends of grouped larvae, reducing manual error and facilitating behavioural phenotyping. The utility of this platform was first demonstrated using TFP at gradually increasing concentrations of 0, 5, 10, and 20 µM, which facilitated interpretation of locomotor profiles given TFP's established effects on mood disorders such as reducing symptoms of anxiety and depression (Mendels et al., 1986). Under the *Startle Response Model*, DMSO vehicle treated 5 dpf larvae showed typical behaviour: a baseline velocity in the first 10-minute dark period, reduced swimming in the subsequent 10-minute bright phase and rebound hyperactivity in the second 10-minute dark period, followed by an immediate freeze upon a 30-second light pulse and a pronounced peak in the final dark period (Figure 4.21A). Clustering analysis showed that control group larvae tended to gather in lower activity groups, defining the normal movement scales without drug treatment. 20 µM TFP treated larvae included several highly active ones, suggesting high TFP doses can boost swimming without changing the overall behaviour pattern

and responsivity to light. Although the clusters were intermingled for TFP treated and control group larvae, indicating parallel swimming patterns among these groups, the ability of the application to easily distinguish drastically different behavioural patterns was observed by the clear clustering of the locomotion heatmap for sorafenib versus DMSO vehicle treated larvae (Appendix Figure 8). At 20 μM TFP, larvae exhibited the highest velocity peaks during both the dark:bright and startle light:dark transitions compared to lower doses (0, 5, and 10 μM), validating the applied protocol for detecting dose dependent behavioural changes (Figure 4.21B). TFP's enhancement of larval velocity at higher concentrations only after light stimuli suggests an anxiolytic or dopaminergic modulatory effect, mirroring its clinical use to alleviate anxiety and agitation (Figure 4.21C). Calculating deceleration slopes provided insight into how TFP modulates sensorimotor processing and recovery in zebrafish larvae (Figure 4.22). In *DARK I,* near zero slopes confirmed uniform baseline swimming stability across treatments. The trend toward sharper deceleration in *DARK II*, especially among the 5 μM TFP treated larvae, suggested that moderate TFP doses may heighten sensitivity to the prior *BRIGHT* phase, resulting in increased response to immediate transition into dark. Although not statistically significant, this dose specific effect implies TFP's neuromodulatory impact on the circuits that govern adaptations to light. In particular, TFP's disruption of the cholesterol biosynthesis pathway, previously observed in U87-MG cells, which is especially relevant given the brain's reliance on de novo cholesterol synthesis for synaptic function and membrane integrity, might have influenced a low-grade neurotoxicity and neuronal responsiveness (Mauch et al., 2001). In *FINAL DARK* after startle light stimulus, dose dependent increase in instantaneous responsivity to startle stimulus was observed with 20 μM and 10 μM TFP treated groups eliciting the sharpest deceleration before converging to a baseline velocity. Such gradual slowing likely arises from TFP's combined impact on calcium signaling and dopaminergic circuits, both of which critically regulate startle recovery in larval zebrafish via calcium

mediated neurotransmission and dopamine dependent modulation of motor output (Mu et al., 2012). Together, these findings show that while TFP treatment at relevant doses does not disrupt basal locomotion but selectively enhances deceleration trends following sensory stimuli in a dose dependent manner, highlighting its neuromodulatory effects on habituation and sensorimotor gating.

Experimental batch variability in baseline speeds emphasizes the need for rigorous assay standardization, yet the preservation of deceleration and rebound patterns across same TFP treated groups demonstrates the relative robustness of the analysis platform . The elevated baseline and post stimulus activity of volasertib treated larvae, as well as increased variability in the combined TFP and volasertib treated group, further highlights how combinatorial pharmacodynamics can reshape larval behaviour (Figure 4.23). In addition, the 10 µM TFP and 2.5 µM volasertib combination did not induce significant behavioural consequences as 20 µM TFP or 2.5 µM sorafenib, further prioritizing this drug repurposing strategy (Figure 4.21, Appendix Figure 8). These results not only suggested the pharmacological safety of the drugs on the central nervous system but also highlighted the importance of precise quantification of light induced swimming patterns in behavioural screens. Although the automated platform requires incorporation of additional statistical analyses and experimental protocols for accurate interpretations, it offers a robust starting point for quantifying drug induced locomotor and startle response alterations in 4-6 dpf zebrafish larvae by integrating automated processing of collected data, statistical scoring, and visualization.

The Shiny application is inherently compatible with in-house Zantiks workflows because the exported data structure (e.g., column names, stimulus annotations, arena IDs, sampling rate) is defined by the experimenter in the Zanscript that runs on the Zantiks server. Accordingly, when new or modified protocols are tested, such as with different light–dark

transitions, startle paradigms, acclimation conditions, and time period specifications, differences in output format should be anticipated and the import/analysis steps adjusted via a protocol-specific schema for arena and time bin mapping, metadata, and DARK/BRIGHT stimulus logs (zantiks.com). Moreover, to better illustrate between-group differences and benchmark assay sensitivity, inclusion of a pharmacological positive control such as pentylenetetrazole (PTZ) would be beneficial. PTZ has been shown in multiple studies to reliably induce hyperlocomotion and seizure-like activity in 4-7 dpf larvae and is widely used to validate locomotion and startle readouts in multi-well platforms (Afrikanova et al., 2013; Bartoszek et al., 2023; Peng et al., 2016). Standardized PTZ treatment provides a robust dynamic range against which drug effects can be contrasted, and they integrate well with light–dark and startle protocols (Whyte-Fagundes et al., 2025). Incorporating a PTZ-treated control cohort alongside vehicle controls would therefore aid interpretation of clustering, velocity peaks, and deceleration slopes in the pipeline.

5.9 Brain Orthotopic Xenograft Model Demonstrates Stable U87-GFP Engraftment and Moderately Alters Larval Behaviour

Human U87-GFP cells engrafted into the zebrafish larval brain were observed to survive for at least 3 days post injection without inducing major developmental defects, aligning with prior studies on larval zebrafish in which orthotopic GBM xenografts were described for their efficacy in pharmaceutical testing with conserved blood-brain barrier integrity and overall viability (Figure 4.24A) (Welker et al., 2016; Zeng et al., 2017). Occasional minor injury to adjacent structures, most notably to the eyes, can occur during microinjection, mirroring findings in other zebrafish studies where localized tissue insult altered sensory inputs without compromising survival (Giacich et al., 2025). Such perturbations

highlight the importance of functional assays alongside anatomical validation. Specifically, eye damage in zebrafish larvae has been shown to impair visual processing and modify locomotor patterns in light-dark assays since the visual system drives exploratory and startle behaviours (Portugues & Engert, 2011). Incorporating the *Startle Response Model* locomotion assay thus serves not only to quantify foreign cancer cell induced or vehicle injection related effects on nervous system function but also to detect subtle sensory deficits that may arise from adjacent tissue injury (Figure 4.24B-25). Microinjection into the larval brain may inevitably provoke local tissue injury and systemic inflammation, which in zebrafish has been shown to drive leukocyte invasion, induce pro-inflammatory cytokines, and lead to anxiety-like behaviours characterized by reduced locomotion and thigmotaxis (Chen et al., 2022). Utilizing transgenic zebrafish lines for complementary imaging of cerebral blood vessels and inflammatory markers could therefore be useful to distinguish micromanipulation induced tissue damage from the actual impact of graft-host interactions. Importantly, despite the significant velocity deficits observed in mock injected and xenograft groups, the conservation of deceleration patterns across dark periods implied that core sensorimotor gating and startle habituation remained relatively intact. This resilience, together with the fact that larval maintenance at the suboptimal temperature of 32 °C did not disrupt the characteristic dark:light locomotor profile, validated the robustness of the behavioural assay and supports its continued use to detect subtle phenotypes in orthotopic xenograft studies for in vivo drug screening.

Overall, the successful engraftment of U87-GFP cells and the preservation of key developmental processes confirm the model's utility for evaluating human glioblastoma cell behaviour, drug penetration, and host-tumour interactions *in vivo*. By combining orthotopic GBM cell implantation with sensitive behavioural readouts, this system offers a promising platform for preclinical evaluation of promising candidate drugs, such as the prioritized trifluoperazine and volasertib combination in this preliminary study.

6. FUTURE PERSPECTIVES

Expanding on *in vitro* findings, the trifluoperazine and volasertib combination should next be evaluated in non-transformed glial and neuronal cultures to assess selectivity and potential neurotoxicity. Parallel screening across additional glioblastoma models, including p53-mutant, PTEN wild-type, unmethylated MGMT promoter harbouring cell lines, and patient-derived primary cultures, will determine whether efficacy extends beyond U87-MG and A172 cells. In addition, incorporating models to express constitutively active EGFR, such as U87/A172-EGFRvIII, could improve translational relevance due to the wild-type EGFR status of these cell lines, especially regarding their vulnerabilities to sorafenib treatment. Moreover, a broader concentration series of at least eight doses should be applied to each prioritized kinase inhibitor to obtain more precise IC50 values, and comprehensive dose-response matrices of trifluoperazine and volasertib combinations should be tested to identify cellular responses across varying concentration pairings in tested cell lines including A172.

Given trifluoperazine's known ability to inhibit cell migration via blockade of the calcium–calmodulin signaling, scratch assays, transwell migration assays, or live-cell imaging–based motility tracking could be performed to quantitatively assess the migratory behaviour of GBM cells following treatment with 10 μM TFP alone and in combination with volasertib. Such experiments could help determine whether the observed cytotoxic synergy extends to suppression of migratory capacity.

To elucidate the molecular mechanisms underlying the synergistic interaction of trifluoperazine and volasertib, comprehensive transcriptomic and protein-level analyses should be performed. These studies should best be accompanied by prolonged combination treatments to monitor resistance emergence and reveal potential vulnerabilities.

Given the antagonistic interactions of trifluoperazine observed with certain VEGFR and Src inhibitors, detailed biochemical studies and pathway analyses are needed. In particular, the Src inhibitor SU6656 and trifluoperazine combination can be further investigated to map the pathway crosstalk responsible for reversed growth-inhibitory effects.

Survival analysis of the TCGA-GBM cohort can be extended to stratify patients by PTEN and TP53 mutation status in order to evaluate the prognostic impact of the volasertib induced gene signature across distinct genetic backgrounds. In addition, the transcriptional profile elicited by the combined treatment of volasertib and trifluoperazine can be characterized to validate the observed synergy in U87-MG cells.

A clinically oriented next step would be to co-test TFP and volasertib with temozolomide (TMZ) in the same models used here using dose-response matrices to quantify synergy. These experiments should also compare schedules such as priot TMZ treatment followed by volasertib with and without TFP addition to identify the most effective sequence. For validation and translational robustness, the triple regimen should then be evaluated in MGMT-unmethylated GBM lines that model TMZ resistance. Consistent efficacy across these backgrounds would strengthen the rationale for *in vivo* studies.

The *in vivo gfap*:GFP fluorescence screen would benefit from three-dimensional imaging modalities such as z-stacking. In addition, the association of fluorescence quantification with glial reporter expression should be validated by quantifying endogenous GFAP protein levels via Western blot or immunohistochemistry to confirm accuracy.

The brain-orthotopic U87-GFP xenograft model in larval zebrafish should be refined by implementing daily monitoring of engrafted cancer cells, while assessment of cell proliferation rates and graft persistence will enable precise evaluation of drug effects on both tumour growth and host tissue responses.

To strengthen the interpretation of behavioural consequences of drug treatments or micromanipulation, the automated locomotor assay platform must be expanded with additional protocols, including varied dark:light alternation cycles and durations. In addition, protocol assessments in ache(+/-) and tp53(-/-) mutant zebrafish lines available in the lab could provide valuable insights into whether the startle-response phenotyping differs across genetic backgrounds.

Finally, the decrease in overall locomotion observed in mock-injected larvae should be further investigated to determine how and to what extent the microinjection procedure induces stress, thereby establishing the most appropriate control conditions for the xenograft model.

REFERENCES

Abate, M., Laezza, C., Pisanti, S., Torelli, G., Seneca, V., Catapano, G., Montella, F., Ranieri, R., Notarnicola, M., & Gazzerro, P. (2017). Deregulated expression and activity of Farnesyl Diphosphate Synthase (FDPS) in Glioblastoma. *Scientific reports*, *7*(1), 14123.

Abbou, S., Lanvers-Kaminsky, C., Daudigeos-Dubus, E., Le Dret, L., Laplace-Builhe, C., Molenaar, J., Vassal, G., & Geoerger, B. (2016). Polo-like kinase inhibitor volasertib exhibits antitumor activity and synergy with vincristine in pediatric malignancies. *Anticancer research*, *36*(2), 599-609.

Abou Khouzam, R., Janji, B., Thiery, J., Zaarour, R. F., Chamseddine, A. N., Mayr, H., Savagner, P., Kieda, C., Gad, S., & Buart, S. (2023). Hypoxia as a potential inducer of immune tolerance, tumor plasticity and a driver of tumor mutational burden: Impact on cancer immunotherapy. Seminars in Cancer Biology,

Achinger-Kawecka, J., Valdes-Mora, F., Luu, P.-L., Giles, K. A., Caldon, C. E., Qu, W., Nair, S., Soto, S., Locke, W. J., & Yeo-Teh, N. S. (2020). Epigenetic reprogramming at estrogen-receptor binding sites alters 3D chromatin landscape in endocrine-resistant breast cancer. *Nature communications*, *11*(1), 320.

Adjibade, P., St-Sauveur, V. G., Huberdeau, M. Q., Fournier, M.-J., Savard, A., Coudert, L., Khandjian, E. W., & Mazroui, R. (2015). Sorafenib, a multikinase inhibitor, induces formation of stress granules in hepatocarcinoma cells. *Oncotarget*, *6*(41), 43927.

Afrikanova, T., Serruys, A.-S. K., Buenafe, O. E., Clinckers, R., Smolders, I., de Witte, P. A., Crawford, A. D., & Esguerra, C. V. (2013). Validation of the zebrafish pentylenetetrazol seizure model: locomotor versus electrographic responses to antiepileptic drugs. *PLoS One*, *8*(1), e54166.

Ahn, H.-J., Kim, G., & Park, K.-S. (2013). Ell3 stimulates proliferation, drug resistance, and cancer stem cell properties of breast cancer cells via a MEK/ERK-dependent signaling pathway. *Biochemical and biophysical research communications*, *437*(4), 557-564.

Alcantara Llaguno, S. R., & Parada, L. F. (2016). Cell of origin of glioma: biological and clinical implications. *British journal of cancer*, *115*(12), 1445-1450.

Alexander, B., Supko, J., Agar, N., Ahluwalia, M., Desai, A., Dietrich, J., Kaley, T., Peereboom, D., Takebe, N., & Desideri, S. (2018). ACTR-14. Phase i study of azd1775 with radiation therapy (RT) and temozolomide (TMZ) in patients with newly diagnosed glioblastoma (GBM) and evaluation of intratumoral drug distribution (idd) in patients with recurrent GBM. *Neuro-Oncology*, *20*(Suppl 6), vi13.

Alhajala, H. S., Markley, J. L., Kim, J. H., Al-Gizawiy, M. M., Schmainda, K. M., Kuo, J. S., & Chitambar, C. R. (2020). The cytotoxicity of gallium maltolate in glioblastoma cells is enhanced by metformin through combined action on mitochondrial complex 1. *Oncotarget*, *11*(17), 1531.

Alles, M. C., Gardiner-Garden, M., Nott, D. J., Wang, Y., Foekens, J. A., Sutherland, R. L., Musgrove, E. A., & Ormandy, C. J. (2009). Meta-analysis and gene set enrichment relative to er status reveal elevated activity of MYC and E2F in the "basal" breast cancer subgroup. *PLoS One*, *4*(3), e4710.

Amatya, P. N., Kim, H.-B., Park, S.-J., Youn, C.-K., Hyun, J.-W., Chang, I.-Y., Lee, J.-H., & You, H. J. (2012). A role of DNA-dependent protein kinase for the activation of AMP-activated protein kinase in response to glucose deprivation. *Biochimica et Biophysica Acta (BBA)-Molecular Cell Research*, *1823*(12), 2099-2108.

Amin, A. G., Jeong, S. W., Gillick, J. L., Sursal, T., Murali, R., Gandhi, C. D., & Jhanwar-Uniyal, M. (2021). Targeting the mTOR pathway using novel ATP-competitive inhibitors, Torin1, Torin2 and XL388, in the treatment of glioblastoma. *International journal of oncology*, *59*(4), 83.

Antonica, F., Santomaso, L., Pernici, D., Petrucci, L., Aiello, G., Cutarelli, A., Conti, L., Romanel, A., Miele, E., & Tebaldi, T. (2022). A slow-cycling/quiescent cells subpopulation is involved in glioma invasiveness. *Nature communications*, *13*(1), 4767.

Attwood, M. M., Fabbro, D., Sokolov, A. V., Knapp, S., & Schiöth, H. B. (2021). Trends in kinase drug discovery: targets, indications and inhibitor design. *Nature Reviews Drug Discovery*, *20*(11), 839-861.

Augello, G., Puleio, R., Emma, M. R., Cusimano, A., Loria, G. R., McCubrey, J. A., Montalto, G., & Cervello, M. (2016). A PTEN inhibitor displays preclinical activity against hepatocarcinoma cells. *Cell Cycle*, *15*(4), 573-583.

Bakker, W. J., Harris, I. S., & Mak, T. W. (2007). FOXO3a is activated in response to hypoxic stress and inhibits HIF1-induced apoptosis via regulation of CITED2. *Molecular cell*, *28*(6), 941-953.

Baltanás, F. C., García-Navas, R., Rodríguez-Ramos, P., Calzada, N., Cuesta, C., Borrajo, J., Fuentes-Mateos, R., Olarte-San Juan, A., Vidaña, N., & Castellano, E. (2023). Critical requirement of SOS1 for tumor development and microenvironment modulation in KRASG12D-driven lung adenocarcinoma. *Nature communications*, *14*(1), 5856.

Baltuch, G. H., Couldwell, W. T., Villemure, J.-G., & Yong, V. W. (1993). Protein kinase C inhibitors suppress cell growth in established and low-passage glioma cell lines. A comparison between staurosporine and tamoxifen. *Neurosurgery*, *33*(3), 495-501.

Banono, N. S., & Esguerra, C. (2020). Pharmacological validation of the prepulse inhibition of startle response in larval zebrafish using a commercial automated system and software. *Journal of Visualized Experiments*, *161*(161).

Bartoszek, A., Trzpil, A., Kozub, A., & Fornal, E. (2023). Optimization of the zebrafish larvae pentylenetetrazol-induced seizure model for the study of caffeine and topiramate interactions. *International Journal of Molecular Sciences*, *24*(16), 12723.

Basnet, R. M., Zizioli, D., Taweedet, S., Finazzi, D., & Memo, M. (2019). Zebrafish larvae as a behavioral model in neuropharmacology. *Biomedicines*, *7*(1), 23.

Battistelli, C., Garbo, S., & Maione, R. (2022). MyoD-induced trans-differentiation: a paradigm for dissecting the molecular mechanisms of cell commitment, differentiation and reprogramming. *Cells*, *11*(21), 3435.

Benary, M., Bohn, S., Lüthen, M., Nolis, I. K., Blüthgen, N., & Loewer, A. (2020). Disentangling pro-mitotic signaling during cell cycle progression using time-resolved single-cell imaging. *Cell reports*, *31*(2).

Berchtold, M. W., & Villalobo, A. (2014). The many faces of calmodulin in cell proliferation, programmed cell death, autophagy, and cancer. *Biochimica et Biophysica Acta (BBA)-Molecular Cell Research*, *1843*(2), 398-435.

Bhat, K., Saki, M., Vlashi, E., Cheng, F., Duhachek-Muggy, S., Alli, C., Yu, G., Medina, P., He, L., & Damoiseaux, R. (2020). The dopamine receptor antagonist trifluoperazine prevents phenotype conversion and improves survival in mouse models of glioblastoma. *Proceedings of the National Academy of Sciences*, *117*(20), 11085-11096.

Bkaily, G., Sperelakis, N., & Eldefrawi, M. (1984). Effects of the calmodulin inhibitor, trifluoperazine, on membrane potentials and slow action potentials of cultured heart cells. *European journal of pharmacology*, *105*(1-2), 23-31.

Brennan, C. W., Verhaak, R. G., McKenna, A., Campos, B., Noushmehr, H., Salama, S. R., Zheng, S., Chakravarty, D., Sanborn, J. Z., & Berman, S. H. (2013). The somatic genomic landscape of glioblastoma. *Cell*, *155*(2), 462-477.

Burgess, H. A., & Granato, M. (2007). Modulation of locomotor activity in larval zebrafish during light adaptation. *Journal of Experimental Biology*, *210*(14), 2526-2539.

Cabezas-Camarero, S., Pérez-Alfayate, R., Polidura, C., Gómez-Ruiz, M. N., Gil-Martínez, L., Casado-Fariñas, I., Bartolomé, J., & Pérez-Segura, P. (2024). Durable benefit and slowdown in tumor growth dynamics with erdafitinib in a FGFR3-TACC3 fusion-positive IDH-wild type glioblastoma. *Neuro-Oncology Advances*, *6*(1), vdae139.

Can, W., Yan, W., Luo, H., Xin, Z., Yan, L., Deqing, L., Honglei, T., Xiaoyu, L., Jiangdong, S., & Yue, X. (2024). ADCY5 act as a putative tumor suppressor in glioblastoma: An integrated analysis. *Heliyon*, *10*(17).

Cardona, A. F., Jaramillo-Velásquez, D., Ruiz-Patiño, A., Polo, C., Jiménez, E., Hakim, F., Gómez, D., Ramón, J. F., Cifuentes, H., & Mejía, J. A. (2021). Efficacy of osimertinib plus bevacizumab

in glioblastoma patients with simultaneous EGFR amplification and EGFRvIII mutation. *Journal of Neuro-Oncology*, *154*(3), 353-364.
Carmo, A. d., Balça-Silva, J., Matias, D., & Lopes, M. (2013). PKC signaling in glioblastoma. *Cancer biology & therapy*, *14*(4), 287-294.
Carra, E., Barbieri, F., Marubbi, D., Pattarozzi, A., Favoni, R. E., Florio, T., & Daga, A. (2013). Sorafenib selectively depletes human glioblastoma tumor-initiating cells from primary cultures. *Cell Cycle*, *12*(3), 491-500.
Catacuzzeno, L., & Franciolini, F. (2018). Role of KCa3. 1 channels in modulating Ca2+ oscillations during glioblastoma cell migration and invasion. *International Journal of Molecular Sciences*, *19*(10), 2970.
Chatree, S., Thongmaen, N., Tantivejkul, K., Sitticharoon, C., & Vucenik, I. (2020). Role of inositols and inositol phosphates in energy metabolism. *Molecules*, *25*(21), 5079.
Chen, X.-K., Kwan, J. S.-K., Wong, G. T.-C., Yi, Z.-N., Ma, A. C.-H., & Chang, R. C.-C. (2022). Leukocyte invasion of the brain after peripheral trauma in zebrafish (Danio rerio). *Experimental & Molecular Medicine*, *54*(7), 973-987.
Chen, Z., Gopalakrishnan, S. M., Bui, M.-H., Soni, N. B., Warrior, U., Johnson, E. F., Donnelly, J. B., & Glaser, K. B. (2011). 1-Benzyl-3-cetyl-2-methylimidazolium iodide (NH125) induces phosphorylation of eukaryotic elongation factor-2 (eEF2): a cautionary note on the anticancer mechanism of an eEF2 kinase inhibitor. *Journal of Biological Chemistry*, *286*(51), 43951-43958.
Cheng, C. K., Gustafson, W. C., Charron, E., Houseman, B. T., Zunder, E., Goga, A., Gray, N. S., Pollok, B., Oakes, S. A., & James, C. D. (2012). Dual blockade of lipid and cyclin-dependent kinases induces synthetic lethality in malignant glioma. *Proceedings of the National Academy of Sciences*, *109*(31), 12722-12727.
Cheng, H., Kari, G., Dicker, A. P., Rodeck, U., Koch, W. J., & Force, T. (2011). A novel preclinical strategy for identifying cardiotoxic kinase inhibitors and mechanisms of cardiotoxicity. *Circulation research*, *109*(12), 1401-1409.
Cheng, H., Liang, Y., Kuo, Y., Chuu, C., Lin, C., Lee, M., Wu, A., Yeh, C.-T., Chen, E. I., & Whang-Peng, J. (2015). Identification of thioridazine, an antipsychotic drug, as an antiglioblastoma and anticancer stem cell agent using public gene expression data. *Cell death & disease*, *6*(5), e1753-e1753.
Cheng, P., Phillips, E., Kim, S.-H., Taylor, D., Hielscher, T., Puccio, L., Hjelmeland, A. B., Lichter, P., Nakano, I., & Goidts, V. (2015). Kinome-wide shRNA screen identifies the receptor tyrosine kinase AXL as a key regulator for mesenchymal glioblastoma stem-like cells. *Stem cell reports*, *4*(5), 899-913.
Cheng, Y.-C., Tsao, M.-J., Chiu, C.-Y., Kan, P.-C., & Chen, Y. (2018). Magnolol inhibits human glioblastoma cell migration by regulating N-cadherin. *Journal of Neuropathology & Experimental Neurology*, *77*(6), 426-436.
Chimote, G., Sreenivasan, J., Pawar, N., Subramanian, J., Sivaramakrishnan, H., & Sharma, S. (2014). Comparison of effects of anti-angiogenic agents in the zebrafish efficacy–toxicity model for translational anti-angiogenic drug discovery. *Drug design, development and therapy*, 1107-1123.
Choi, T.-Y., Choi, T.-I., Lee, Y.-R., Choe, S.-K., & Kim, C.-H. (2021). Zebrafish as an animal model for biomedical research. *Experimental & Molecular Medicine*, *53*(3), 310-317.
Cholewa, B. D., Ndiaye, M. A., Huang, W., Liu, X., & Ahmad, N. (2017). Small molecule inhibition of polo-like kinase 1 by volasertib (BI 6727) causes significant melanoma growth delay and regression in vivo. *Cancer letters*, *385*, 179-187.
Clapham, D. E. (1995). Calcium signaling. *Cell*, *80*(2), 259-268.
Cohen, P., Cross, D., & Jänne, P. A. (2021). Kinase drug discovery 20 years after imatinib: progress and future directions. *Nature Reviews Drug Discovery*, *20*(7), 551-569.
Colardo, M., Segatto, M., & Di Bartolomeo, S. (2021). Targeting RTK-PI3K-mTOR axis in gliomas: an update. *International Journal of Molecular Sciences*, *22*(9), 4899.
Collin, G., Huna, A., Warnier, M., Flaman, J.-M., & Bernard, D. (2018). Transcriptional repression of DNA repair genes is a hallmark and a cause of cellular senescence. *Cell death & disease*, *9*(3), 259.

Cortes Ballen, A. I., Amosu, M., Ravinder, S., Chan, J., Derin, E., Slika, H., & Tyler, B. (2024). Metabolic reprogramming in glioblastoma multiforme: a review of pathways and therapeutic targets. *Cells*, *13*(18), 1574.

Cui, Y., Wu, H., Yang, L., Huang, T., Li, J., Gong, X., Li, L., Sun, X., Mao, F., & Wang, Y. (2021). Chlorpromazine sensitizes progestin-resistant endometrial cancer cells to MPA by upregulating PRB. *Frontiers in Oncology*, *11*, 665832.

Datta, K., Babbar, P., Srivastava, T., Sinha, S., & Chattopadhyay, P. (2002). p53 dependent apoptosis in glioma cell lines in response to hydrogen peroxide induced oxidative stress. *The international journal of biochemistry & cell biology*, *34*(2), 148-157.

David, C. J., & Massagué, J. (2018). Contextual determinants of TGFβ action in development, immunity and cancer. *Nature reviews Molecular cell biology*, *19*(7), 419-435.

de Braud, F., Cascinu, S., Spitaleri, G., Pilz, K., Clementi, L., Liu, D., Sikken, P., & De Pas, T. (2015). A phase I, dose-escalation study of volasertib combined with nintedanib in advanced solid tumors. *Annals of Oncology*, *26*(11), 2341-2346.

De Silva, M. I., Gan, H. K., & Bardy, C. (2025). Repurposing trifluoperazine for glioblastoma treatment. *Trends in Pharmacological Sciences*.

De Witt Hamer, P. C. (2010). Small molecule kinase inhibitors in glioblastoma: a systematic review of clinical studies. *Neuro-Oncology*, *12*(3), 304-316.

DeAngelo, D. J., Sekeres, M. A., Ottmann, O. G., Sanz, M. A., Naoe, T., Taube, T., Belsack, V., Ge, M., & Döhner, H. (2015). Phase III randomized trial of volasertib combined with low-dose cytarabine (LDAC) versus placebo plus LDAC in patients aged≥ 65 years with previously untreated, acute myeloid leukemia (AML) ineligible for intensive remission induction therapy. *Clinical Lymphoma, Myeloma and Leukemia*, *15*, S194.

Deschenes, M., & Chabot, B. (2017). The emerging role of alternative splicing in senescence and aging. *Aging cell*, *16*(5), 918-933.

Desjardins, A., Gromeier, M., Herndon, J. E., Beaubier, N., Bolognesi, D. P., Friedman, A. H., Friedman, H. S., McSherry, F., Muscat, A. M., & Nair, S. (2018). Recurrent glioblastoma treated with recombinant poliovirus. *New England journal of medicine*, *379*(2), 150-161.

Dewdney, B., Jenkins, M. R., Best, S. A., Freytag, S., Prasad, K., Holst, J., Endersby, R., & Johns, T. G. (2023). From signalling pathways to targeted therapies: unravelling glioblastoma's secrets and harnessing two decades of progress. *Signal Transduction and Targeted Therapy*, *8*(1), 400.

Döhner, H., Lübbert, M., Fiedler, W., Fouillard, L., Haaland, A., Brandwein, J. M., Lepretre, S., Reman, O., Turlure, P., & Ottmann, O. G. (2014). Randomized, phase 2 trial of low-dose cytarabine with or without volasertib in AML patients not suitable for induction therapy. *Blood, The Journal of the American Society of Hematology*, *124*(9), 1426-1433.

Dong, J., Park, S. Y., Nguyen, N., Ezhilarasan, R., Martinez-Ledesma, E., Wu, S., Henry, V., Piao, Y., Tiao, N., & Brunell, D. (2018). The polo-like kinase 1 inhibitor volasertib synergistically increases radiation efficacy in glioma stem cells. *Oncotarget*, *9*(12), 10497.

Doroszko, M., Stockgard, R., Uppman, I., Heinold, J., Voukelatou, F., Mangukiya, H. B., Millner, T. O., Skeppås, M., Ballester Bravo, M., & Elgendy, R. (2025). The invasion phenotypes of glioblastoma depend on plastic and reprogrammable cell states. *Nature communications*, *16*(1), 6662.

Dovey, C. M., Diep, J., Clarke, B. P., Hale, A. T., McNamara, D. E., Guo, H., Brown, N. W., Cao, J. Y., Grace, C. R., & Gough, P. J. (2018). MLKL requires the inositol phosphate code to execute necroptosis. *Molecular cell*, *70*(5), 936-948. e937.

Du, Z., Whitt, M. A., Baumann, J., Garner, J. M., Morton, C. L., Davidoff, A. M., & Pfeffer, L. M. (2012). Inhibition of type I interferon-mediated antiviral action in human glioma cells by the IKK inhibitors BMS-345541 and TPCA-1. *Journal of Interferon & Cytokine Research*, *32*(8), 368-377.

Fan, S., Chen, Y., Wang, W., Xu, W., Tian, M., Liu, Y., Zhou, Y., Liu, D., Xia, Q., & Dong, L. (2024). Pharmacological and Biological Targeting of FGFR1 in Cancer. *Current Issues in Molecular Biology*, *46*(11), 13131-13150.

Fan, X., Matsui, W., Khaki, L., Stearns, D., Chun, J., Li, Y.-M., & Eberhart, C. G. (2006). Notch pathway inhibition depletes stem-like cells and blocks engraftment in embryonal brain tumors. *Cancer research*, *66*(15), 7445-7452.

Fang, C., Dai, L., Wang, C., Fan, C., Yu, Y., Yang, L., Deng, H., & Zhou, Z. (2021). Secretogranin II impairs tumor growth and angiogenesis by promoting degradation of hypoxia-inducible factor-1α in colorectal cancer. *Molecular Oncology*, *15*(12), 3513-3526.

Feng, Z., Xia, Y., Gao, T., Xu, F., Lei, Q., Peng, C., Yang, Y., Xue, Q., Hu, X., & Wang, Q. (2018). The antipsychotic agent trifluoperazine hydrochloride suppresses triple-negative breast cancer tumor growth and brain metastasis by inducing G0/G1 arrest and apoptosis. *Cell death & disease*, *9*(10), 1006.

Ferri, A., Stagni, V., & Barilà, D. (2020). Targeting the DNA damage response to overcome cancer drug resistance in glioblastoma. *International Journal of Molecular Sciences*, *21*(14), 4910.

Filipovich, E., Gorodkova, E., Shcherbakova, A., Asaad, W., Popov, S., Melnichenko, G., Mokrysheva, N., & Utkina, M. (2025). The role of cell cycle-related genes in the tumorigenesis of adrenal and thyroid neuroendocrine tumors. *Heliyon*, *11*(1).

Fontana, B. D., & Parker, M. O. (2022). The larval diving response (LDR): Validation of an automated, high-throughput, ecologically relevant measure of anxiety-related behavior in larval zebrafish (Danio rerio). *Journal of neuroscience methods*, *381*, 109706.

Fu, W., Hou, X., Dong, L., & Hou, W. (2023). Roles of STAT3 in the pathogenesis and treatment of glioblastoma. *Frontiers in Cell and Developmental Biology*, *11*, 1098482.

Furnari, F. B., Fenton, T., Bachoo, R. M., Mukasa, A., Stommel, J. M., Stegh, A., Hahn, W. C., Ligon, K. L., Louis, D. N., & Brennan, C. (2007). Malignant astrocytic glioma: genetics, biology, and paths to treatment. *Genes & development*, *21*(21), 2683-2710.

Gamble, J. T., Elson, D. J., Greenwood, J. A., Tanguay, R. L., & Kolluri, S. K. (2021). The zebrafish xenograft models for investigating cancer and cancer therapeutics. *Biology*, *10*(4), 252.

García-Gutiérrez, L., Delgado, M., & León, J. (2019). MYC oncogene contributions to release of cell cycle brakes. Genes (Basel) 10: 244. In.

Gawi Ermi, A., & Sarkar, D. (2024). Resistance to Tyrosine Kinase Inhibitors in Hepatocellular Carcinoma (HCC): Clinical Implications and Potential Strategies to Overcome the Resistance. *Cancers*, *16*(23), 3944.

Georgescu, M.-M. (2010). PTEN tumor suppressor network in PI3K-Akt pathway control. *Genes & cancer*, *1*(12), 1170-1177.

Giacich, M., Marchese, M., Damiani, D., Santorelli, F. M., & Naef, V. (2025). Eyes Wide Open: Assessing Early Visual Behavior in Zebrafish Larvae. *Biology*, *14*(8), 934.

Gil del Alcazar, C. R., Hardebeck, M. C., Mukherjee, B., Tomimatsu, N., Gao, X., Yan, J., Xie, X.-J., Bachoo, R., Li, L., & Habib, A. A. (2014). Inhibition of DNA double-strand break repair by the dual PI3K/mTOR inhibitor NVP-BEZ235 as a strategy for radiosensitization of glioblastoma. *Clinical Cancer Research*, *20*(5), 1235-1248.

Gjertsen, B. T., & Schöffski, P. (2015). Discovery and development of the Polo-like kinase inhibitor volasertib in cancer therapy. *Leukemia*, *29*(1), 11-19.

Golán-Cancela, I., & Caja, L. (2024). The TGF-β family in glioblastoma. *International Journal of Molecular Sciences*, *25*(2), 1067.

Gulhati, P., Zaytseva, Y. Y., Valentino, J. D., Stevens, P. D., Kim, J. T., Sasazuki, T., Shirasawa, S., Lee, E. Y., Weiss, H. L., & Dong, J. (2012). Sorafenib enhances the therapeutic efficacy of rapamycin in colorectal cancers harboring oncogenic KRAS and PIK3CA. *Carcinogenesis*, *33*(9), 1782-1790.

Guo, X., Zhou, S., Yang, Z., Li, Z.-A., Hu, W., Dai, L., Liang, W., & Wang, X. (2022). Cholesterol metabolism and its implication in glioblastoma therapy. *Journal of Cancer*, *13*(6), 1745.

Hadian, K. (2020). Ferroptosis suppressor protein 1 (FSP1) and coenzyme Q10 cooperatively suppress ferroptosis. *Biochemistry*, *59*(5), 637-638.

Hadian, K., & Stockwell, B. R. (2020). SnapShot: ferroptosis. *Cell*, *181*(5), 1188-1188. e1181.

Hambardzumyan, D., Gutmann, D. H., & Kettenmann, H. (2016). The role of microglia and macrophages in glioma maintenance and progression. *Nature neuroscience*, *19*(1), 20-27.

Han, M., Wang, S., Yang, N., Wang, X., Zhao, W., Saed, H. S., Daubon, T., Huang, B., Chen, A., & Li, G. (2020). Therapeutic implications of altered cholesterol homeostasis mediated by loss of CYP46A1 in human glioblastoma. *EMBO Molecular Medicine*, *12*(1), e10924.

Hänzelmann, S., Castelo, R., & Guinney, J. (2013). GSVA: gene set variation analysis for microarray and RNA-seq data. *BMC bioinformatics*, *14*(1), 7.

Harikumar, K. B., Kunnumakkara, A. B., Ochi, N., Tong, Z., Deorukhkar, A., Sung, B., Kelland, L., Jamieson, S., Sutherland, R., & Raynham, T. (2010). A novel small-molecule inhibitor of protein kinase D blocks pancreatic cancer growth in vitro and in vivo. *Molecular cancer therapeutics*, *9*(5), 1136-1146.

Harmalkar, M. N., & Shirsat, N. V. (2006). Staurosporine-induced growth inhibition of glioma cells is accompanied by altered expression of cyclins, CDKs and CDK inhibitors. *Neurochemical research*, *31*(5), 685-692.

He, L., Ioannidis, A., Hoffman, C. J., Arambula, E., Joshi, P., Whitelegge, J., Liau, L. M., Kornblum, H. I., & Pajonk, F. (2024). Activation of the mevalonate pathway in response to anti-cancer treatments drives glioblastoma recurrences through activation of Rac-1. *Cancer Research Communications*, *4*(6), 1566-1580.

He, Y., Sun, M. M., Zhang, G. G., Yang, J., Chen, K. S., Xu, W. W., & Li, B. (2021). Targeting PI3K/Akt signal transduction for cancer therapy. *Signal Transduction and Targeted Therapy*, *6*(1), 425.

Hegi, M. E., Diserens, A.-C., Gorlia, T., Hamou, M.-F., De Tribolet, N., Weller, M., Kros, J. M., Hainfellner, J. A., Mason, W., & Mariani, L. (2005). MGMT gene silencing and benefit from temozolomide in glioblastoma. *New England journal of medicine*, *352*(10), 997-1003.

Hillig, R. C., Sautier, B., Schroeder, J., Moosmayer, D., Hilpmann, A., Stegmann, C. M., Werbeck, N. D., Briem, H., Boemer, U., & Weiske, J. (2019). Discovery of potent SOS1 inhibitors that block RAS activation via disruption of the RAS–SOS1 interaction. *Proceedings of the National Academy of Sciences*, *116*(7), 2551-2560.

Hillman, C., Kearn, J., & Parker, M. O. (2024). A unified approach to investigating 4 dpf zebrafish larval behaviour through a standardised light/dark assay. *Progress in Neuro-Psychopharmacology and Biological Psychiatry*, *134*, 111084.

Hu, C., Sun, L., Chen, J., Lyu, Z., Yuan, C., & Jiang, X. (2024). Advantages of the zebrafish tumor xenograft model: the evaluation of efficacy in cancer therapy and the application to the study of lncRNAs. *Frontiers in Immunology*, *15*, 1483192.

Hu, H. J., Wang, S. S., Wang, Y. X., Liu, Y., Feng, X. M., Shen, Y., Zhu, L., Chen, H. Z., & Song, M. (2019). Blockade of the forward Na+/Ca2+ exchanger suppresses the growth of glioblastoma cells through Ca2+-mediated cell death. *British Journal of Pharmacology*, *176*(15), 2691-2707.

Huang, W., Hao, Z., Mao, F., & Guo, D. (2022). Small molecule inhibitors in adult high-grade glioma: from the past to the future. *Frontiers in Oncology*, *12*, 911876.

Huang, X., Li, X., & Guo, B. (2008). KLF6 induces apoptosis in prostate cancer cells through up-regulation of ATF3. *Journal of Biological Chemistry*, *283*(44), 29795-29801.

Hwang, E., Yoo, K.-C., Kang, S.-G., Kim, R.-K., Cui, Y.-H., Lee, H.-J., Kim, M.-J., Lee, J.-S., Kim, I.-G., & Suh, Y. (2015). PKCδ activated by c-MET enhances infiltration of human glioblastoma cells through NOTCH2 signaling. *Oncotarget*, *7*(4), 4890.

Jarema, K. A., Hunter, D. L., Hill, B. N., Olin, J. K., Britton, K. N., Waalkes, M. R., & Padilla, S. (2022). Developmental neurotoxicity and behavioral screening in larval zebrafish with a comparison to other published results. *Toxics*, *10*(5), 256.

Jaszczyszyn, A., Gąsiorowski, K., Świątek, P., Malinka, W., Cieślik-Boczula, K., Petrus, J., & Czarnik-Matusewicz, B. (2012). Chemical structure of phenothiazines and their biological activity. *Pharmacological Reports*, *64*(1), 16-23.

Jewell, J. L., Russell, R. C., & Guan, K.-L. (2013). Amino acid signalling upstream of mTOR. *Nature reviews Molecular cell biology*, *14*(3), 133-139.

Jhou, A.-J., Chang, H.-C., Hung, C.-C., Lin, H.-C., Lee, Y.-C., Liu, W.-t., Han, K.-F., Lai, Y.-W., Lin, M.-Y., & Lee, C.-H. (2021). Chlorpromazine, an antipsychotic agent, induces G2/M phase arrest and apoptosis via regulation of the PI3K/AKT/mTOR-mediated autophagy pathways in human oral cancer. *Biochemical pharmacology*, *184*, 114403.

Jiang, W., Li, G., Li, W., Wang, P., Xiu, P., Jiang, X., Liu, B., Sun, X., & Jiang, H. (2018). Sodium orthovanadate overcomes sorafenib resistance of hepatocellular carcinoma cells by inhibiting Na+/K+-ATPase activity and hypoxia-inducible pathways. *Scientific reports*, *8*(1), 9706.
Kalam Shamsuddin, A., & Bose, S. (2012). IP6 (Inositol Hexaphosphate) as a signaling molecule. *Current Signal Transduction Therapy*, *7*(3), 289-304.
Kamgar-Dayhoff, P., & Brelidze, T. I. (2021). Multifaceted effect of chlorpromazine in cancer: Implications for cancer treatment. *Oncotarget*, *12*(14), 1406.
Kataba, A., Botha, T. L., Nakayama, S. M., Yohannes, Y. B., Ikenaka, Y., Wepener, V., & Ishizuka, M. (2020). Acute exposure to environmentally relevant lead levels induces oxidative stress and neurobehavioral alterations in larval zebrafish (Danio rerio). *Aquatic toxicology*, *227*, 105607.
Kawabata, M., Umemoto, N., Shimada, Y., Nishimura, Y., Zhang, B., Kuroyanagi, J., Miyabe, M., & Tanaka, T. (2015). Downregulation of stanniocalcin 1 is responsible for sorafenib-induced cardiotoxicity. *Toxicological Sciences*, *143*(2), 374-384.
Kim, Y., Varn, F. S., Park, S.-H., Yoon, B. W., Park, H. R., Lee, C., Verhaak, R. G., & Paek, S. H. (2021). Perspective of mesenchymal transformation in glioblastoma. *Acta neuropathologica communications*, *9*(1), 50.
Kleihues, P., Louis, D. N., Scheithauer, B. W., Rorke, L. B., Reifenberger, G., Burger, P. C., & Cavenee, W. K. (2002). The WHO classification of tumors of the nervous system. *Journal of Neuropathology & Experimental Neurology*, *61*(3), 215-225.
Korbecki, J., Kojder, K., Jeżewski, D., Simińska, D., Tarnowski, M., Kopytko, P., Safranow, K., Gutowska, I., Goschorska, M., & Kolasa-Wołosiuk, A. (2020). Expression of SCD and FADS2 is lower in the necrotic core and growing tumor area than in the peritumoral area of glioblastoma multiforme. *Biomolecules*, *10*(5), 727.
Koundouros, N., & Poulogiannis, G. (2020). Reprogramming of fatty acid metabolism in cancer. *British journal of cancer*, *122*(1), 4-22.
Krishna, S., Choudhury, A., Keough, M. B., Seo, K., Ni, L., Kakaizada, S., Lee, A., Aabedi, A., Popova, G., & Lipkin, B. (2023). Glioblastoma remodelling of human neural circuits decreases survival. *Nature*, *617*(7961), 599-607.
Kusne, Y., Carrera-Silva, E. A., Perry, A. S., Rushing, E. J., Mandell, E. K., Dietrich, J. D., Errasti, A. E., Gibbs, D., Berens, M. E., & Loftus, J. C. (2014). Targeting aPKC disables oncogenic signaling by both the EGFR and the proinflammatory cytokine TNFα in glioblastoma. *Science signaling*, *7*(338), ra75-ra75.
Lan, Y.-L., Zou, S., Wang, X., Lou, J.-C., Xing, J.-S., Yu, M., & Zhang, B. (2017). Update on the therapeutic significance of estrogen receptor beta in malignant gliomas. *Oncotarget*, *8*(46), 81686.
Langhans, J., Schneele, L., Trenkler, N., von Bandemer, H., Nonnenmacher, L., Karpel-Massler, G., Siegelin, M. D., Zhou, S., Halatsch, M.-E., & Debatin, K.-M. (2017). The effects of PI3K-mediated signalling on glioblastoma cell behaviour. *Oncogenesis*, *6*(11), 398.
Leduc, C., & Etienne-Manneville, S. (2015). Intermediate filaments in cell migration and invasion: the unusual suspects. *Current opinion in cell biology*, *32*, 102-112.
Lee, J.-K., Joo, K. M., Lee, J., Yoon, Y., & Nam, D.-H. (2014). Targeting the epithelial to mesenchymal transition in glioblastoma: the emerging role of MET signaling. *OncoTargets and therapy*, 1933-1944.
Li, A., Chen, X., Jing, Z., & Chen, J. (2020). Trifluoperazine induces cellular apoptosis by inhibiting autophagy and targeting NUPR1 in multiple myeloma. *FEBS Open Bio*, *10*(10), 2097-2106.
Li, D., Li, T., Shang, Z., Zhao, L., Xu, Q., Tan, J., Qin, Y., Zhang, Y., Cao, Y., & Wang, N. (2020). Combined inhibition of Notch and FLT3 produces synergistic cytotoxic effects in FLT3/ITD+ acute myeloid leukemia. *Signal Transduction and Targeted Therapy*, *5*(1), 21.
Li, J., Cao, F., Yin, H.-l., Huang, Z.-j., Lin, Z.-t., Mao, N., Sun, B., & Wang, G. (2020). Ferroptosis: past, present and future. *Cell death & disease*, *11*(2), 88.
Li, J., Gong, C., Zhou, H., Liu, J., Xia, X., Ha, W., Jiang, Y., Liu, Q., & Xiong, H. (2024). Kinase inhibitors and kinase-targeted cancer therapies: recent advances and future perspectives. *International Journal of Molecular Sciences*, *25*(10), 5489.

Li, R., Zupanic, A., Talikka, M., Belcastro, V., Madan, S., Dörpinghaus, J., Berg, C. v., Szostak, J., Martin, F., & Peitsch, M. C. (2020). Systems toxicology approach for testing chemical cardiotoxicity in larval zebrafish. *Chemical research in toxicology*, *33*(10), 2550-2564.

Li, T., Yang, Z., Li, H., Zhu, J., Wang, Y., Tang, Q., & Shi, Z. (2022). Phospholipase Cγ1 (PLCG1) overexpression is associated with tumor growth and poor survival in IDH wild-type lower-grade gliomas in adult patients. *Laboratory Investigation*, *102*(2), 143-153.

Li, X., Chen, G., Liu, B., Tao, Z., Wu, Y., Zhang, K., Feng, Z., Huang, Y., & Wang, H. (2023). PLK1 inhibition promotes apoptosis and DNA damage in glioma stem cells by regulating the nuclear translocation of YBX1. *Cell Death Discovery*, *9*(1), 68.

Li, X., Wu, C., Chen, N., Gu, H., Yen, A., Cao, L., Wang, E., & Wang, L. (2016). PI3K/Akt/mTOR signaling pathway and targeted therapy for glioblastoma. *Oncotarget*, *7*(22), 33440.

Liau, L. M., Ashkan, K., Brem, S., Campian, J. L., Trusheim, J. E., Iwamoto, F. M., Tran, D. D., Ansstas, G., Cobbs, C. S., & Heth, J. A. (2023). Association of autologous tumor lysate-loaded dendritic cell vaccination with extension of survival among patients with newly diagnosed and recurrent glioblastoma: a phase 3 prospective externally controlled cohort trial. *JAMA oncology*, *9*(1), 112-121.

Lin, C., Garruss, A. S., Luo, Z., Guo, F., & Shilatifard, A. (2013). The RNA Pol II elongation factor Ell3 marks enhancers in ES cells and primes future gene activation. *Cell*, *152*(1), 144-156.

Lin, C., Su, W., Yen, C., Hsu, C., Su, W., Yeh, K., Lu, Y., Cheng, A., Huang, D. C., & Fritsch, H. (2014). A phase I study of two dosing schedules of volasertib (BI 6727), an intravenous polo-like kinase inhibitor, in patients with advanced solid malignancies. *British journal of cancer*, *110*(10), 2434-2440.

Lin, S.-F., Lin, J.-D., Yeh, C.-N., Huang, Y.-T., Chou, T.-C., & Wong, R. J. (2019). Targeting PLKs as a therapeutic approach to well-differentiated thyroid cancer. *Endocrine-related cancer*, *26*(8), 727-738.

Liu, H., Qiu, W., Sun, T., Wang, L., Du, C., Hu, Y., Liu, W., Feng, F., Chen, Y., & Sun, H. (2022). Therapeutic strategies of glioblastoma (GBM): The current advances in the molecular targets and bioactive small molecule compounds. *Acta Pharmaceutica Sinica B*, *12*(4), 1781-1804.

Liu, L., Cao, Y., Chen, C., Zhang, X., McNabola, A., Wilkie, D., Wilhelm, S., Lynch, M., & Carter, C. (2006). Sorafenib blocks the RAF/MEK/ERK pathway, inhibits tumor angiogenesis, and induces tumor cell apoptosis in hepatocellular carcinoma model PLC/PRF/5. *Cancer research*, *66*(24), 11851-11858.

Liu, Y., Zhou, F., Ali, H., Lathia, J. D., & Chen, P. (2024). Immunotherapy for glioblastoma: current state, challenges, and future perspectives. *Cellular & Molecular Immunology*, *21*(12), 1354-1375.

Lorenz, N. I., Sittig, A. C., Urban, H., Luger, A.-L., Engel, A. L., Münch, C., Steinbach, J. P., & Ronellenfitsch, M. W. (2021). Activating transcription factor 4 mediates adaptation of human glioblastoma cells to hypoxia and temozolomide. *Scientific reports*, *11*(1), 14161.

Louis, D. N., Perry, A., Reifenberger, G., Von Deimling, A., Figarella-Branger, D., Cavenee, W. K., Ohgaki, H., Wiestler, O. D., Kleihues, P., & Ellison, D. W. (2016). The 2016 World Health Organization classification of tumors of the central nervous system: a summary. *Acta neuropathologica*, *131*(6), 803-820.

Lu, Y., Wang, X., Gu, Q., Wang, J., Sui, Y., Wu, J., & Feng, J. (2022). Heterogeneous nuclear ribonucleoprotein A/B: an emerging group of cancer biomarkers and therapeutic targets. *Cell Death Discovery*, *8*(1), 337.

MacLeod, G., Molaei, F., Haider, S., Almeida, M. P., Lin, S., Kushida, M., Sureshkumar, H., Bhatti, J. K., Lu, J. Q., & Schramek, D. (2024). Fitness Screens Map State-Specific Glioblastoma Stem Cell Vulnerabilities. *Cancer research*, *84*(23), 3967-3983.

Manoharan, G. B., Okutachi, S., & Abankwa, D. (2022). Potential of phenothiazines to synergistically block calmodulin and reactivate PP2A in cancer cells. *PLoS One*, *17*(5), e0268635.

Manoharan, V. T., Abdelkareem, A., Gill, G., Brown, S., Gillmor, A., Hall, C., Seo, H., Narta, K., Grewal, S., & Dang, N. H. (2024). Spatiotemporal modeling reveals high-resolution invasion states in glioblastoma. *Genome Biology*, *25*(1), 264.

Martini, M., De Santis, M. C., Braccini, L., Gulluni, F., & Hirsch, E. (2014). PI3K/AKT signaling pathway and cancer: an updated review. *Annals of medicine*, *46*(6), 372-383.

Masci, D., Puxeddu, M., Silvestri, R., & La Regina, G. (2024). Metabolic rewiring in cancer: small molecule inhibitors in colorectal cancer therapy. *Molecules*, *29*(9), 2110.
Mashimo, T., Pichumani, K., Vemireddy, V., Hatanpaa, K. J., Singh, D. K., Sirasanagandla, S., Nannepaga, S., Piccirillo, S. G., Kovacs, Z., & Foong, C. (2014). Acetate is a bioenergetic substrate for human glioblastoma and brain metastases. *Cell*, *159*(7), 1603-1614.
Matarrese, P., Signore, M., Ascione, B., Fanelli, G., Paggi, M. G., & Abbruzzese, C. (2024). Chlorpromazine overcomes temozolomide resistance in glioblastoma by inhibiting Cx43 and essential DNA repair pathways. *Journal of Translational Medicine*, *22*(1), 667.
Mauch, D. H., Nagler, K., Schumacher, S., Göritz, C., Müller, E.-C., Otto, A., & Pfrieger, F. W. (2001). CNS synaptogenesis promoted by glia-derived cholesterol. *Science*, *294*(5545), 1354-1357.
Mazière, C., Mazière, J.-C., Mora, L., Auclair, M., & Polonovski, J. (1988). Trifluoperazine increases fatty acid turnover in phospholipids in cultured human fibroblasts. *Lipids*, *23*(5), 419-423.
Mehrabi, S. F., Elmi, S., & Nylandsted, J. (2023). Repurposing phenothiazines for cancer therapy: compromising membrane integrity in cancer cells. *Frontiers in Oncology*, *13*, 1320621.
Mendels, J., Krajewski, T. F., Huffer, V., Taylor, R. J., Secunda, S., Schless, A., Sebastian, J., Semchyshyn, G., Durr, M., & Melmed, A. (1986). Effective short-term treatment of generalized anxiety disorder with trifluoperazine. *The Journal of clinical psychiatry*, *47*(4), 170-174.
Méndez-Blanco, C., Fondevila, F., García-Palomo, A., González-Gallego, J., & Mauriz, J. L. (2018). Sorafenib resistance in hepatocarcinoma: role of hypoxia-inducible factors. *Experimental & Molecular Medicine*, *50*(10), 1-9.
Menzies, S. A., Volkmar, N., van den Boomen, D. J., Timms, R. T., Dickson, A. S., Nathan, J. A., & Lehner, P. J. (2018). The sterol-responsive RNF145 E3 ubiquitin ligase mediates the degradation of HMG-CoA reductase together with gp78 and Hrd1. *Elife*, *7*, e40009.
Milkereit, R., Persaud, A., Vanoaica, L., Guetg, A., Verrey, F., & Rotin, D. (2015). LAPTM4b recruits the LAT1-4F2hc Leu transporter to lysosomes and promotes mTORC1 activation. *Nature communications*, *6*(1), 7250.
Miller, T., Williams, K., Johnstone, R. W., & Shilatifard, A. (2000). Identification, cloning, expression, and biochemical characterization of the testis-specific RNA polymerase II elongation factor ELL3. *Journal of Biological Chemistry*, *275*(41), 32052-32056.
Miller, T. W., Balko, J. M., Fox, E. M., Ghazoui, Z., Dunbier, A., Anderson, H., Dowsett, M., Jiang, A., Smith, R. A., & Maira, S.-M. (2011). ERα-dependent E2F transcription can mediate resistance to estrogen deprivation in human breast cancer. *Cancer discovery*, *1*(4), 338-351.
Miyahara, S., Ohuchi, M., Nomura, M., Hashimoto, E., Soga, T., Saito, R., Hayashi, K., Sato, T., Saito, M., & Yamashita, Y. (2024). FDX2, an iron-sulfur cluster assembly factor, is essential to prevent cellular senescence, apoptosis or ferroptosis of ovarian cancer cells. *Journal of Biological Chemistry*, *300*(9).
Miziorko, H. M. (2011). Enzymes of the mevalonate pathway of isoprenoid biosynthesis. *Archives of biochemistry and biophysics*, *505*(2), 131-143.
Mo, H., Shao, J., Li, Z., Zeng, P., Yin, X., Huang, Y., Wang, P., & Liao, J. (2024). FDFT1 maintains glioblastoma stem cells through activation of the Akt pathway. *Stem Cell Research & Therapy*, *15*(1), 492.
Modarresi Chahardehi, A., Arsad, H., & Lim, V. (2020). Zebrafish as a successful animal model for screening toxicity of medicinal plants. *Plants*, *9*(10), 1345.
Mok, E. H. K., & Lee, T. K. W. (2020). The pivotal role of the dysregulation of cholesterol homeostasis in cancer: implications for therapeutic targets. *Cancers*, *12*(6), 1410.
Moraes, V. W., Santos, V. M., Suarez, E. R., Ferraz, L. S., Lopes, R. d. M., Mognol, G. P., Campeiro, J. D., Machado-Neto, J. A., Nascimento, F. D., & Hayashi, M. A. (2022). Targeting Ca2+ and mitochondrial homeostasis by antipsychotic thioridazine in leukemia cells. *Life*, *12*(10), 1477.
Mu, Y., Li, X.-q., Zhang, B., & Du, J.-l. (2012). Visual input modulates audiomotor function via hypothalamic dopaminergic neurons through a cooperative mechanism. *Neuron*, *75*(4), 688-699.
Ng, M. Y., Wang, H., Zhang, H., Prucker, I., Perera, L., Goncharova, E., Wamiru, A., Jessen, H. J., Stanley, R. E., & Shears, S. B. (2025). Biochemical and biophysical characterization of

inositol-tetrakisphosphate 1-kinase inhibitors. *Journal of Biological Chemistry*, *301*(3), 108274.
Noack, S., Raab, M., Matthess, Y., Sanhaji, M., Krämer, A., Győrffy, B., Kaderali, L., El-Balat, A., Becker, S., & Strebhardt, K. (2018). Synthetic lethality in CCNE1-amplified high grade serous ovarian cancer through combined inhibition of Polo-like kinase 1 and microtubule dynamics. *Oncotarget*, *9*(40), 25842.
O'Day, D. H. (2022). Calmodulin binding domains in critical risk proteins involved in neurodegeneration. *Current Issues in Molecular Biology*, *44*(11), 5802-5814.
Okada, M., Nakagawa-Saito, Y., Mitobe, Y., Sugai, A., Togashi, K., Suzuki, S., & Kitanaka, C. (2022). Inhibition of the Phospholipase Cε–c-Jun N-Terminal Kinase Axis Suppresses Glioma Stem Cell Properties. *International Journal of Molecular Sciences*, *23*(15), 8785.
Ozawa, T., Rodriguez, M., Zhao, G., Yao, T. W., Fischer, W.-N., Jandeleit, B., Koller, K., Nicolaides, T., Jandeleit, B. G., & Koller, K. J. (2021). A novel blood-brain barrier-permeable chemotherapeutic agent for the treatment of glioblastoma. *Cureus*, *13*(8).
Ozeki, Y., Pickard, B. S., Kano, S.-i., Malloy, M. P., Zeledon, M., Sun, D. Q., Fujii, K., Wakui, K., Shirayama, Y., & Fukushima, Y. (2011). A novel balanced chromosomal translocation found in subjects with schizophrenia and schizotypal personality disorder: altered l-serine level associated with disruption of PSAT1 gene expression. *Neuroscience research*, *69*(2), 154-160.
Pakos-Zebrucka, K., Koryga, I., Mnich, K., Ljujic, M., Samali, A., & Gorman, A. M. (2016). The integrated stress response. *EMBO reports*, *17*(10), 1374-1395.
Panopoulos, A. D., Yanes, O., Ruiz, S., Kida, Y. S., Diep, D., Tautenhahn, R., Herrerías, A., Batchelder, E. M., Plongthongkum, N., & Lutz, M. (2012). The metabolome of induced pluripotent stem cells reveals metabolic changes occurring in somatic cell reprogramming. *Cell research*, *22*(1), 168-177.
Panwar, V., Singh, A., Bhatt, M., Tonk, R. K., Azizov, S., Raza, A. S., Sengupta, S., Kumar, D., & Garg, M. (2023). Multifaceted role of mTOR (mammalian target of rapamycin) signaling pathway in human health and disease. *Signal Transduction and Targeted Therapy*, *8*(1), 375.
Park, J., Jeong, J. Y., & Kang, S. S. (2022). COX-2 acts as a key mediator of trifluoperazine-induced cell death in U87MG glioma cells. *Anticancer research*, *42*(12), 5773-5781.
Patton, E. E., Zon, L. I., & Langenau, D. M. (2021). Zebrafish disease models in drug discovery: from preclinical modelling to clinical trials. *Nature Reviews Drug Discovery*, *20*(8), 611-628.
Pearson, J. R., & Regad, T. (2017). Targeting cellular pathways in glioblastoma multiforme. *Signal Transduction and Targeted Therapy*, *2*(1), 1-11.
Peng, X., Lin, J., Zhu, Y., Liu, X., Zhang, Y., Ji, Y., Yang, X., Zhang, Y., Guo, N., & Li, Q. (2016). Anxiety-related behavioral responses of pentylenetetrazole-treated zebrafish larvae to light-dark transitions. *Pharmacology Biochemistry and Behavior*, *145*, 55-65.
Persson, A. I., Petritsch, C., Swartling, F. J., Itsara, M., Sim, F. J., Auvergne, R., Goldenberg, D. D., Vandenberg, S. R., Nguyen, K. N., & Yakovenko, S. (2010). Non-stem cell origin for oligodendroglioma. *Cancer cell*, *18*(6), 669-682.
Petersen, B. D., Bertoncello, K. T., & Bonan, C. D. (2022). Standardizing zebrafish behavioral paradigms across life stages: an effort towards translational pharmacology. *Frontiers in Pharmacology*, *13*, 833227.
Pillai, V., Pracucci, E., Trovato, F., Parra, R., Landi, S., & Ratto, G. M. (2025). Heterogeneity of intracellular calcium signaling of glioblastoma cells depends on intratumoral location and migration state. *Neuro-Oncology Advances*, *7*(1), vdaf055.
Platzbecker, U., Chromik, J., Krönke, J., Handa, H., Strickland, S., Miyazaki, Y., Wermke, M., Sakamoto, W., Tachibana, Y., & Taube, T. (2022). Volasertib as a monotherapy or in combination with azacitidine in patients with myelodysplastic syndrome, chronic myelomonocytic leukemia, or acute myeloid leukemia: summary of three phase I studies. *BMC cancer*, *22*(1), 569.
Porter, J. R., Fisher, B. E., Baranello, L., Liu, J. C., Kambach, D. M., Nie, Z., Koh, W. S., Luo, J., Stommel, J. M., & Levens, D. (2017). Global inhibition with specific activation: how p53 and MYC redistribute the transcriptome in the DNA double-strand break response. *Molecular cell*, *67*(6), 1013-1025. e1019.

Portugues, R., & Engert, F. (2011). Adaptive locomotor behavior in larval zebrafish. *Frontiers in systems neuroscience*, *5*, 72.

Pouyan, A., Ghorbanlo, M., Eslami, M., Jahanshahi, M., Ziaei, E., Salami, A., Mokhtari, K., Shahpasand, K., Farahani, N., & Meybodi, T. E. (2025). Glioblastoma multiforme: insights into pathogenesis, key signaling pathways, and therapeutic strategies. *Molecular cancer*, *24*(1), 58.

Prolo, L. M., Li, A., Owen, S. F., Parker, J. J., Foshay, K., Nitta, R. T., Morgens, D. W., Bolin, S., Wilson, C. M., & Vega L, J. C. (2019). Targeted genomic CRISPR-Cas9 screen identifies MAP4K4 as essential for glioblastoma invasion. *Scientific reports*, *9*(1), 14020.

Qannita, R. A., Alalami, A. I., Harb, A. A., Aleidi, S. M., Taneera, J., Abu-Gharbieh, E., El-Huneidi, W., Saleh, M. A., Alzoubi, K. H., & Semreen, M. H. (2024). Targeting hypoxia-inducible factor-1 (HIF-1) in cancer: emerging therapeutic strategies and pathway regulation. *Pharmaceuticals*, *17*(2), 195.

Qian, L., Chai, A. B., Gelissen, I. C., & Brown, A. J. (2022). Balancing cholesterol in the brain: From synthesis to disposal. *Exploration of Neuroprotective Therapy*, *2*(1), 1-27.

Qiu, R., Zhong, Y., Li, Q., Li, Y., & Fan, H. (2021). Metabolic remodeling in glioma immune microenvironment: intercellular interactions distinct from peripheral tumors. *Frontiers in Cell and Developmental Biology*, *9*, 693215.

Rahman, R., Trippa, L., Lee, E. Q., Arrillaga-Romany, I., Fell, G., Touat, M., McCluskey, C., Wiley, J., Gaffey, S., & Drappatz, J. (2023). Inaugural results of the individualized screening trial of innovative glioblastoma therapy: a phase II platform trial for newly diagnosed glioblastoma using Bayesian adaptive randomization. *Journal of Clinical Oncology*, *41*(36), 5524-5535.

Raizer, J., Abrey, L., & Wen, P. (2004). A Phase II trial of OSI-774 (Tarceva) in patients (pts) with recurrent malignant gliomas (MG) not on EIAEDs. Proc. Am. Soc. Clin. Oncol,

Read, E., & Hindges, R. (2024). A novel locomotion-based prepulse inhibition assay in zebrafish larvae. *microPublication Biology*, *2024*, 10.17912/micropub. biology. 000914.

Ren, J., Da, J., & Hu, N. (2022). Identification of COL1A1 associated with immune infiltration in brain lower grade glioma. *PLoS One*, *17*(7), e0269533.

Richbart, S. D., Merritt, J. C., Nolan, N. A., & Dasgupta, P. (2021). Acetylcholinesterase and human cancers. *Advances in Cancer Research*, *152*, 1-66.

Ricklefs, F. L., Maire, C. L., Matschke, J., Dührsen, L., Sauvigny, T., Holz, M., Kolbe, K., Peine, S., Herold-Mende, C., & Carter, B. (2020). FASN is a biomarker enriched in malignant glioma-derived extracellular vesicles. *International Journal of Molecular Sciences*, *21*(6), 1931.

Rodriguez, S. M. B., Kamel, A., Ciubotaru, G. V., Onose, G., Sevastre, A.-S., Sfredel, V., Danoiu, S., Dricu, A., & Tataranu, L. G. (2023). An overview of EGFR mechanisms and their implications in targeted therapies for glioblastoma. *International Journal of Molecular Sciences*, *24*(13), 11110.

Rokhlin, O. W., Glover, R. A., Taghiyev, A. F., Guseva, N. V., Seftor, R. E., Shyshynova, I., Gudkov, A. V., & Cohen, M. B. (2002). Bisindolylmaleimide IX facilitates tumor necrosis factor receptor family-mediated cell death and acts as an inhibitor of transcription. *Journal of Biological Chemistry*, *277*(36), 33213-33219.

Ronnen, R., Wang, S., Haddock, S., Ravn-Boess, N., Golub, D., Stephan, G., Sabio, J., Donaldson, H., Bonanni, L., & Zuniga, A. G. (2024). CSIG-22. PHARMACOLOGIC INHIBITION AND KNOCKDOWN OF CAMK2 IMPAIR GROWTH OF PATIENT-DERIVED GLIOBLASTOMA CULTURES. *Neuro-Oncology*, *26*(Supplement_8), viii68-viii68.

Rutkowski, D. T., Arnold, S. M., Miller, C. N., Wu, J., Li, J., Gunnison, K. M., Mori, K., Sadighi Akha, A. A., Raden, D., & Kaufman, R. J. (2006). Adaptation to ER stress is mediated by differential stabilities of pro-survival and pro-apoptotic mRNAs and proteins. *PLoS biology*, *4*(11), e374.

Sakai, C., Ijaz, S., & Hoffman, E. J. (2018). Zebrafish models of neurodevelopmental disorders: past, present, and future. *Frontiers in molecular neuroscience*, *11*, 294.

Salbini, M., Formato, A., Mongiardi, M. P., Levi, A., & Falchetti, M. L. (2025). Kinase-Targeted Therapies for Glioblastoma. *International Journal of Molecular Sciences*, *26*(8), 3737.

Saxton, R. A., & Sabatini, D. M. (2017). mTOR signaling in growth, metabolism, and disease. *Cell*, *168*(6), 960-976.

Sazonova, E. V., Petrichuk, S. V., Kopeina, G. S., & Zhivotovsky, B. (2021). A link between mitotic defects and mitotic catastrophe: detection and cell fate. *Biology Direct*, *16*(1), 25.
Schöffski, P., Awada, A., Dumez, H., Gil, T., Bartholomeus, S., Wolter, P., Taton, M., Fritsch, H., Glomb, P., & Munzert, G. (2012). A phase I, dose-escalation study of the novel Polo-like kinase inhibitor volasertib (BI 6727) in patients with advanced solid tumours. *European journal of cancer*, *48*(2), 179-186.
Schulz, J. A., Rodgers, L. T., Kryscio, R. J., Hartz, A. M., & Bauer, B. (2022). Characterization and comparison of human glioblastoma models. *BMC cancer*, *22*(1), 844.
Schwerk, C., & Schulze-Osthoff, K. (2005). Regulation of apoptosis by alternative pre-mRNA splicing. *Molecular cell*, *19*(1), 1-13.
Shaikat, A. H., Azad, S. A. K., Tamim, M. A. R., Ullah, M. S., Amin, M. N., Sabbir, M. K., Tarun, M. T. I., Mostaq, M. S., Sabrin, S., & Mahmud, M. Z. (2025). Investigating hypoxia-inducible factor signaling in cancer: mechanisms, clinical implications, targeted therapeutic strategies, and resistance. *Cancer Pathogenesis and Therapy*.
Shen, J., Ma, B., Zhang, X., Sun, X., Han, J., Wang, Y., Chu, L., Xu, H., & Yang, Y. (2017). Thioridazine has potent antitumor effects on lung cancer stem-like cells. *Oncology letters*, *13*(3), 1563-1568.
Shen, L., Shen, H., Wang, T., Chen, G., Yu, Z., & Liu, F. (2025). Analysis of ABCC3 in glioma progression: implications for prognosis, immunotherapy, and drug resistance. *Discover Oncology*, *16*(1), 179.
Shen, W. W. (1999). A history of antipsychotic drug development. *Comprehensive psychiatry*, *40*(6), 407-414.
Shi, F., Zhang, J., Liu, H., Wu, L., Jiang, H., Wu, Q., Liu, T., Lou, M., & Wu, H. (2017). The dual PI3K/mTOR inhibitor dactolisib elicits anti-tumor activity in vitro and in vivo. *Oncotarget*, *9*(1), 706.
Shimada, K., Bachman, J. A., Muhlich, J. L., & Mitchison, T. J. (2021). shinyDepMap, a tool to identify targetable cancer genes and their functional connections from Cancer Dependency Map data. *Elife*, *10*, e57116.
Shu, L., Wang, D., Saba, N. F., & Chen, Z. G. (2020). A historic perspective and overview of H-Ras structure, oncogenicity, and targeting. *Molecular cancer therapeutics*, *19*(4), 999-1007.
Siegelin, M. D., Raskett, C. M., Gilbert, C. A., Ross, A. H., & Altieri, D. C. (2010). Sorafenib exerts anti-glioma activity in vitro and in vivo. *Neuroscience letters*, *478*(3), 165-170.
Silva, R., Vilas-Boas, V., Carmo, H., Dinis-Oliveira, R. J., Carvalho, F., de Lourdes Bastos, M., & Remiao, F. (2015). Modulation of P-glycoprotein efflux pump: induction and activation as a therapeutic strategy. *Pharmacology & therapeutics*, *149*, 1-123.
Simbilyabo, L. Z., Yang, L., Wen, J., & Liu, Z. (2024). The unfolded protein response machinery in glioblastoma genesis, chemoresistance and as a druggable target. *CNS Neuroscience & Therapeutics*, *30*(7), e14839.
Singh, S., Barik, D., Lawrie, K., Mohapatra, I., Prasad, S., Naqvi, A. R., Singh, A., & Singh, G. (2023). Unveiling novel avenues in mTOR-targeted therapeutics: advancements in glioblastoma treatment. *International Journal of Molecular Sciences*, *24*(19), 14960.
Singh, S. K., Clarke, I. D., Terasaki, M., Bonn, V. E., Hawkins, C., Squire, J., & Dirks, P. B. (2003). Identification of a cancer stem cell in human brain tumors. *Cancer research*, *63*(18), 5821-5828.
So, J.-S., Kim, H., & Han, K.-S. (2021). Mechanisms of invasion in glioblastoma: extracellular matrix, Ca2+ signaling, and glutamate. *Frontiers in cellular neuroscience*, *15*, 663092.
Song, A., Andrews, D. W., Werner-Wasik, M., Kim, L., Glass, J., Bar-Ad, V., Evans, J. J., Farrell, C. J., Judy, K. D., & Daskalakis, C. (2019). Phase I trial of alisertib with concurrent fractionated stereotactic re-irradiation for recurrent high grade gliomas. *Radiotherapy and Oncology*, *132*, 135-141.
Soria-Valles, C., Osorio, F. G., Gutiérrez-Fernández, A., De Los Angeles, A., Bueno, C., Menéndez, P., Martín-Subero, J. I., Daley, G. Q., Freije, J. M., & López-Otín, C. (2015). NF-κB activation impairs somatic cell reprogramming in ageing. *Nature cell biology*, *17*(8), 1004-1013.

Stateva, S. R., Salas, V., Anguita, E., Benaim, G., & Villalobo, A. (2015). Ca2+/calmodulin and apo-calmodulin both bind to and enhance the tyrosine kinase activity of c-Src. *PLoS One*, *10*(6), e0128783.

Stringer, B. W., De Silva, M. I., Greenberg, Z., Noreña Puerta, A., Adams, R., Milky, B., Zabolocki, M., van den Hurk, M., Ebert, L. M., & Fairly Bishop, C. (2023). Human cerebrospinal fluid affects chemoradiotherapy sensitivities in tumor cells from patients with glioblastoma. *Science Advances*, *9*(43), eadf1332.

Stupp, R., Mason, W. P., Van Den Bent, M. J., Weller, M., Fisher, B., Taphoorn, M. J., Belanger, K., Brandes, A. A., Marosi, C., & Bogdahn, U. (2005). Radiotherapy plus concomitant and adjuvant temozolomide for glioblastoma. *New England journal of medicine*, *352*(10), 987-996.

Su, S., Chhabra, G., Singh, C. K., Ndiaye, M. A., & Ahmad, N. (2022). PLK1 inhibition-based combination therapies for cancer management. *Translational oncology*, *16*, 101332.

Sun, Q., Liu, D., Cui, W., Cheng, H., Huang, L., Zhang, R., Gu, J., Liu, S., Zhuang, X., & Lu, Y. (2023). Cholesterol mediated ferroptosis suppression reveals essential roles of Coenzyme Q and squalene. *Communications Biology*, *6*(1), 1108.

Sun, S., Wang, Y., Wu, Y., Gao, Y., Li, Q., Abdulrahman, A. A., Liu, X. F., Ji, G. Q., Gao, J., & Li, L. (2018). Identification of COL1A1 as an invasion-related gene in malignant astrocytoma. *International journal of oncology*, *53*(6), 2542-2554.

Sun, S., Xue, D., Chen, Z., Ou-Yang, Y., Zhang, J., Mai, J., Gu, J., Lu, W., Liu, X., & Liu, W. (2019). R406 elicits anti-Warburg effect via Syk-dependent and-independent mechanisms to trigger apoptosis in glioma stem cells. *Cell death & disease*, *10*(5), 358.

Tal, T., Yaghoobi, B., & Lein, P. J. (2020). Translational toxicology in zebrafish. *Current opinion in toxicology*, *23*, 56-66.

Tan, A. C., Ashley, D. M., López, G. Y., Malinzak, M., Friedman, H. S., & Khasraw, M. (2020). Management of glioblastoma: State of the art and future directions. *CA: a cancer journal for clinicians*, *70*(4), 299-312.

Tanaka, K., Sasayama, T., Nagashima, H., Irino, Y., Takahashi, M., Izumi, Y., Uno, T., Satoh, N., Kitta, A., & Kyotani, K. (2021). Glioma cells require one-carbon metabolism to survive glutamine starvation. *Acta neuropathologica communications*, *9*(1), 16.

Tang, Y., Dai, Y., Grant, S., & Dent, P. (2012). Enhancing CHK1 inhibitor lethality in glioblastoma. *Cancer biology & therapy*, *13*(6), 379-388.

Targen, S., Kaya, T., Avci, M. E., Gunes, D., Keskus, A. G., & Konu, O. (2020). ZenoFishDb v1. 1: a database for xenotransplantation studies in zebrafish. *Zebrafish*, *17*(5), 305-318.

Taylor, J. W., Parikh, M., Phillips, J. J., James, C. D., Molinaro, A. M., Butowski, N. A., Clarke, J. L., Oberheim-Bush, N. A., Chang, S. M., & Berger, M. S. (2018). Phase-2 trial of palbociclib in adult patients with recurrent RB1-positive glioblastoma. *Journal of Neuro-Oncology*, *140*(2), 477-483.

Teicher, G., Riffe, R. M., Barnaby, W., Martin, G., Clayton, B. E., Trapani, J. G., & Downes, G. B. (2025). Marigold: a machine learning-based web app for zebrafish pose tracking. *BMC bioinformatics*, *26*(1), 30.

Thakkar, J. P., Dolecek, T. A., Horbinski, C., Ostrom, Q. T., Lightner, D. D., Barnholtz-Sloan, J. S., & Villano, J. L. (2014). Epidemiologic and molecular prognostic review of glioblastoma. *Cancer epidemiology, biomarkers & prevention*, *23*(10), 1985-1996.

Tilak, M., Holborn, J., New, L. A., Lalonde, J., & Jones, N. (2021). Receptor tyrosine kinase signaling and targeting in glioblastoma multiforme. *International Journal of Molecular Sciences*, *22*(4), 1831.

Tomuleasa, C., Tigu, A.-B., Munteanu, R., Moldovan, C.-S., Kegyes, D., Onaciu, A., Gulei, D., Ghiaur, G., Einsele, H., & Croce, C. M. (2024). Therapeutic advances of targeting receptor tyrosine kinases in cancer. *Signal Transduction and Targeted Therapy*, *9*(1), 201.

Torp, S. H., Solheim, O., & Skjulsvik, A. J. (2022). The WHO 2021 Classification of Central Nervous System tumours: a practical update on what neurosurgeons need to know—a minireview. *Acta neurochirurgica*, *164*(9), 2453-2464.

Trejo-Solís, C., Castillo-Rodríguez, R. A., Serrano-García, N., Silva-Adaya, D., Vargas-Cruz, S., Chávez-Cortéz, E. G., Gallardo-Pérez, J. C., Zavala-Vega, S., Cruz-Salgado, A., & Magaña-

Maldonado, R. (2024). Metabolic roles of HIF1, c-Myc, and p53 in glioma cells. *Metabolites*, *14*(5), 249.

Tsai, S.-C., Chang, P.-C., Lin, Y. T., Huang, P.-T., Chen, J. Y.-F., Lin, C. S., Wu, B.-N., Chang, H.-M., Wu, W.-J., & Chang, C.-I. (2024). Repurposing of the Antipsychotic Trifluoperazine Induces SLC7A11/GPX4-Mediated Ferroptosis of Oral Cancer via the ROS/Autophagy Pathway. *International Journal of Biological Sciences*, *20*(15), 6090.

Tuz-Sasik, M. U., Boije, H., & Manuel, R. (2022). Characterization of locomotor phenotypes in zebrafish larvae requires testing under both light and dark conditions. *PLoS One*, *17*(4), e0266491.

Van Linde, M. E., Labots, M., Brahm, C. G., Hovinga, K. E., De Witt Hamer, P. C., Honeywell, R. J., De Goeij-De Haas, R., Henneman, A. A., Knol, J. C., & Peters, G. J. (2022). Tumor drug concentration and phosphoproteomic profiles after two weeks of treatment with sunitinib in patients with newly diagnosed glioblastoma. *Clinical Cancer Research*, *28*(8), 1595-1602.

Vandonselaar, M., Hickie, R. A., Quail, W., & Delbaere, L. T. (1994). Trifluoperazine-induced conformational change in Ca2+-calmodulin. *Nature structural biology*, *1*(11), 795-801.

Varghese, R. T., Liang, Y., Guan, T., Franck, C. T., Kelly, D. F., & Sheng, Z. (2016). Survival kinase genes present prognostic significance in glioblastoma. *Oncotarget*, *7*(15), 20140.

Varn, F. S., Johnson, K. C., Martinek, J., Huse, J. T., Nasrallah, M. P., Wesseling, P., Cooper, L. A., Malta, T. M., Wade, T. E., & Sabedot, T. S. (2022). Glioma progression is shaped by genetic evolution and microenvironment interactions. *Cell*, *185*(12), 2184-2199. e2116.

Venkataramani, V., Yang, Y., Schubert, M. C., Reyhan, E., Tetzlaff, S. K., Wißmann, N., Botz, M., Soyka, S. J., Beretta, C. A., & Pramatarov, R. L. (2022). Glioblastoma hijacks neuronal mechanisms for brain invasion. *Cell*, *185*(16), 2899-2917. e2831.

Villa, G. R., Hulce, J. J., Zanca, C., Bi, J., Ikegami, S., Cahill, G. L., Gu, Y., Lum, K. M., Masui, K., & Yang, H. (2016). An LXR-cholesterol axis creates a metabolic co-dependency for brain cancers. *Cancer cell*, *30*(5), 683-693.

Vinik, Y., Maimon, A., & Lev, S. (2025). Protocol for predicting suppressors of cell-death pathways based on transcriptomic and vulnerability data. *STAR protocols*, *6*(2), 103855.

Visa, A., Sallán, M. C., Maiques, O., Alza, L., Talavera, E., López-Ortega, R., Santacana, M., Herreros, J., & Cantí, C. (2019). T-type Cav3. 1 channels mediate progression and chemotherapeutic resistance in glioblastoma. *Cancer research*, *79*(8), 1857-1868.

Vivona, S., Cipriano, D. J., O'Leary, S., Li, Y. H., Fenn, T. D., & Brunger, A. T. (2013). Disassembly of all SNARE complexes by N-ethylmaleimide-sensitive factor (NSF) is initiated by a conserved 1: 1 interaction between α-soluble NSF attachment protein (SNAP) and SNARE complex. *Journal of Biological Chemistry*, *288*(34), 24984-24991.

Walker, K., Boyd, N. H., Anderson, J. C., Willey, C. D., & Hjelmeland, A. B. (2018). Kinomic profiling of glioblastoma cells reveals PLCG1 as a target in restricted glucose. *Biomarker Research*, *6*(1), 22.

Wan, S., Jiang, J., Zheng, C., Wang, N., Zhai, X., Fei, X., Wu, R., & Jiang, X. (2018). Estrogen nuclear receptors affect cell migration by altering sublocalization of AQP2 in glioma cell lines. *Cell Death Discovery*, *4*(1), 49.

Wang, B., Varela-Eirin, M., Brandenburg, S. M., Hernandez-Segura, A., van Vliet, T., Jongbloed, E. M., Wilting, S. M., Ohtani, N., Jager, A., & Demaria, M. (2022). Pharmacological CDK4/6 inhibition reveals a p53-dependent senescent state with restricted toxicity. *The EMBO journal*, *41*(6), e108946.

Wang, H., Yin, J., Hong, Y., Ren, A., Wang, H., Li, M., Zhao, Q., Jiang, C., & Liu, L. (2022). SCG2 is a prognostic biomarker associated with immune infiltration and macrophage polarization in colorectal cancer. *Frontiers in Cell and Developmental Biology*, *9*, 795133.

Wang, J., & Matosevic, S. (2019). NT5E/CD73 as correlative factor of patient survival and natural killer cell infiltration in glioblastoma. *Journal of clinical medicine*, *8*(10), 1526.

Wang, L., Lankhorst, L., & Bernards, R. (2022). Exploiting senescence for the treatment of cancer. *Nature Reviews Cancer*, *22*(6), 340-355.

Wang, L., Zhang, Z., Zhong, Y., Ma, Z., & Kang, H. (2024). 488P ITGA2 promotes glioma cell stemness and progression by activating the AKT pathway. *Annals of Oncology*, *35*, S422-S423.

Wang, M., Jia, J., Cui, Y., Peng, Y., & Jiang, Y. (2021). CD73-positive extracellular vesicles promote glioblastoma immunosuppression by inhibiting T-cell clonal expansion. *Cell death & disease*, *12*(11), 1065.

Wang, S., Gu, S., Chen, J., Yuan, Z., Liang, P., & Cui, H. (2024). Mechanism of notch signaling pathway in malignant progression of glioblastoma and targeted therapy. *Biomolecules*, *14*(4), 480.

Wang, X., Chen, J., Liu, X.-h., Zeng, X.-y., Long, Q.-y., Liu, Y.-h., & Mao, Q. (2022). Evaluation of CD98 light chain-LAT1 as a potential marker of cancer stem-like cells in glioblastoma. *Biochimica et Biophysica Acta (BBA)-Molecular Cell Research*, *1869*(9), 119303.

Waqar, M., Trifiletti, D. M., McBain, C., O'connor, J., Coope, D. J., Akkari, L., Quinones-Hinojosa, A., & Borst, G. R. (2022). Early therapeutic interventions for newly diagnosed glioblastoma: rationale and review of the literature. *Current oncology reports*, *24*(3), 311-324.

Wei, J.-c., Meng, F.-d., Qu, K., Wang, Z.-x., Wu, Q.-f., Zhang, L.-q., Pang, Q., & Liu, C. (2015). Sorafenib inhibits proliferation and invasion of human hepatocellular carcinoma cells via up-regulation of p53 and suppressing FoxM1. *Acta pharmacologica sinica*, *36*(2), 241-251.

Welker, A. M., Jaros, B. D., Puduvalli, V. K., Imitola, J., Kaur, B., & Beattie, C. E. (2016). Standardized orthotopic xenografts in zebrafish reveal glioma cell-line-specific characteristics and tumor cell heterogeneity. *Disease models & mechanisms*, *9*(2), 199-210.

Weller, M., van den Bent, M., Preusser, M., Le Rhun, E., Tonn, J. C., Minniti, G., Bendszus, M., Balana, C., Chinot, O., & Dirven, L. (2021). EANO guidelines on the diagnosis and treatment of diffuse gliomas of adulthood. *Nature reviews Clinical oncology*, *18*(3), 170-186.

Wen, P. Y., & Kesari, S. (2008). Malignant gliomas in adults. *New England journal of medicine*, *359*(5), 492-507.

Whyte-Fagundes, P., Efromson, J., Vance, A., Carpenter, S., Bègue, A., Carroll, A., Doman, T. J. J., Harfouche, M., & Baraban, S. C. (2025). Automated detection of complex zebrafish seizure behavior at scale. *Communications Biology*, *8*(1), 872.

Wilhelm, S. M., Adnane, L., Newell, P., Villanueva, A., Llovet, J. M., & Lynch, M. (2008). Preclinical overview of sorafenib, a multikinase inhibitor that targets both Raf and VEGF and PDGF receptor tyrosine kinase signaling. *Molecular cancer therapeutics*, *7*(10), 3129-3140.

Winkler, J., Abisoye-Ogunniyan, A., Metcalf, K. J., & Werb, Z. (2020). Concepts of extracellular matrix remodelling in tumour progression and metastasis. *Nature communications*, *11*(1), 5120.

Xia, Y., Jia, C., Xue, Q., Jiang, J., Xie, Y., Wang, R., Ran, Z., Xu, F., Zhang, Y., & Ye, T. (2019). Antipsychotic drug trifluoperazine suppresses colorectal cancer by inducing G0/G1 arrest and apoptosis. *Frontiers in Pharmacology*, *10*, 1029.

Xie, F.-F., Pan, S.-S., Ou, R.-Y., Zheng, Z.-Z., Huang, X.-X., Jian, M.-T., Qiu, J.-G., Zhang, W.-J., Jiang, Q.-W., & Yang, Y. (2015). Volasertib suppresses tumor growth and potentiates the activity of cisplatin in cervical cancer. *American journal of cancer research*, *5*(12), 3548.

Yang, K., Wu, B., Zhang, Z., Peng, G., Huang, J., Hong, X., Ding, Q., Shi, L., Wang, X., & Zhao, H. (2023). Anlotinib for patients with newly diagnosed glioblastoma with unmethylated MGMT promoter: An open-label, single-center, phase 2 clinical trial. In: American Society of Clinical Oncology.

Yang, Q., Wang, Y., Pan, X., Ye, J., Gan, S., Qu, F., Chen, L., Chu, C., Gao, Y., & Cui, X. (2017). Frizzled 8 promotes the cell proliferation and metastasis of renal cell carcinoma. *Oncotarget*, *8*(45), 78989.

Yasumoto, Y., Miyazaki, H., Vaidyan, L. K., Kagawa, Y., Ebrahimi, M., Yamamoto, Y., Ogata, M., Katsuyama, Y., Sadahiro, H., & Suzuki, M. (2016). Inhibition of fatty acid synthase decreases expression of stemness markers in glioma stem cells. *PLoS One*, *11*(1), e0147717.

Yeh, C.-T., Wu, A. T., Chang, P. M.-H., Chen, K.-Y., Yang, C.-N., Yang, S.-C., Ho, C.-C., Chen, C.-C., Kuo, Y.-L., & Lee, P.-Y. (2012). Trifluoperazine, an antipsychotic agent, inhibits cancer stem cell growth and overcomes drug resistance of lung cancer. *American journal of respiratory and critical care medicine*, *186*(11), 1180-1188.

Zakaria, Z. Z., Benslimane, F. M., Nasrallah, G. K., Shurbaji, S., Younes, N. N., Mraiche, F., Da'as, S. I., & Yalcin, H. C. (2018). Using zebrafish for investigating the molecular mechanisms of drug-induced cardiotoxicity. *BioMed research international*, *2018*(1), 1642684.

Zeng, A., Ye, T., Cao, D., Huang, X., Yang, Y., Chen, X., Xie, Y., Yao, S., & Zhao, C. (2017). Identify a blood-brain barrier penetrating drug-TNB using zebrafish orthotopic glioblastoma xenograft model. *Scientific reports*, *7*(1), 14372.

Zeng, X., Chen, W., Yu, N., Li, Z., Li, H., Chen, Y., Gong, F., Jiang, X., & Ji, G. (2024). Trifluoperazine exerts anti-osteosarcoma effect by inducing mitochondria-dependent apoptosis via AKT/TXNIP signaling pathway. *Toxicology and Applied Pharmacology*, *492*, 117080.

Zhai, J., Wu, J., Wang, Y., Fan, R., Xie, G., Wu, F., He, Y., Qian, S., Tan, A., & Yao, X. (2021). Prediction of sensitivity and efficacy of clinical chemotherapy using larval zebrafish patient-derived xenografts of gastric cancer. *Frontiers in Cell and Developmental Biology*, *9*, 680491.

Zhang, J., Li, R., Zhang, H., Wang, S., & Zhao, Y. (2024). ITGA2 as a prognostic factor of glioma promotes GSCs invasion and EMT by activating STAT3 phosphorylation. *Carcinogenesis*, *45*(4), 235-246.

Zhang, X., Xu, R., Zhang, C., Xu, Y., Han, M., Huang, B., Chen, A., Qiu, C., Thorsen, F., & Prestegarden, L. (2017). Trifluoperazine, a novel autophagy inhibitor, increases radiosensitivity in glioblastoma by impairing homologous recombination. *Journal of Experimental & Clinical Cancer Research*, *36*(1), 118.

Zhao, H.-f., Wang, J., Shao, W., Wu, C.-p., Chen, Z.-p., To, S.-s. T., & Li, W.-p. (2017). Recent advances in the use of PI3K inhibitors for glioblastoma multiforme: current preclinical and clinical development. *Molecular cancer*, *16*(1), 100.

Zhao, S., Huang, J., & Ye, J. (2015). A fresh look at zebrafish from the perspective of cancer research. *Journal of Experimental & Clinical Cancer Research*, *34*(1), 80.

Zheng, J., Sato, M., Mishima, E., Sato, H., Proneth, B., & Conrad, M. (2021). Sorafenib fails to trigger ferroptosis across a wide range of cancer cell lines. *Cell death & disease*, *12*(7), 698.

Zottel, A., Novak, M., Šamec, N., Majc, B., Colja, S., Katrašnik, M., Vittori, M., Hrastar, B., Rotter, A., & Porčnik, A. (2023). Anti-vimentin nanobody decreases glioblastoma cell invasion in vitro and in vivo. *Cancers*, *15*(3), 573.

APPENDIX

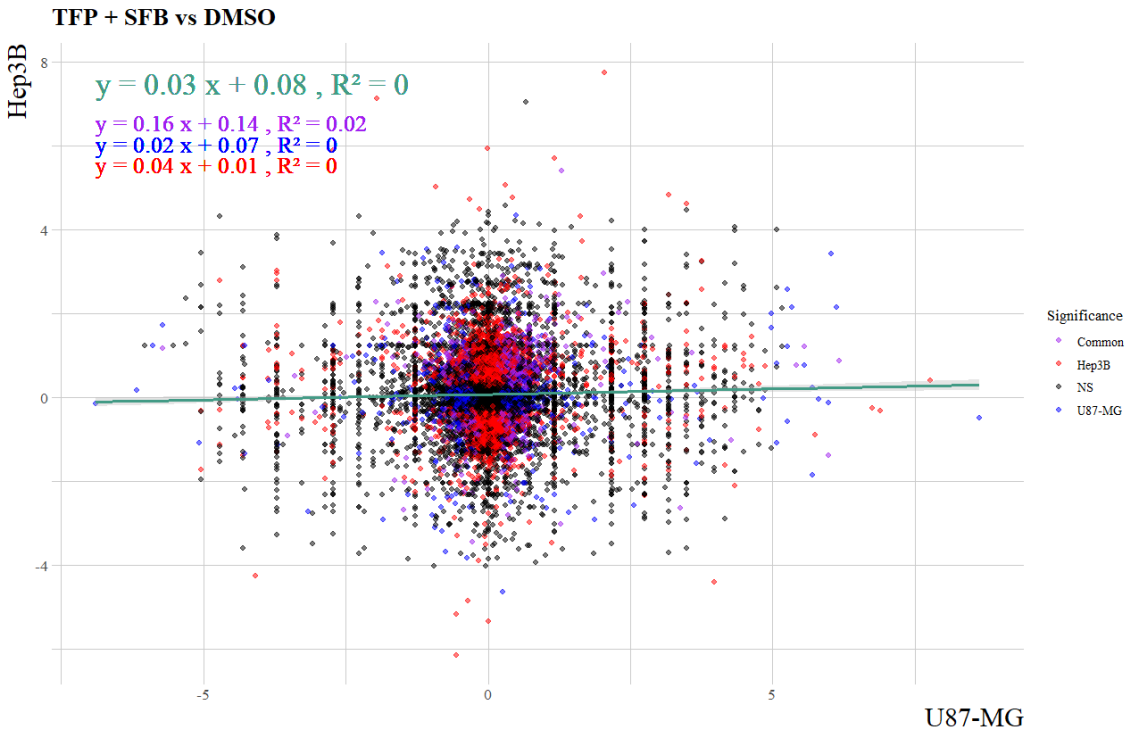

Appendix Figure 1. Regression plot for $\log_2$ fold-changes from RNA-seq data of $TFP_{12\ \mu M}$ + $SFB_{2\ \mu M}$ vs DMSO treated Hep3B cells (doubling time = 28.05h) for 48h, and $TFP_{10\ \mu M}$ + $SFB_{2.5\ \mu M}$ vs DMSO treated U87-MG cells (doubling time = 39h) for 72h; using p-value < 0.05 for significance threshold for both datasets.

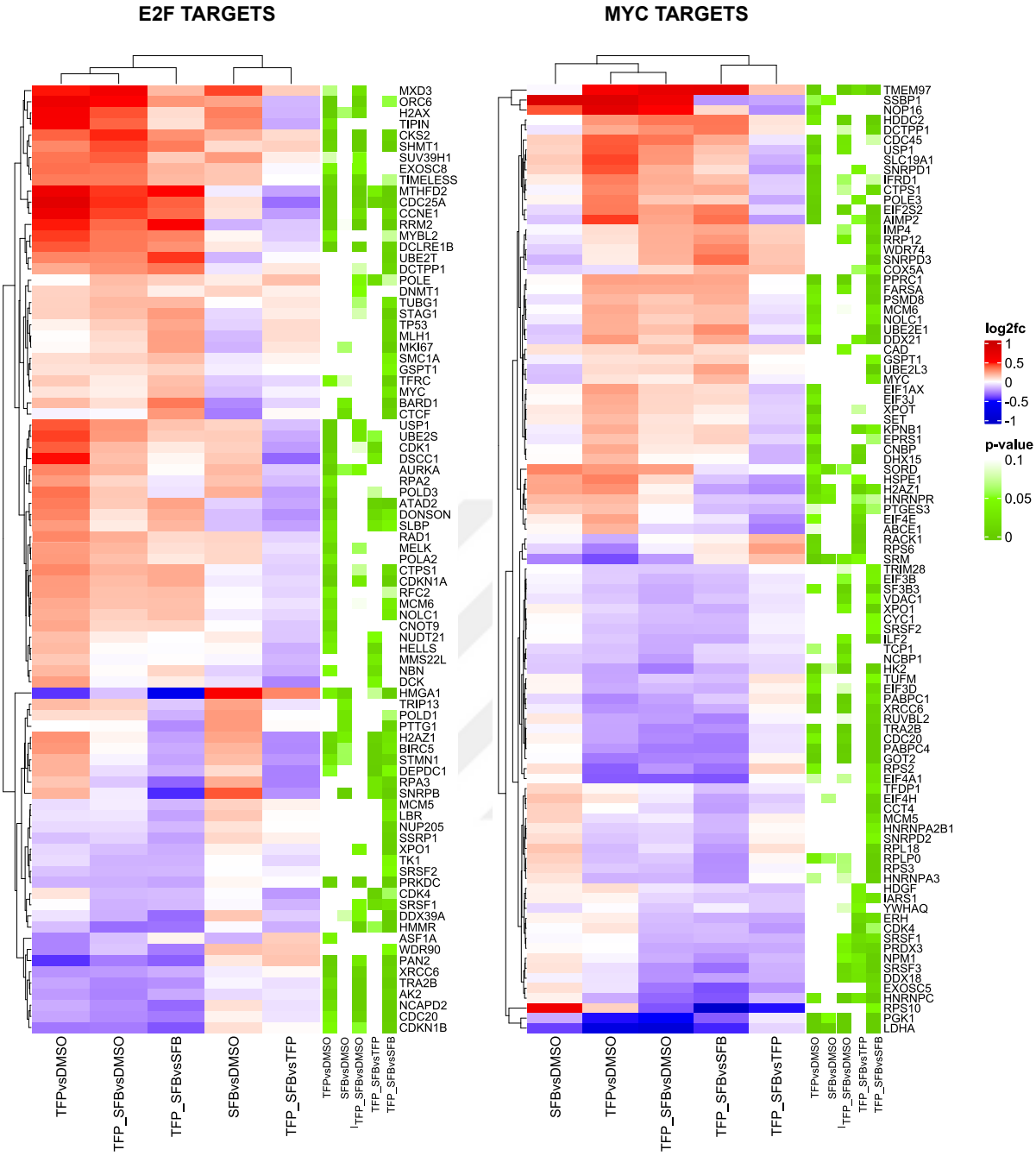

Appendix Figure 2. Log_2 fold-change heatmaps of MSigDB Hallmark E2F Targets *(M5925)* and MYC Targets V1/V2 *(M5926/ M5928)* gene sets, significantly modulated in at least one contrast (p-value < 0.05).

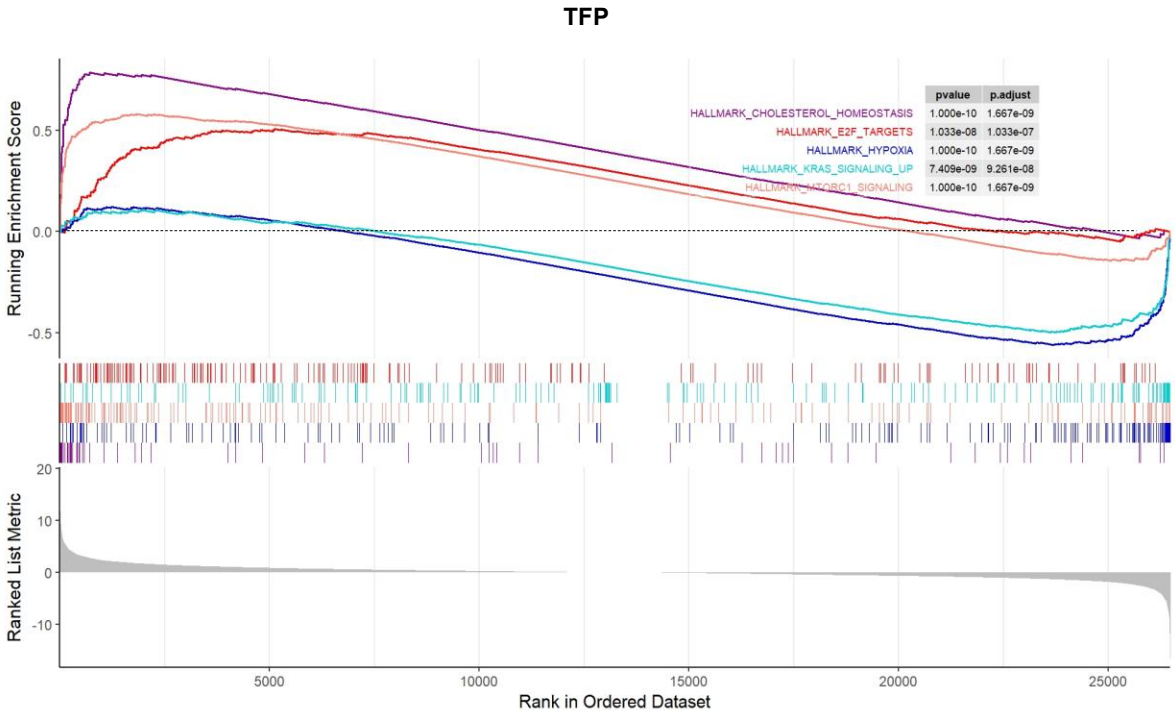

Appendix Figure 3. Visualization of top 5 gene set enrichment results using DESeq2 statistics covering log2 fold-change values and standard error ($TFP_{10\,\mu M}$ vs DMSO; p-value < 0.05 enrichment cutoff).

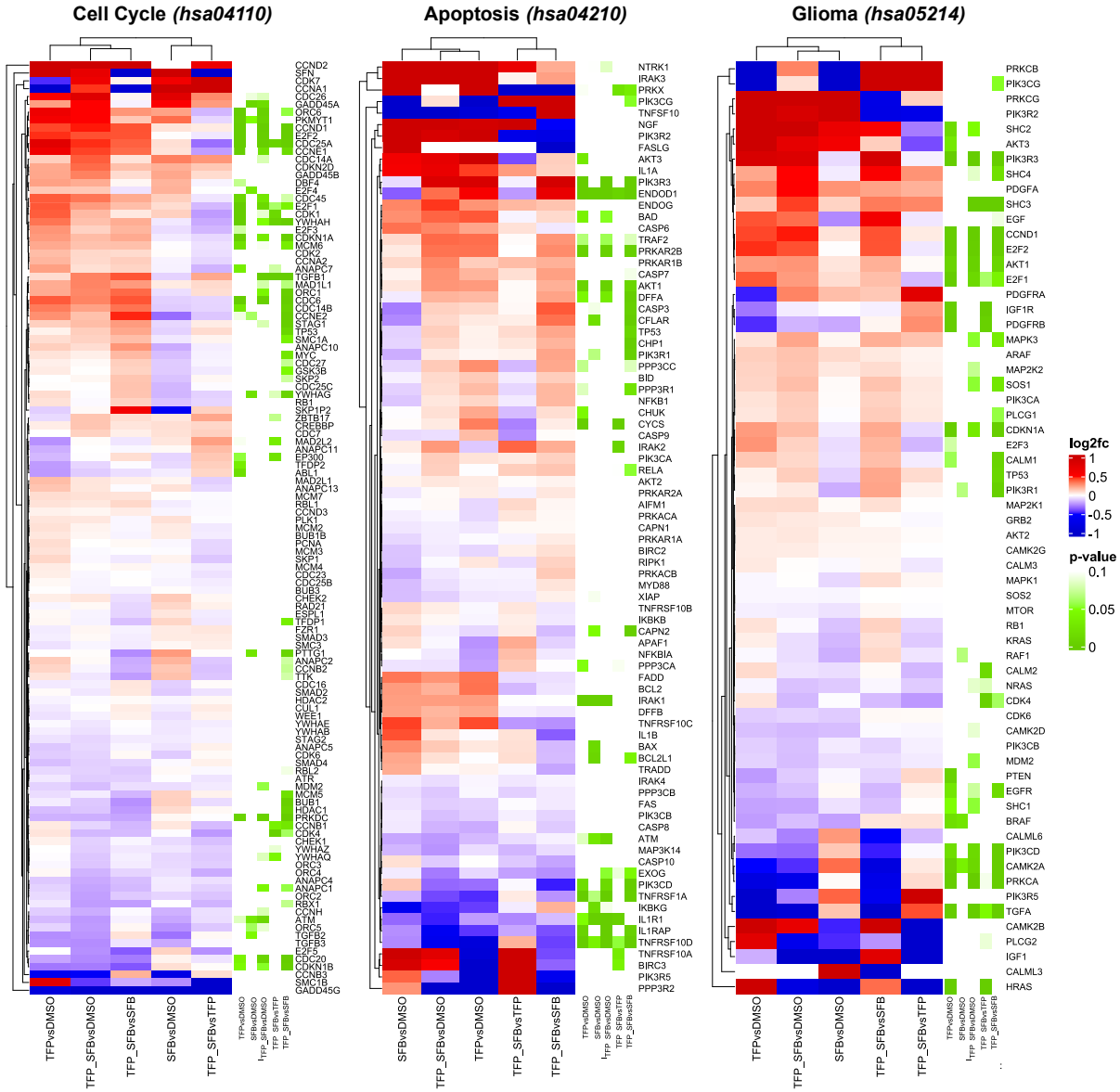

Appendix Figure 4. Log_2 fold-change heatmaps of cell cycle, apoptosis, and glioma KEGG pathway gene sets among from $TFP_{10\ \mu M}$ and/or $SFB_{2.5\ \mu M}$ treated U87-MG cell samples.

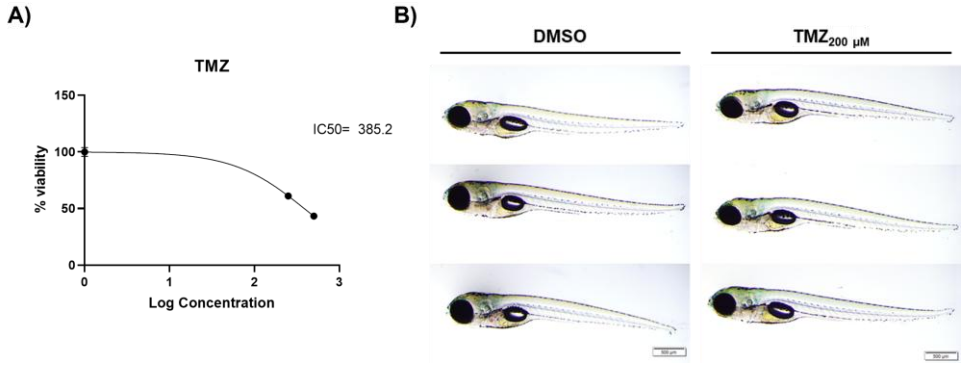

Appendix Figure 5. Results from experimental controls using TMZ. **A)** IC50 curve from MTT cell viability assay of 250 and 500 µM TMZ treated U87-MG cells. **B)** Bright field images of 5 dpf AB strain zebrafish larvae treated with DMSO control, and TMZ$_{200\ \mu M}$ for 72h; 3.2X magnification.

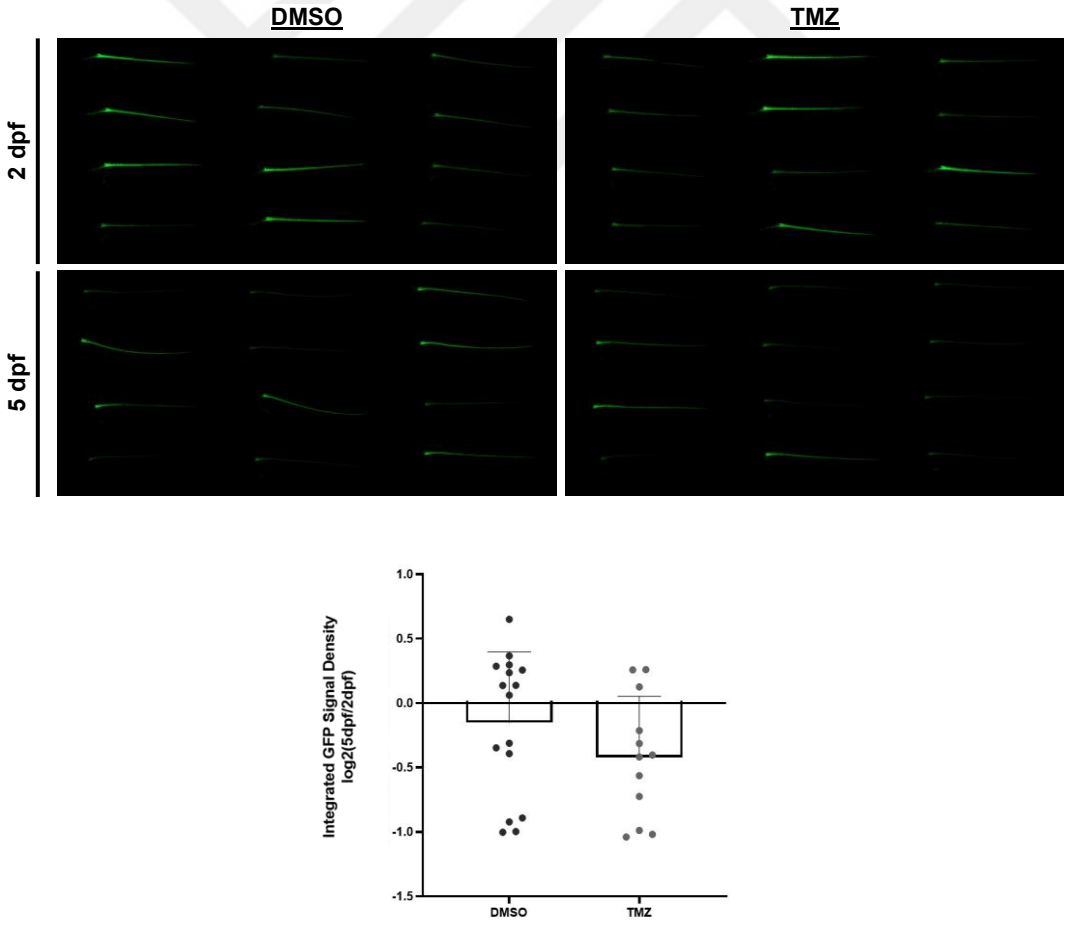

Appendix Figure 6. Fluorescent images of 5 dpf Tg(*gfap*:GFP) strain zebrafish larvae treated with DMSO control, TMZ$_{200\ \mu M}$ for 72h; 3.2X magnification.

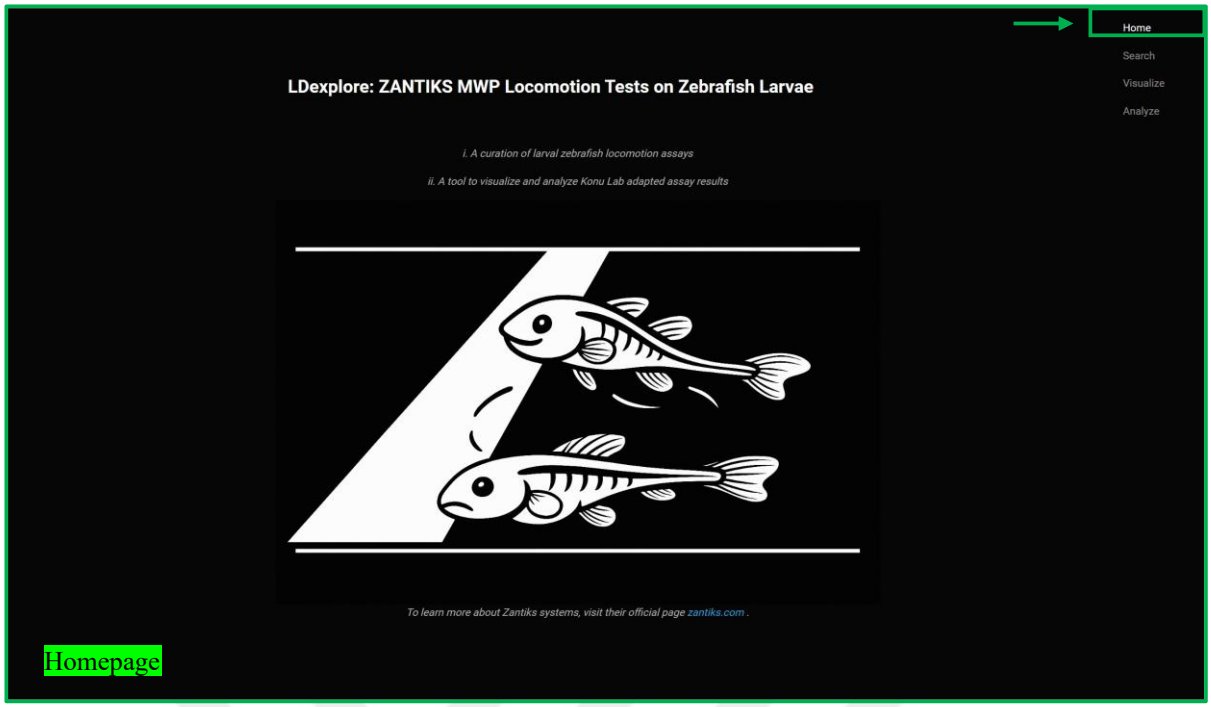

Appendix Figure 7.1. Homepage of *LDexplore: ZANTIKS MWP Locomotion Tests on Zebrafish Larvae*, an R Shiny based webpage that serves as a curation of larval locomotion assays in the literature and as a tool to analyze in-house *Zantiks MWP* assay results.

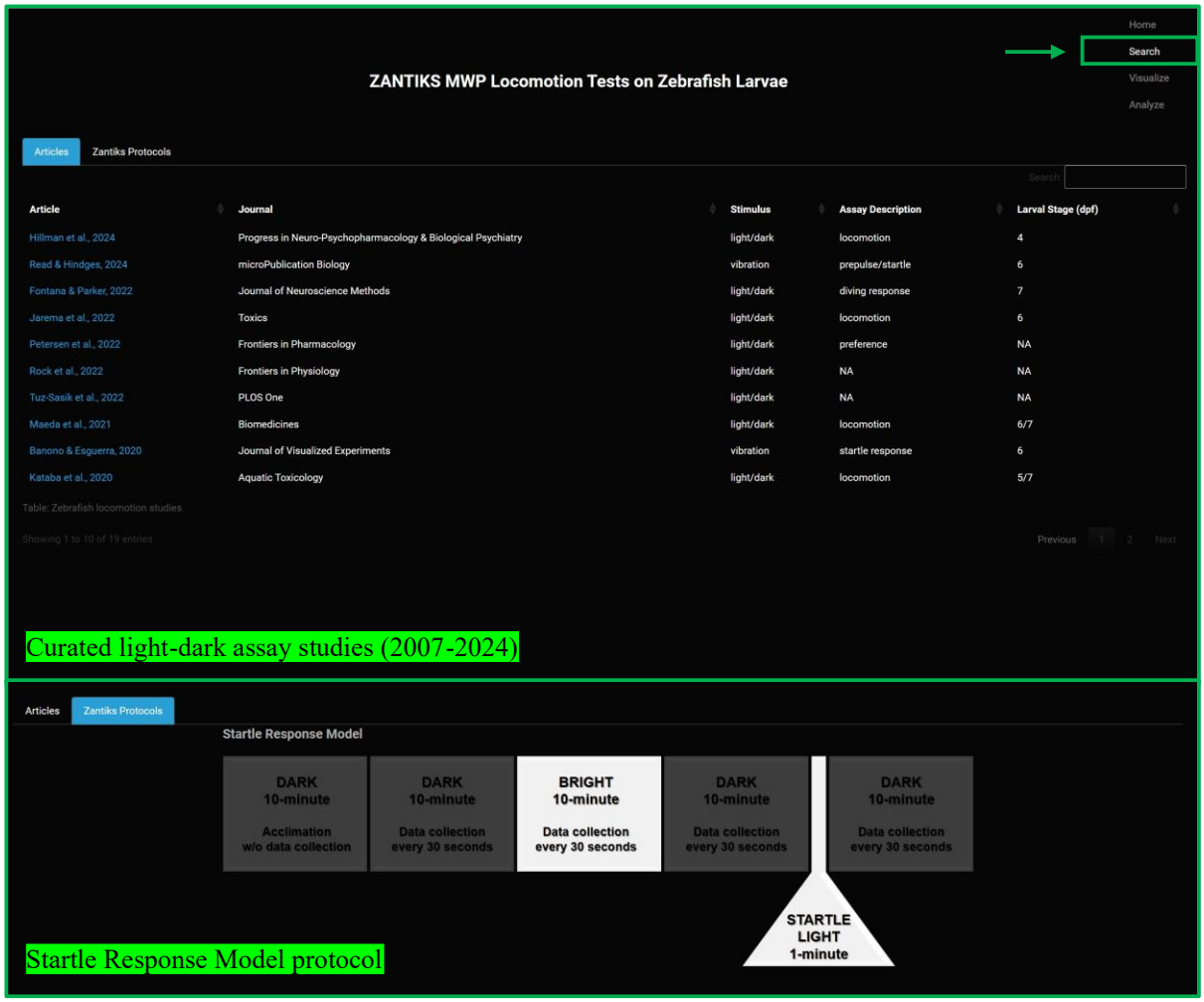

Appendix Figure 7.2. *Search* tab of *LDexplore*. Above panel shows the *Articles* subtab, in which a curated table of locomotion studies can be explored with article details, behavioural stimuli used, assay description, and larval zebrafish stage (dpf). Below panel shows the *Zantiks Protocols* subtab, in which the in-house protocol *Startle Response Model* is visually described for the associated *Zanscript*.

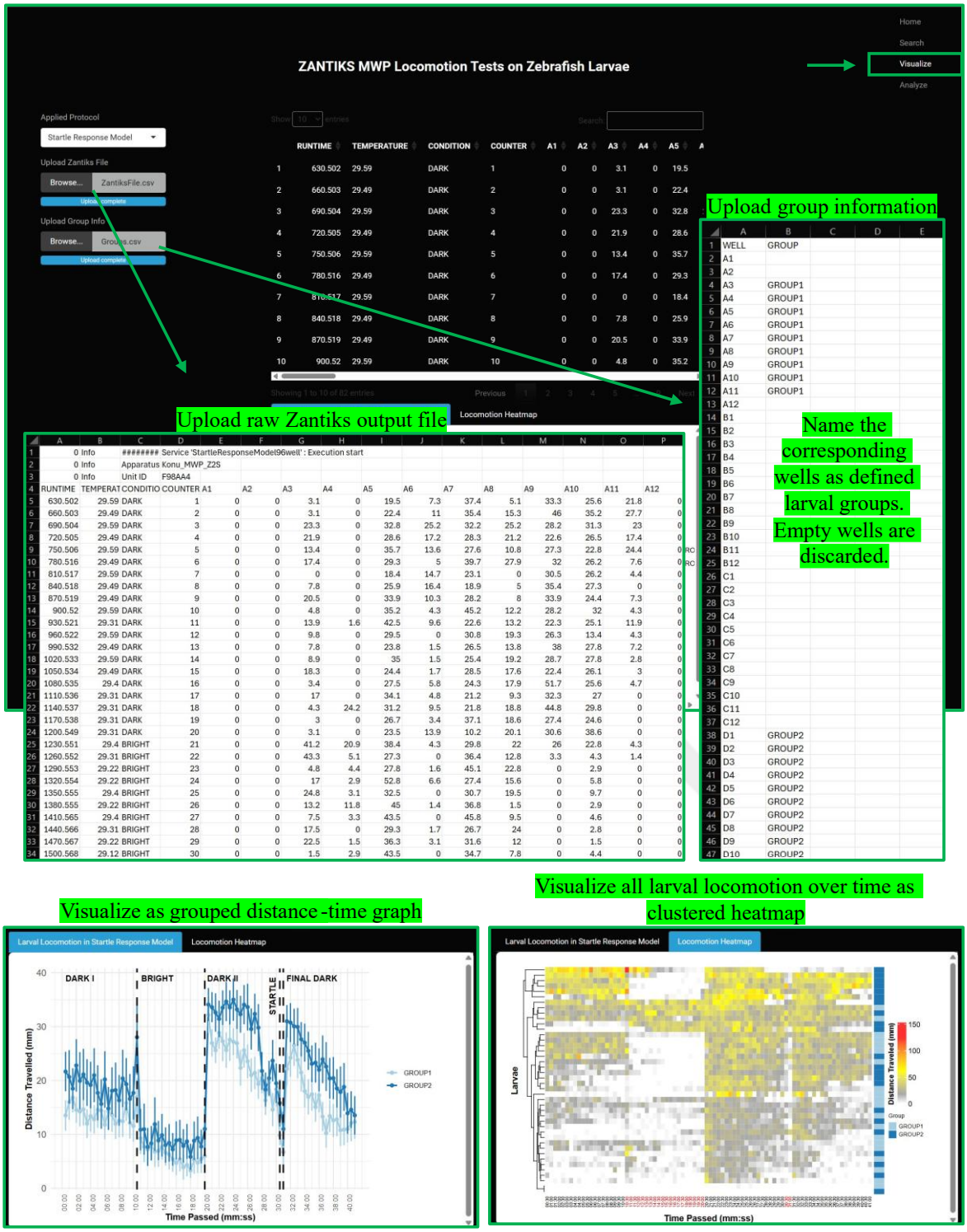

Appendix Figure 7.3. *Visualize* tab of *LDexplore* for *Zantiks* raw output data ingestion and preview. Above panel describes how to upload raw CSV files exported from the *Zantiks* system together with a custom group-annotation file that specifies the 96-well plate layout. Below panel describes how the inputs are reactively ingested and rendered in an interactive, scrollable table, which then feeds the plotting functions for grouped distance-time graph and clustered locomotion heatmap.

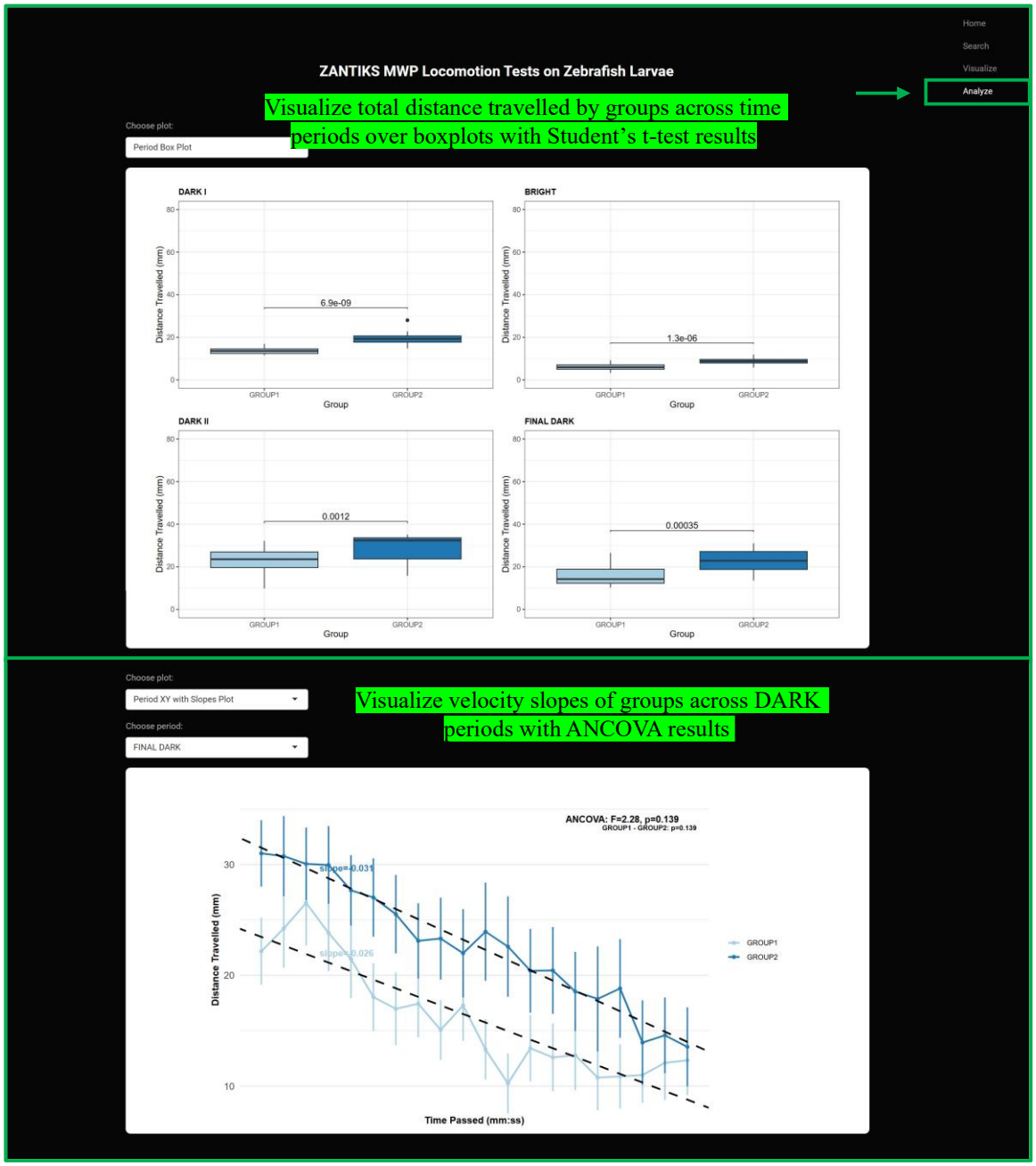

Appendix Figure 7.4. *Analyze* tab of *LDexplore* for downstream analysis of user input *Zantiks* assay data. Above panel shows the period boxplot module that divides total distance travelled into DARK/BRIGHT periods and compares each larval group by Student's t-test. Below panel shows the period specific distance-time graph with grouped velocity slopes and their ANCOVA statistics as well as p-values from pairwise group trend comparisons.

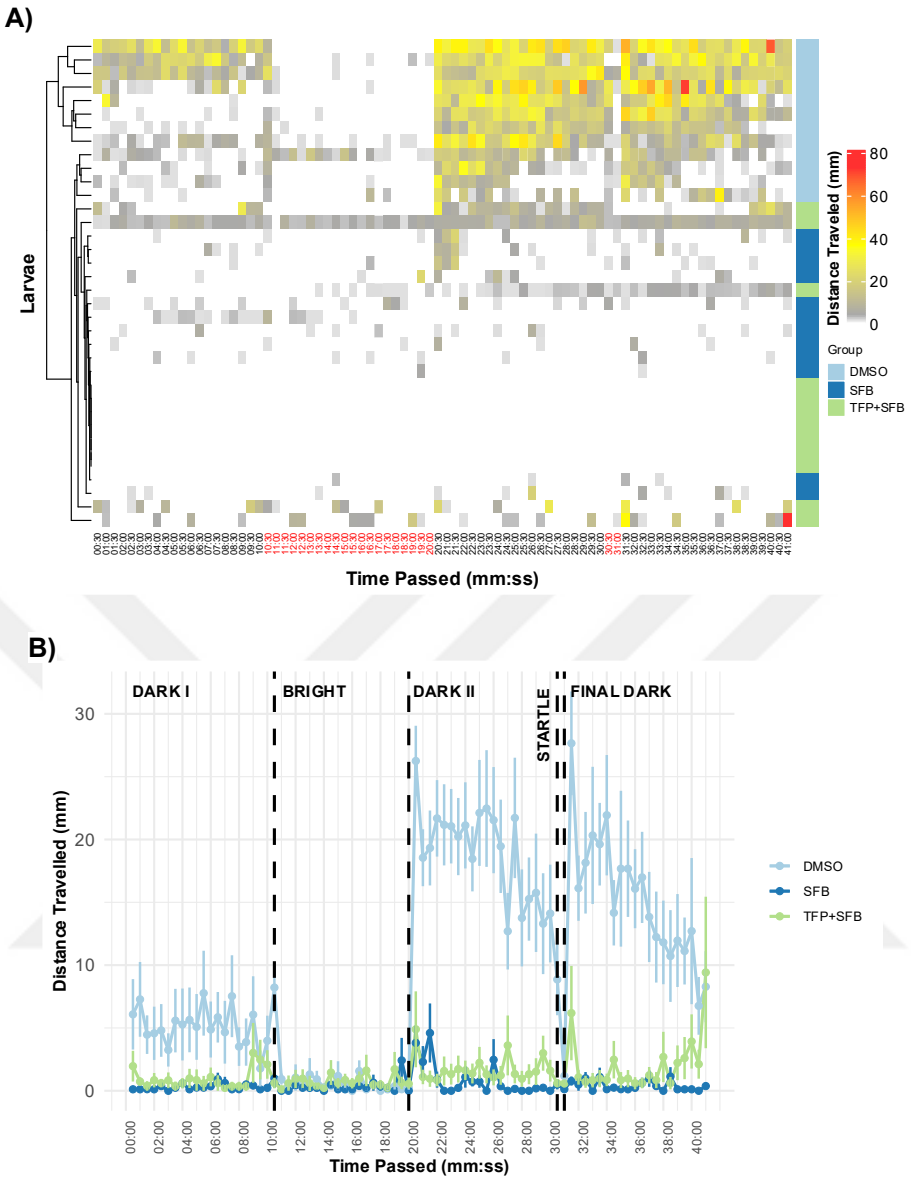

Appendix Figure 8. Locomotion assay results from *Startle Response Model* using *Zantiks MWP* system for 72h controlled 2.5 µM sorafenib with or without 10 µM TFP treated 5 dpf AB strain larvae. **A)** Clustered locomotion heatmap of distance travelled per time bin for individual larva. **B)** Distance-time graph of larval groups with standard error; from Shiny app output. ($n_{DMSO} = 12$, $n_{SFB} = 12$, $n_{TFP+SFB} = 12$)